INVESTIGATING LATE MIOCENE COCCOLITH GEOCHEMISTRY

by

SUSHANTH GATTUPALLI

A thesis submitted to the University of Birmingham
for the degree of MASTER OF SCIENCE BY RESEARCH

School of Geography, Earth, and Environmental Sciences
College of Life and Environmental Sciences
University of Birmingham

June 2024

Abstract

This study focuses on tiny marine organisms called coccolithophores, which produce calcium carbonate shells that store important information about past ocean conditions. Our research investigates how these shells show vital effects- differences in their carbon isotope composition that are influenced by the biology of the organism and its environment during the late Miocene, a period of significant environmental change. Scientists have suggested that these isotopic changes were driven by declining carbon dioxide (CO_2) levels during this time.

We used a new technique to separate coccoliths of different sizes and analyze their carbon and oxygen isotopic signatures, greatly increasing the amount of data available for this period. This provided a much more detailed timeline of changes compared to previous studies.

Our findings suggest that the vital effects seen in coccolith carbon isotopes are more closely related to global productivity trends, particularly during the Late Miocene Biogenic Bloom, rather than to shifts in CO_2 levels, which remained relatively stable.

Acknowledgment

I could not thank my supervisors, Dr. Tom Dunkley Jones, and Dr. Kirsty Edgar, enough. I am forever grateful to Tom for his invaluable guidance and continuous support from day one of my joining. His patience throughout this process, coupled with his career guidance, has been exceptional. Tom's support and encouragement have been crucial for the successful completion of this project. One of the best and most memorable times here in the UK for me is the field trip to S-W England. I enjoyed it a lot and thank you, Kirsty.

I would also like to thank Emma for her patience and support in the lab for, teaching me and fixing my unexpected problems during my time in the lab. A heartfelt thanks to Marcin for all the talks, encouragement, and career guidance. I also extend my sincere thanks to all the amazing staff in the Earth Sciences Department and my wonderful colleagues.

I would not be here today without the constant love and support from my mom, my sister Anu, and all my family members. To all my friends, who keep encouraging me even from miles away and cheering me up when I am down, thank you. A massive thanks to my friend Vaishnavi for always being there and being so helpful.

A particular massive thanks to my mentor, friend, and brother, Dr. Raghu Ram Katreddi. He has done so much for me, from guiding me in my research to providing unwavering support for the past eight years. His contributions have been instrumental in my journey.

Thank you all for your unwavering support and belief in my abilities.

Contents

List of Appendices

List of Figures

1 Introduction

1.1 Coccolithophores

Coccolithophores, marine calcifying phytoplankton algae, have thrived since the Jurassic period, evolving in morphology over millions of years (Bown et al., 2004). They belong to the kingdom Protista, Phylum Haptophyta, and class Prymnesiophyceae (see discussion in Silva et al., 2007) exhibiting diverse cell structures and forms (Billard & Inouye, 2004). As autotrophic primary producers, coccolithophores utilize photosynthesis in the ocean's photic zone, sometimes forming extensive blooms (Tyrrell & Merico, 2004) influenced by environmental factors such as nutrient availability and light intensity. The competition among species for nutrients shapes the composition and functionality of coccolithophore communities within these blooms (Margalef, 1978).

The soft cell is protected by an exoskeleton known as the coccosphere (Billard & Inouye, 2004), comprising multiple individual calcium carbonate ($CaCO_3$) coccoliths. Coccoliths exhibit distinct species-specific morphologies, making changes in their shapes and abundance over time useful indicators of past marine conditions and ecosystems. These variations serve as valuable proxies for reconstructing paleoenvironmental changes (Cavaleiro et al., 2020; Marino et al., 2009). These coccoliths (heterococcoliths) are formed inside the cell and later pushed out onto its surface hence, the older coccoliths will be towards the outer edge of the coccosphere (Young & Henriksen, 2003), although this mechanism may vary depending on the type of coccolith being produced within the coccolith-forming vesicle (Billard & Inouye, 2004). There are four possible ways that coccoliths can be arranged to form a coccosphere i.e. when two adjacent coccoliths are overlapping, interlocking, non-interlocking, and adjacent coccoliths arranged with edges directly abutting rather than overlapping (Young, 1997). Some coccospheres exhibit remarkable mechanical resilience, capable of withstanding hydrostatic pressure through inelastic deformation and controlled crack growth (Jaya et al., 2016).

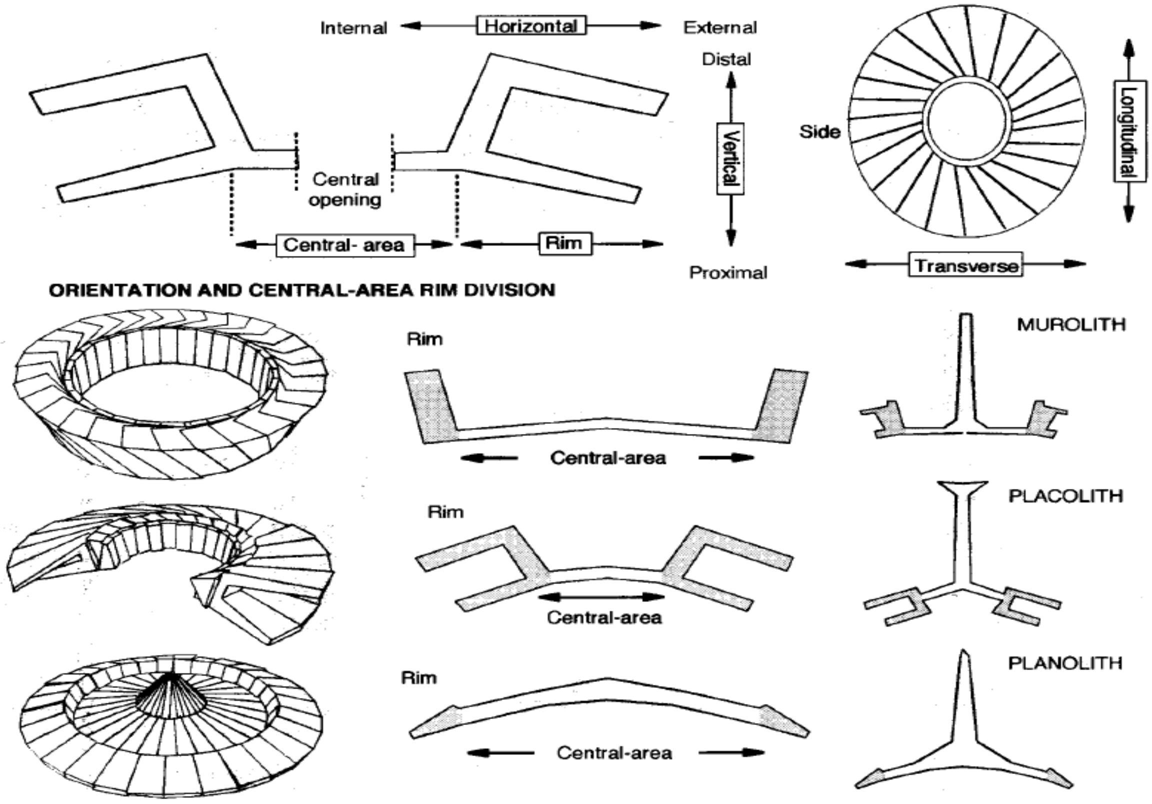

Figure 1.1 This Image, from Young (1997) showing a schematic representation of basic parts and shapes of coccoliths.

According to Young (1997), coccolith morphology consists of two basic components, a coccolith rim made of regular cycles, and a central area, which is enclosed by the rim (Figure 1.1). Occasionally, there is outward growth in the central area, forming a structure, including bridges, spines, processes, and nets (Young, 1997). Coccoliths exhibit diverse sizes and shapes, with a classification system introduced to streamline their description in the literature. Common shapes include murolith, planolith, and placolith, each defined by specific characteristics (Figure 1.1) (Young, 1997). Coccolith shapes in planar view range from perfectly elliptical and symmetrical to irregularly polygonal, lenticular, and asymmetrical (Young, 1997). Coccoliths vary in size from minuscule (<1µm) to very large (15µm), categorized as small (3 µm-5 µm), medium (5 µm-8 µm), and large (8 µm-12 µm) based on their length observed under light microscopy (Young, 1997).

Coccolithophores produce two main types of coccoliths: heterococcoliths and holococcoliths. Heterococcoliths are formed inside the cell during the diploid stage of the life cycle, within specialized vesicles, and are then pushed out to the surface (Billard & Inouye, 2004; Rowson et al., 1986). In contrast, holococcoliths are formed outside the cell during the haploid stage and consist of smaller, regularly arranged calcite crystals (Young et al., 1992). This difference in biomineralization processes leads to distinct structural characteristics for each type, with holococcoliths being more fragile and less likely to be preserved in the fossil record compared to heterococcoliths (Winter, 1994). Holococcoliths, formed from numerous, minute euhedral calcite crystals, are notably less prevalent than heterococcoliths in both extant species and the fossil record, likely due to their more rapid disintegration (Young et al., 1992; Winter, 1994). Unlike heterococcoliths, which consist of a radial array of variably shaped crystal units, holococcoliths' minute crystals make them more vulnerable to dissolution.

Coccolithophores can be further classified based on the types of coccoliths they produce. Monomorphic species produce only one type of coccolith throughout their life cycle, while dimorphic species produce two distinct types, often during different life stages. Polymorphic species, on the other hand, can produce multiple types of coccoliths, showing significant variation across life stages or within the population (Bown et al., 2014; Gard, 1987).

The importance of fossil coccospheres in coccolithophore research is due to their capacity to preserve cellular features and offer valuable palaeobiological data (Bown et al., 2014). Coccospheres also provide partial protection against microzooplankton predation and viral attacks (Haunost et al., 2020; Taylor et al., 2017). Culturing experiments reveal shifts in coccosphere size and coccolith numbers in response to growth phases and nutrient availability, shedding light on species responses to environmental changes over time (Sheward et al., 2017). Most coccolithophores live in the surface mixed layer above the thermocline, at depths less than 100 – 150 meters, so coccospheres could also help vertical depth positioning with flotation and accelerated sinking allowing faster nutrient uptakes (Munk & Riley, 1952). If an autotrophic organism were to stay still in calm water, it would quickly use up the nearby nutrients. The cell's division rate would then depend on how fast nutrients could diffuse from the surrounding water into the nutrient-depleted area around it. However, if the cell sinks, it would keep encountering new nutrient-rich areas (Hutchinson, 1967).

Determining the chemical composition of these coccoliths is very hard due to their minute sizes. In general, a typical coccolithophore size lies between 2 µm – 75 µm (Jordan, 2009), and a typical coccolith size varies between 1 µm – 15 µm (Suchéras-Marx et al., 2022; Young, 1997). Early petrographic analyses have revealed that the elemental composition of coccoliths is composed of calcium carbonate ($CaCO_3$) (Müller et al., 2014). Later rudimentary chemical and X-ray diffraction studies of bulk nannofossil ooze added further support to this idea (Isenberg et al., 1963), using better chemical and X-ray diffraction techniques eventually confirmed that the plates produced by these coccolithophores are made up of the mineral calcite.

Coccoliths and calcareous nannofossils (Young & Henriksen, 2003) contribute significant amounts of calcium carbonate to calcareous oozes or chalk deposits at the sea floor (Figure 1.2). The coccolithophores as $CaCO_3$ secreting phytoplankton impact the global carbon cycle via consumption of CO_2 during the photosynthesis and generation of CO_2 during the calcification (Westbroek et al., 1993). Coccolithophores are estimated to be responsible for about half of all modern $CaCO_3$ precipitation in the oceans and hence, play an important role in the global carbon cycle (Milliman, 1993).

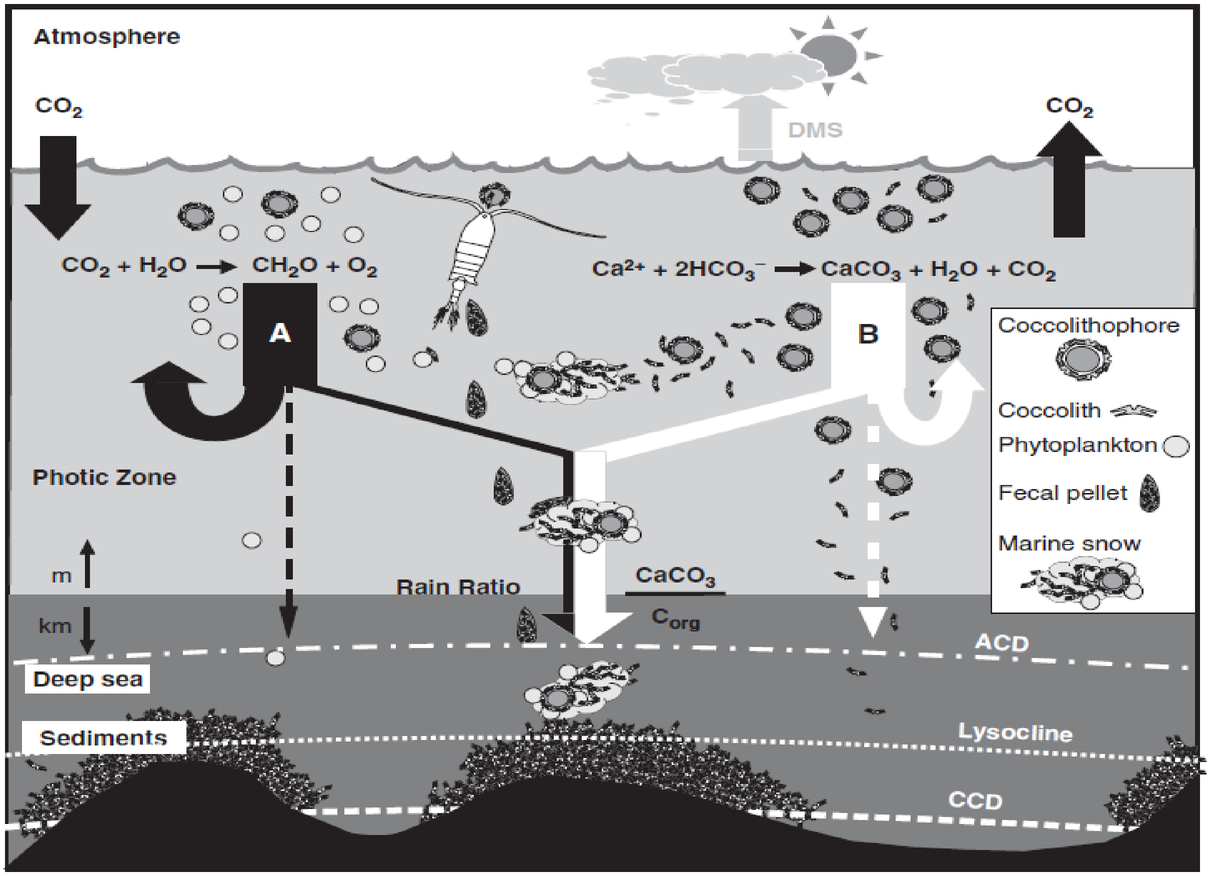

Figure 1.2 . Image taken from de Vargas et al. (2007), The figure illustrates how coccolithophores contribute to the global carbon cycle. In the photic zone, coccolithophores aid in gas exchange and organic matter export to deep ocean layers, driving both the carbonate counter-pump (B) and the organic carbon pump (A). Their coccoliths, resistant to dissolution, eventually settle on the seafloor, forming significant fossil records over millions of years.

At present, the global carbon cycle is the subject of critical examination and global research because of the anthropogenic carbon input into the atmosphere (Bhatti et al., 2005; Jian, 2003; Orr et al., 2005; Wang et al., 2001). Oceans are 'carbon sinks' because there is a net global absorption of carbon from the atmosphere to the oceans through downward diffusion processes (Feely et al., 2005; Raven & Falkowski, 1999), and the removal of dissolved carbon from the surface to the deep ocean through photosynthesis in planktonic species (Sabine et al., 2004). According to Rost & Riebesell (2004), ' *A critical part of evaluating global environmental changes related to carbon dioxide input is a clearer understanding of the process governing the production, fate, and cycle of biogenic materials in the sea.'* Coccolithophores play a major role in capturing dissolved carbon in the surface ocean, through the production of coccoliths and the fixation of organic carbon, a proportion of which then sinks and eventually settles at the bottom of the sea floor after death (Rock et al., 2018) (Figure 1.2). Since coccolithophores are at the base of the food chain, there is a high chance of being consumed by other higher species such as copepods. Hence, coccolithophores often do not complete the full life cycle and end up in the gut of predators, and are processed into fecal pellets (Honjo, 1976). The sedimentation of coccoliths is extremely slow because of their low mass and large relative surface area, but laboratory experiments have shown that coccoliths or coccospheres can descend rapidly in fecal pellets or relatively large particles (Honjo, 1976). Upon reaching the seabed, several physical, chemical, and biological processes act on the sediment via diagenesis (Winter, 1994) before they eventually form sedimentary rock, in the form of claystone, marl, and chalks. Coccolithophores distribution in the oceans is influenced by various factors, including salinity, temperature, and nutrient availability, leading to distinct biogeographic zones (Baumann et al., 1999). This adaptability to different marine environments underscores their ecological significance and contributions to oceanic carbon sequestration.

1.2 Late Miocene Climate and Environment

Having explored the biology and role of coccolithophores in marine ecosystems, it is important to now consider the environmental context in which they have evolved. The environmental shifts during the Late Miocene (~11.6 Ma to 5.3 Ma), including notable climatic changes, offer essential context for exploring how coccolithophores adapted to evolving oceanic conditions and fluctuations in the global carbon cycle

This study is focused on producing new coccolith size-fraction isotope data to better determine the timing and controls on the divergence in carbon isotope values of large-to-small coccoliths during the Late Miocene (Bolton & Stoll, 2013). I review the environmental and climate conditions of the Late Miocene, particularly trends in atmospheric carbon dioxide (CO_2) concentrations and changes in surface ocean productivity, both key drivers of this isotopic divergence.

The late Miocene epoch is a time marked by significant global cooling and the rise of modern ecosystems (Herbert et al., 2016) (Figure 1.3). During this period, continental conditions and mountain topography transitioned toward modern conditions, and global flora and fauna evolved toward the modern taxa we know today (Steinthorsdottir et al., 2021b) (Figure 1.5). During the Miocene, tectonic activities significantly influenced current geographical settings leading to mountain formation in various regions like the circum-Mediterranean, circum-Pacific, and central Asia (Steinthorsdottir et al., 2021b). Although the proto-Tibetan highland was likely present before the final collision between the Indian and the Eurasian plate, plateau uplift continued during the late Miocene in southern and central Tibet (Wang et al., 2014) (Figure 1.6) creating a rain shadow effect and influencing the intensification of the South Asian Monsoons (Ding et al., 2017). Throughout the Neogene period, sedimentary erosion rates rose, as indicated by global sedimentary volume estimates and oceanic carbonate accumulation rates, and this combined evolution of tectonic uplift, monsoon climate, and erosion rates may have strongly influenced marine biogeochemical cycles (Steinthorsdottir et al., 2021b).

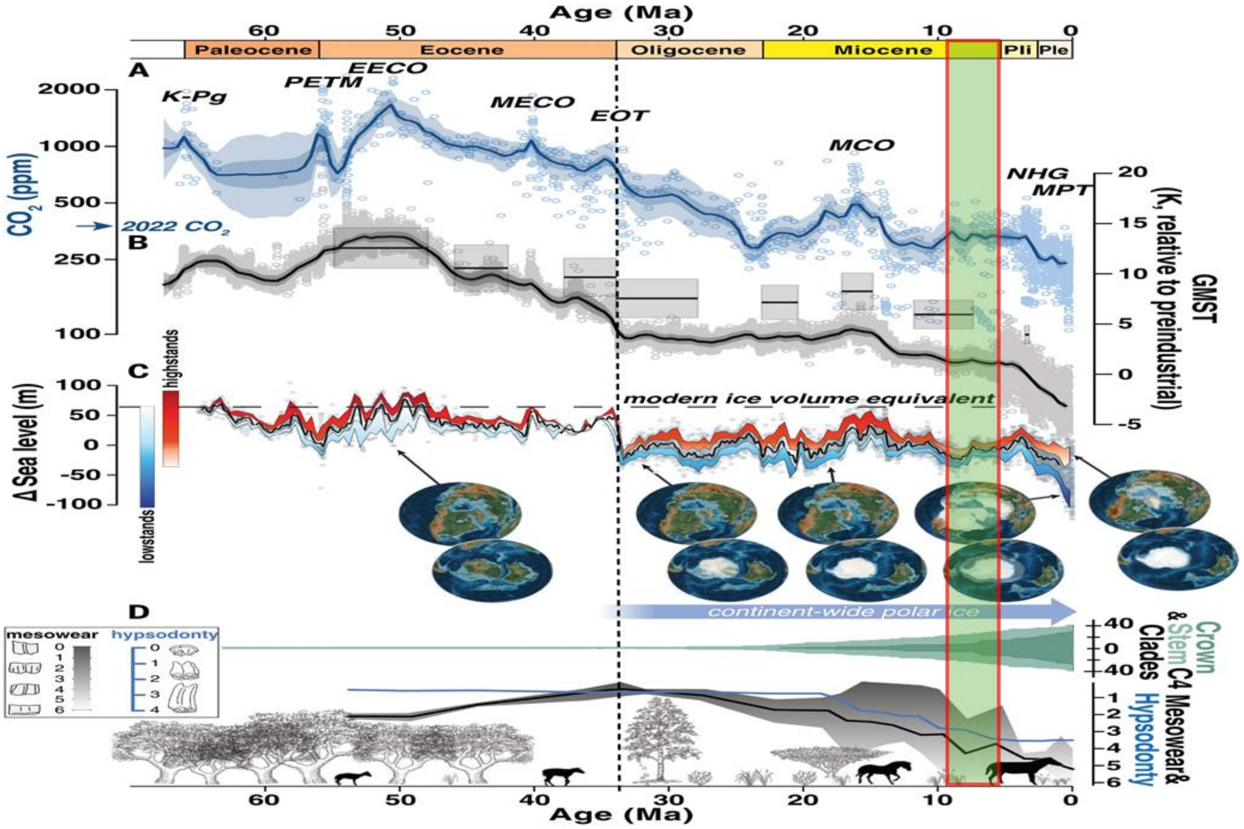

Figure 1.3 Image from Hönisch et al. (2023), illustrates, variations in atmospheric CO_2 of the Late Miocene highlighted in a shaded pale green box with red boundary.

During the Miocene epoch, significant tectonic changes influenced oceanic circulation. The Drake Passage opened in the Oligocene, allowing the connection between Antarctica and South America (Lagabrielle et al., 2009). The early Miocene featured an open Tethys gateway connecting the Atlantic and Indian oceans, closing by the late Miocene (Rögl, 1999). The Bering Strait was closed for most of the Miocene, opening possibly in the late Miocene, while the Fram Strait widening and Greenland-Scotland Ridge subsidence connected the Arctic and North Atlantic (Steinthorsdottir et al., 2021b). The Messinian Salinity Crisis marked the end of the Miocene (Roveri et al., 2014),

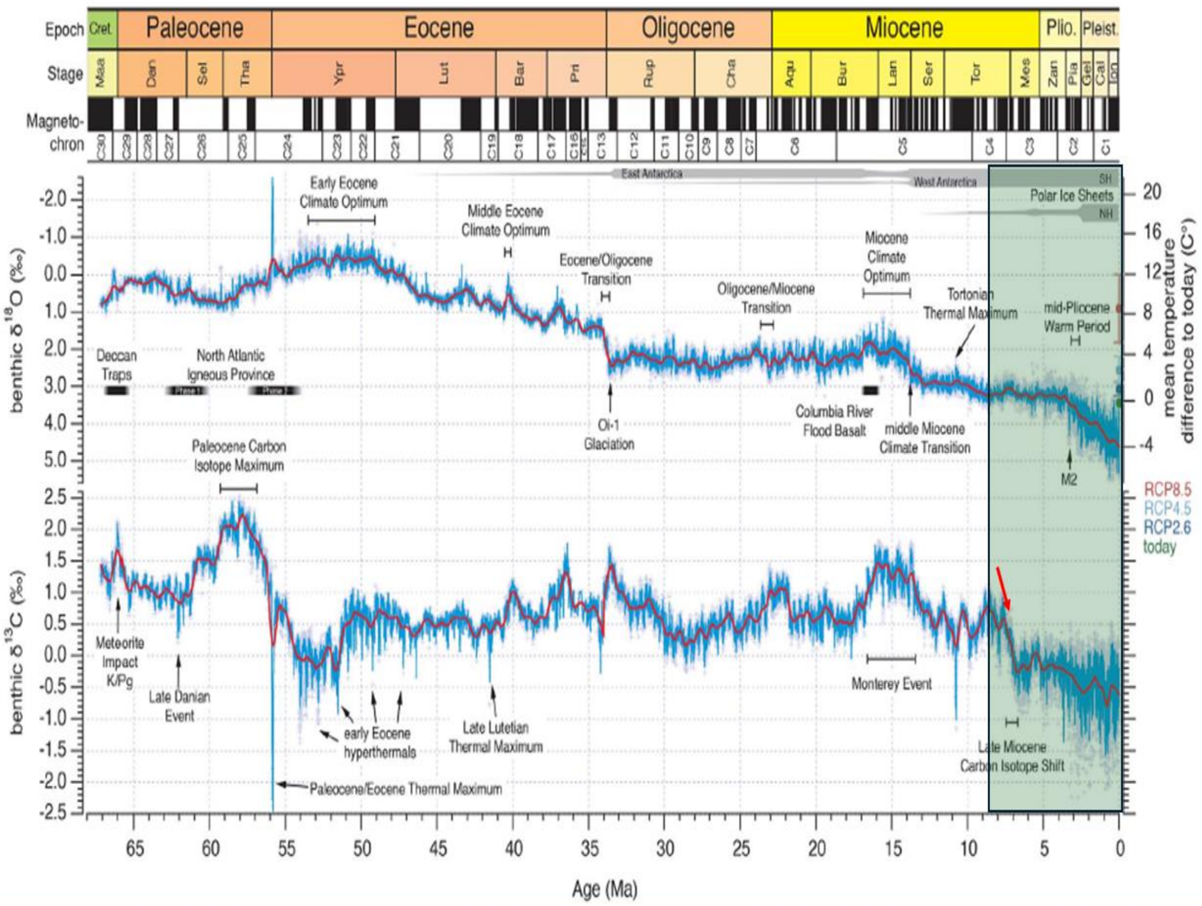

Figure 1.4 This image is taken from Westerhold et al. (2020), presents with long-term benthic foraminifera $\delta^{18}O$ and $\delta^{13}C$ values. The late Miocene to recent data is highlighted in a pale green rectangular box. The red arrow indicates the Late Miocene Carbon Isotope Shift (LMCIS) around ~ 8 Ma ago.

with closed connections between the Atlantic and the Mediterranean due to tectonic convergence (Krijgsman et al., 2018).

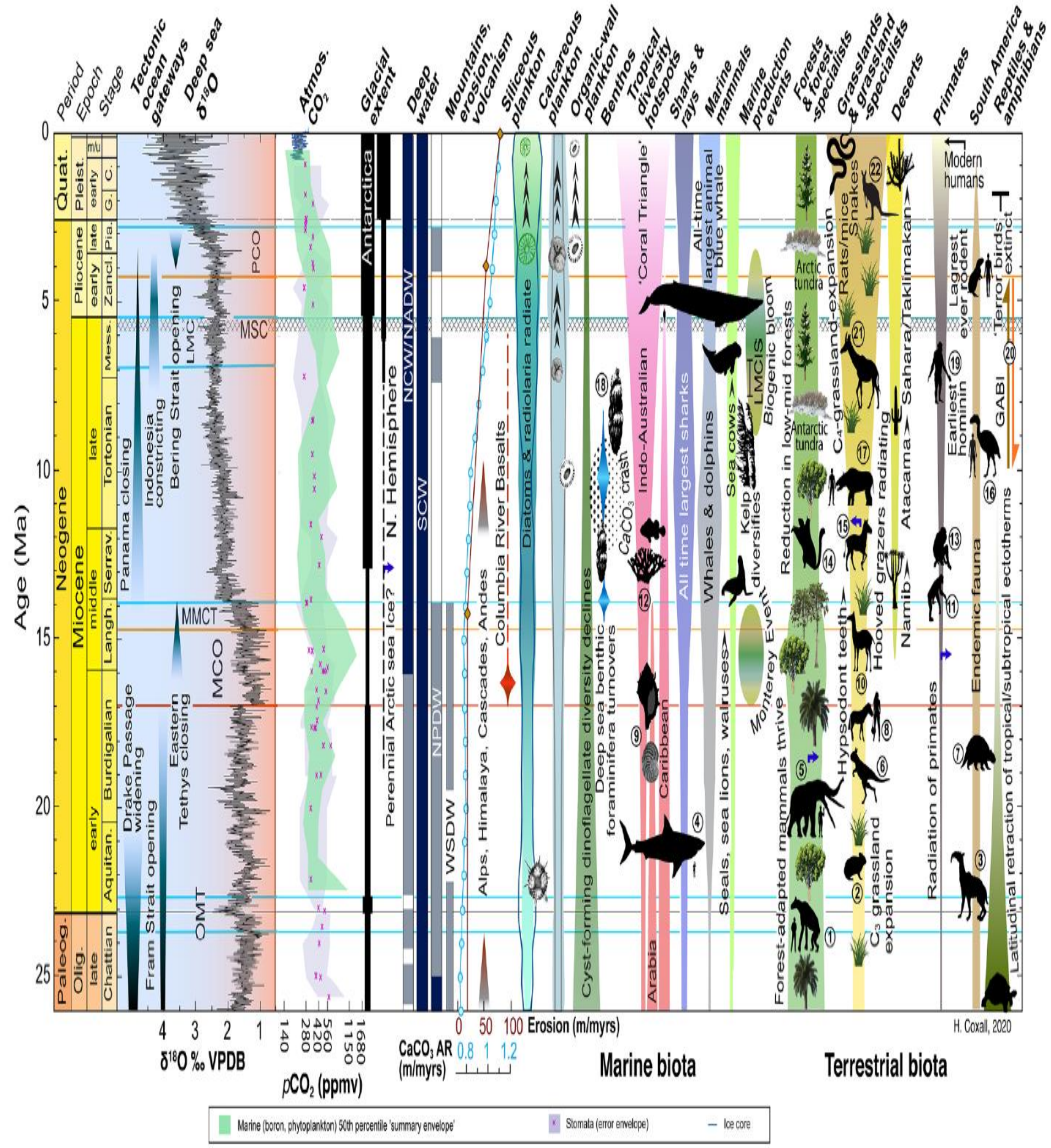

Figure 1.5 This figure from Steinthorsdottir et al. (2021a) shows climate, tectonic, and oceanic changes over the Miocene period, including data on biogenic bloom, $CaCO_3$ accumulation rates, and tectonic activity. The figure also highlights shifts in oceanic circulation patterns and carbonate deposition.

During the Miocene epoch, the marine ecosystem underwent significant evolutionary changes influenced by various factors such as plate tectonics, ocean currents, temperature, and chemistry of the oceans (Steinthorsdottir et al., 2021b). The fossil record of marine plankton provides insights into these transformations. Calcareous nannoplankton, primarily coccolithophores, played a crucial role as primary producers, contributing to pelagic carbonate burial in the deep sea (Si & Rosenthal, 2019). The decline in coccolithophore species diversity from the middle Eocene to the Oligocene, associated with global cooling, led to smaller cell sizes, reflecting decreasing levels of pCO_2 (Bolton et al., 2016; Dunkley Jones et al., 2008; Hannisdal et al., 2012). During the Miocene, marine planktonic siliceous diatoms, essential for ocean carbon cycling, diversified rapidly, particularly in high latitudes (Lewitus et al., 2018; Suto, 2006). The success of marine diatoms, linked to ocean cooling and increased nutrient availability, contributed to the biological carbon pump, potentially impacting atmospheric pCO_2 levels and global climate states (Falkowski et al., 2004; Renaudie, 2016; Tréguer et al., 2018).

Foraminifera, the major group of calcareous zooplankton, experienced turnover, and diversification during the Miocene, with shell size increases suggesting complex evolutionary patterns influenced by global environmental changes (Ezard et al., 2011; Schmidt et al., 2004). Deep-sea foraminifera changes around the Middle Miocene Climate Transition (MMCT; 14.7 Ma - 13.8 Ma) and late Miocene indicate responses to environmental shifts, such as oxygen minimum zone (OMZ) expansion in the subtropical Indian Ocean (Singh et al., 2012).

After the Mid Miocene Climate Optimum (~17 to 14 Ma), global cooling from approximately 13 Ma reduced the distribution of certain nannoplankton to more tropical latitudes (Haq, 1980) and contributed to the rise in dominance of *reticulofenestrids* across high and low latitudes in the

Atlantic (Henderiks et al., 2020). Overall, the Miocene marine ecosystem witnessed dynamic shifts driven by a combination of geological, oceanic, and climate factors.

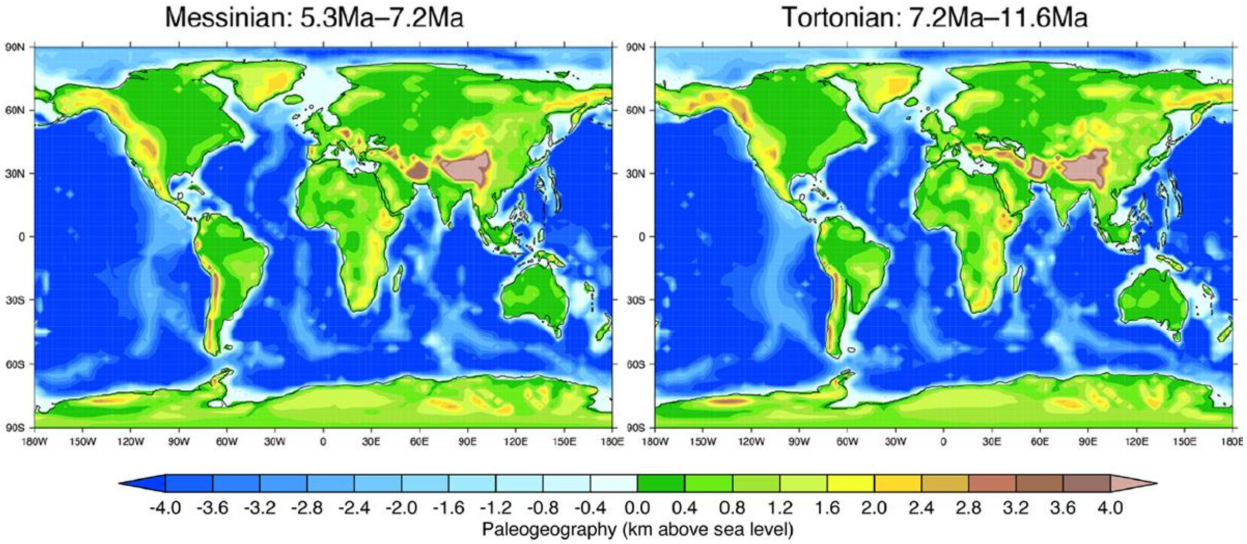

Figure 1.6 The image is highlighting the paleogeographic and topographical evolution from the Late Miocene epoch. Colors represent elevation changes relative to sea level, from Steinthorsdottir et al. (2021b).

The Late Miocene and the early Pliocene biogenic bloom (LMBB) is an important event of global high productivity and mass accumulation of carbonate, from calcareous nannoplankton and foraminifera and opal from diatoms in the world oceans (Dickens & Owen, 1999; Farrell et al., 1995; Lyle & Baldauf, 2015). Increased accumulation rates of both carbonate and biogenic silica were observed from around 9 Ma in the Indian Ocean and from 8 Ma in the Eastern Equatorial Pacific region, indicating the start of the event during this period (Dickens & Owen, 1999; Pillot et al., 2023) (Figure 1.7). The end of the event is placed at the decrease in sedimentation rate observed between, 4.5 – 4.4 Ma in the Eastern Equatorial Pacific region (Lyle et al., 2019) and ~ 3.5 Ma in the Indian Ocean (Dickens & Owen, 1999). More recently, Karatsolis et al, (2022), found evidence of increased primary productivity in the Atlantic up to 3.5 Ma, but this was limited to a single site (tropical ODP Site 925) and may not represent the entire Atlantic basin. Other authors also identified this event, as a high productivity interval, in the South China Sea between 12 and 6 Ma (Zhang et al., 2009) and the southwestern Pacific Ocean around 9 and 3.8 Ma with maximum productivity at around 5 Ma (Grant & Dickens, 2002). Diester-Haass et al (2005) identified the LMBB in three different regions of the Atlantic Ocean between 8.2 and 3.3 Ma. Hermoyian & Owen (2001) identified the LMBB from the low-productivity regions of the Atlantic and Indian Oceans by measuring the mass accumulation rate of phosphorus, a limiting nutrient that controls the primary production in the oceans, which is closely correlated with bulk sediment mass accumulation rates and suggests that the LMBB's occurrence was influenced by a global influx of phosphorus rather than by redistribution of nutrients among ocean basins. In these phosphorus accumulation records, the LMBB reaches a peak of productivity at ~4 Ma – 5 Ma (Hermoyian & Owen, 2001).

Overall, LMBB exhibits a widespread geographical distribution across the Pacific, Atlantic, and Indian oceans (Dickens & Owen, 1999; Diester-Haass et al., 2005; Farrell et al., 1995; Hermoyian & Owen, 2001; Lyle et al., 2019) (Figure 1.8). Predominantly concentrated at mid and low latitudes, the LMBB is notably absent or yet to be recovered in the Southern and Arctic oceans (Pillot et al., 2023). In the Indian Ocean, increased primary productivity was observed in the north and western parts resulting in the expansion of the OMZ southeastward (Dickens & Owen, 1999). In the Pacific Ocean, LMBB signatures are present off the coast of Australia, the northern Tasman Sea, and the northern Pacific, particularly in the eastern equatorial region between 5°N and 5°S (Pillot et al., 2023).

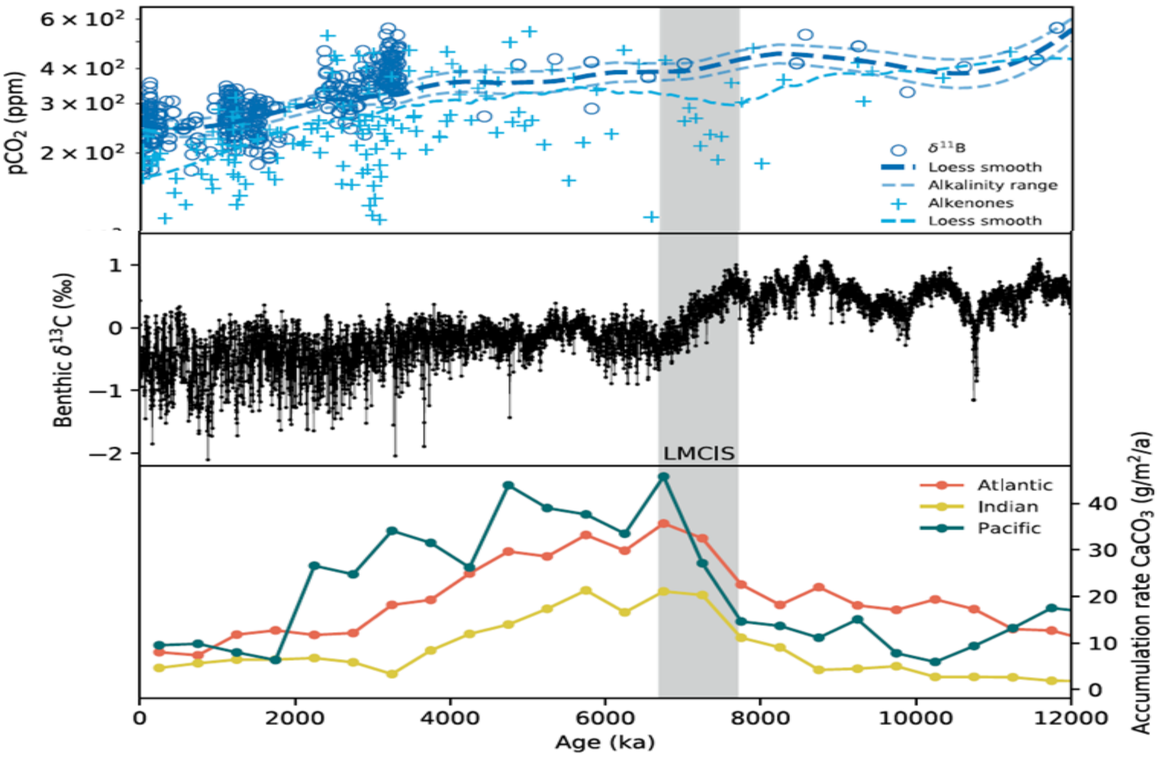

Figure 1.7 This figure illustrates mass accumulation rates of $CaCO_3$ in three ocean basins (Atlantic, Pacific, and Indian), alongside variations in pCO_2 levels and benthic foraminifera $\delta^{13}C$ data. It highlights the connection between carbonate deposition, ocean chemistry, and isotopic signals from 8 Ma to the present, crucial for understanding shifts in marine productivity and the global carbon cycle. From, Pillot et al. (2023).

Conversely, sites without an LMBB signature tend to be a few degrees further north and south. Sites lacking the LMBB signature, often located less than 2,000 km from coastlines, may be influenced by dissolution effects, potentially related to local depth variations (Pillot et al., 2023) (Figure 1.8). The full distribution of LMBB remains incompletely understood, hindered by limited data coverage and temporal variations in available datasets (Pillot et al., 2023).

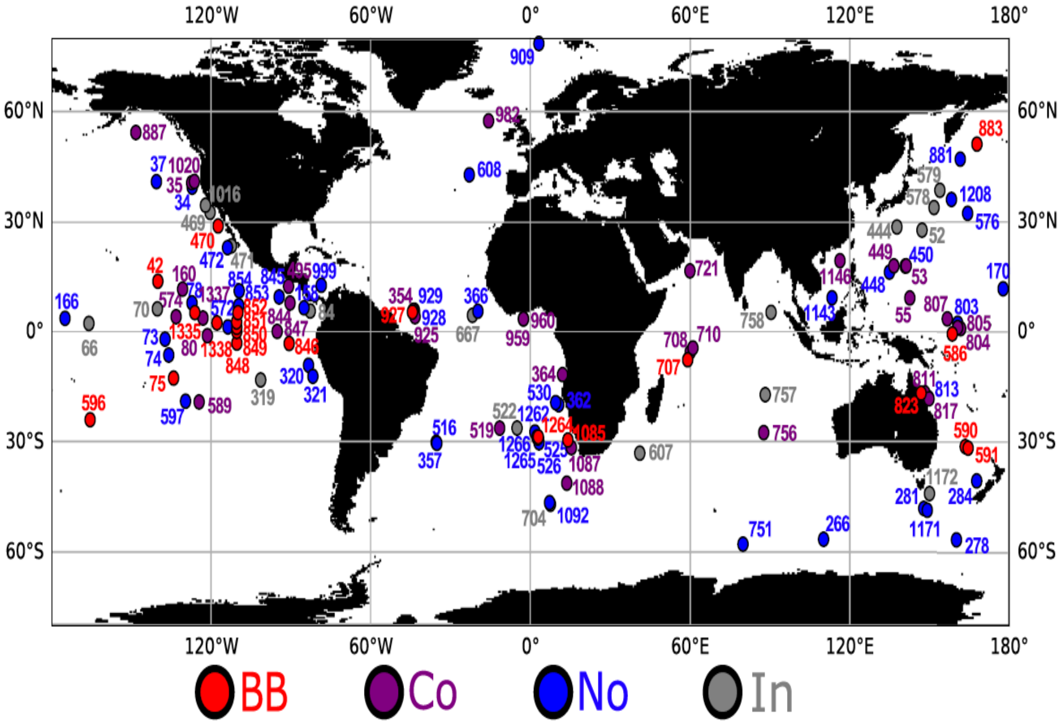

Figure 1.8 This image is from, Pillot et al. (2023). Sites where LMBB is present are represented as red dots, blue dots represent the absence of an LMBB event whereas purple and grey are the sites either controversial or inconclusive.

There are two main hypotheses for the factors contributing to a significant increase in marine productivity during the LMBB:

i. An increase in nutrient supply from continents to oceans, possibly driven by the Tibetan Plateau uplift, Andean uplift, intensification of trade winds, and continental aridification (Bowen et al., 2020; Herbert et al., 2016). Orogenic uplift would have intensified monsoon rainfall, enhanced continental weathering, and increased sediment transported to the oceans (Bowen et al., 2020; Curry, 1995). The global spread of C4 plants (Tauxe & Feakins, 2020) may have introduced siliceous phytoliths into the oceans, contributing to the biogenic bloom (Cortese et al., 2004). The influx of phytoliths could have alleviated silica limitation and promoted diatom growth, enhancing oceanic productivity.

ii. Redistribution of nutrients in the ocean due to changes in oceanic circulation, influenced by factors like amplification of North Atlantic Deep Water (NADW) formation (Berger et al., 1992) and the closure of the Central American Seaway (Farrell et al., 1995; Pisias et al., 1995). For example, changes in ocean circulation intensified upwelling in the Eastern Equatorial Pacific, resulting in increased surface nutrient concentrations and higher primary productivity (Schneider & Schmittner, 2006). Both events, NADW and the closure of the American Seaway resulted in intensifying and altering ocean circulation patterns and either increased or redistributed areas of nutrient-rich upwelling among the ocean basins (Pillot et al., 2023). Another explanation focuses on the strengthening of global ocean circulation driven by increased trade winds due to the enhancing of the latitudinal temperature gradient due to global decreases in pCO_2 and the growth of polar ice sheets (Diester-Haass et al., 2005).

According to Dickens and Owen,(1999), high rates of surface productivity at the Indo-Pacific divergence zone induce a significant downward flux of organic carbon. The decomposition of this sinking organic matter within the water column causes pronounced OMZ that exist at intermediate water depths beneath all present-day Indo-Pacific divergence zones (Wyrtki, 1971). Oceanographic models indicate that increased surface productivity will intensify underlying intermediate water OMZs (Olson et al., 1993) lies in the relationship between surface productivity and oxygen consumption in the deeper ocean layers. When surface productivity increases, more organic matter sinks to intermediate depths, where it decomposes and consumes oxygen, leading to the formation or intensification of OMZs. This process is particularly important in highly productive regions like the Indo-Pacific, where sinking organic material creates pronounced OMZs. Understanding this relationship is essential for interpreting past biogeochemical cycles and modern OMZ patterns, especially as OMZs influence marine biodiversity and nutrient cycling.

The biogenic bloom hypothesis suggests increased primary productivity in the north and western Indian Ocean during this period, extending the OMZ southeastward by more than 5,000 km (Dickens & Owen, 1999). According to Pillot et al,(2023) '*The spatial heterogeneity of LMBB data supports the nutrient supply scenario, yet the global nature of the event challenges solely a local cause.'* Proximity to coastlines and the influence of the East Asian Monsoon do not consistently align with the presence or absence of the LMBB event (Pillot et al., 2023). From the literature, the late Miocene holds records of increased dust accumulation in the Pacific and China seas (Hovan, 1995; Molnar, 2005; Rea, 1994; Rea et al., 1998). The data compilation by Pillot et al (2023), however, does not support the hypothesis of an increase in dust flux during this time interval. Furthermore, if nutrient input were indeed influenced by dust, it would likely be restricted to areas downwind of arid and desert regions, which does not clearly align with the patterns observed in the records (Pillot et al., 2023). Therefore, the role of dust as a significant contributor to nutrient input during the late Miocene biogenic bloom appears to be unsupported by their compiled data (Pillot et al., 2023).

In summary, LMBB is an important event of high biological productivity in the oceans globally. The onset and end of the event are not well constrained, but in most records, the intensity of productivity increase reaches a maximum at around 7 Ma. Both hypotheses discussed above seem plausible because the event is highly seen in places of upwelling areas. The LMBB event is very important in the study of climate control on the global carbon cycle and the origin of the modern oceans. Further research should explore the mechanisms of this event to enhance understanding.

1.3 Late Miocene Coccolith Isotope Fraction: declining CO_2 or Productivity?

Coccolithophores, which produce calcium carbonate ($CaCO_3$) plates called coccoliths, play a key role in the global carbon cycle. These organisms not only contribute to oceanic carbon sequestration through calcification, but also impact isotopic records, providing valuable information about past environmental conditions. Unlike organisms that biomineralize at or outside the cell wall, such as foraminifera, coccolith calcite reflects the internal physiological processes within the coccolith-forming vesicle. These processes leave distinct chemical signatures on the coccolith calcite, influenced by both external environmental conditions and the carbon acquisition strategies of the cell during growth and calcification (Hermoso, 2014).

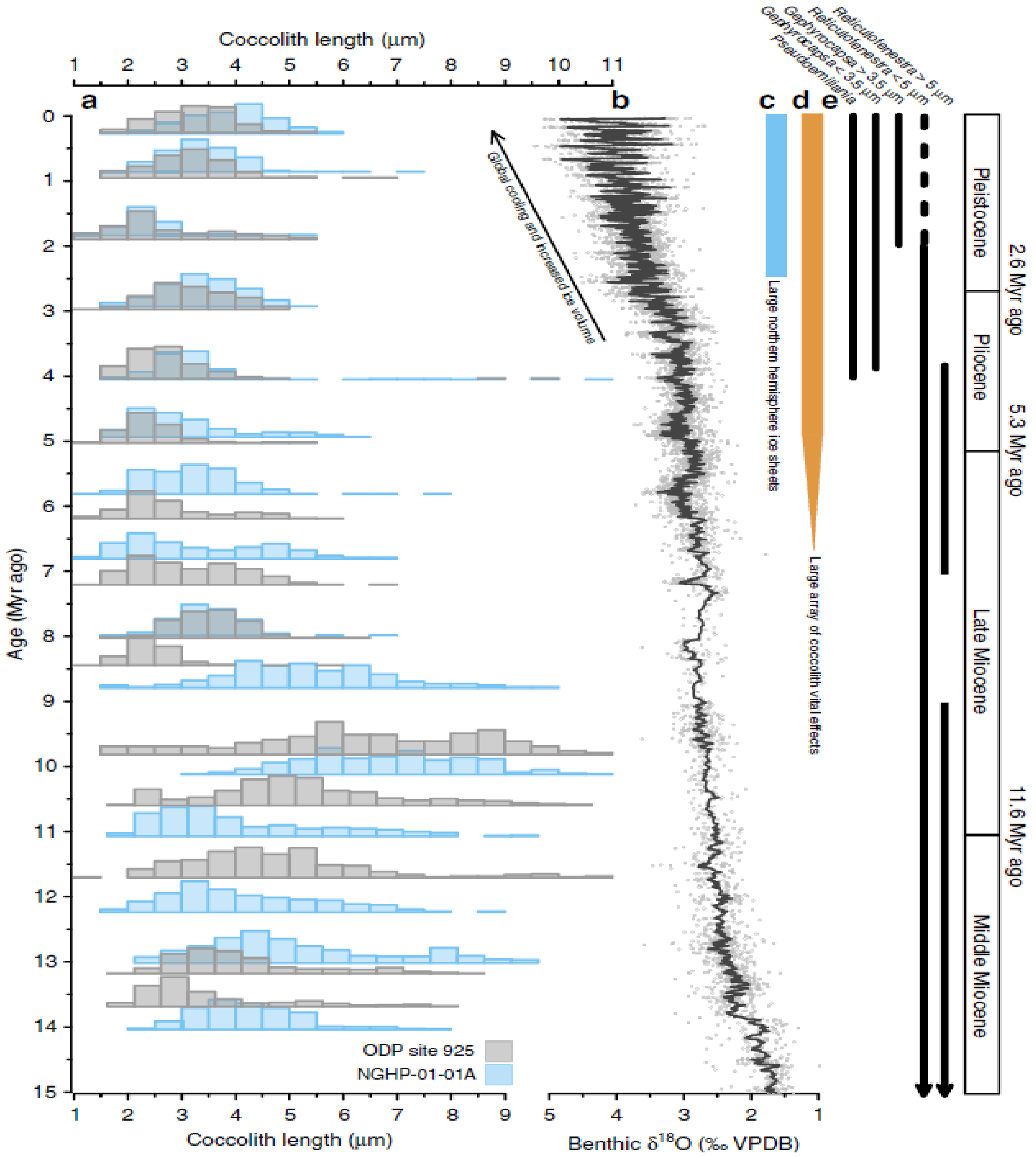

Figure 1.9 Image from, Bolton et al. (2016), showing a reduction in the sizes of coccolith approx. around 8 Ma. the grey bar represents ODP site 925 in the Atlantic Ocean and light blue bar represents NGHP-01-01A site from Kerala-Konkan basin.

In a seminal study, Bolton & Stoll (2013) observed significant differences in the carbon isotopic composition of large versus small coccoliths, which first appeared around 8 million years ago. These isotopic differences were interpreted to signal the onset of carbon limitation, particularly for larger coccolithophores, during a late Miocene decline in atmospheric CO_2 levels. This limitation in available carbon is thought to have driven the adoption of energetically costlier but more efficient carbon uptake pathways (Bolton & Stoll, 2013; Hermoso, 2014).

Larger coccolithophores, with their lower surface area-to-volume ratio, are especially sensitive to changes in CO_2 levels during the diffusive uptake of Dissolved Inorganic Carbon (DIC) from sea-water. Under carbon-limited conditions, larger coccolithophores increasingly relied on bicarbonate (HCO_3-) as a carbon source for photosynthesis. This adaptation was crucial because CO_2 levels were too low for efficient diffusive uptake. By utilizing more HCO_3-, larger coccolithophores could maintain photosynthesis rates; however, this shift created a trade-off. Bicarbonate is also necessary for calcification, and using more of it for photosynthesis reduced the amount available for building coccoliths. As a result, the calcification process was hindered, contributing to the observed isotopic offset in larger coccolith $\delta^{13}C$ values. This response highlights the organism's physiological adaptation to maintain productivity at the expense of calcification, which had evolutionary implications during the late Miocene.

The evolutionary consequences of this carbon limitation during the late Miocene were profound. As atmospheric CO_2 levels declined, the energy required for calcification increased, particularly for larger, heavily calcifying coccoliths. This shift made the production of smaller coccoliths more advantageous, leading to the selection of smaller coccolithophores over time. Figure 1.9 clearly shows a shift toward smaller coccolith sizes during this period.

Our research aims to investigate whether the observed isotopic offsets in coccolith $\delta^{13}C$ values are more closely related to declining atmospheric CO_2 levels or changes in marine productivity, particularly during the Late Miocene Biogenic Bloom (LMBB). The LMBB represents a period of increased marine productivity, which may have driven changes in carbon cycling and coccolith isotopic composition. By analyzing $\delta^{13}C$ and $\delta^{18}O$ signatures in very coarse (V.C) and very fine (V.F) coccolith size fractions, this study provides higher temporal resolution data, offering new insights into the timing and controls of coccolith isotopic fractionation during the late Miocene.

2 Methodology

2.1 Sampling

The sediment samples used in this study were collected as part of International Ocean Discovery Program (IODP) Expedition 363, from site U1482 from the Indian Ocean, north-west coast of Australia, (see Figure 2.1) at 15°3.32'S, 120°26.10'E and a water depth of 1,466 m (Rosenthal et al., 2018). The sediment at IODP Site U1482 consists mainly of nannofossil ooze, changing to

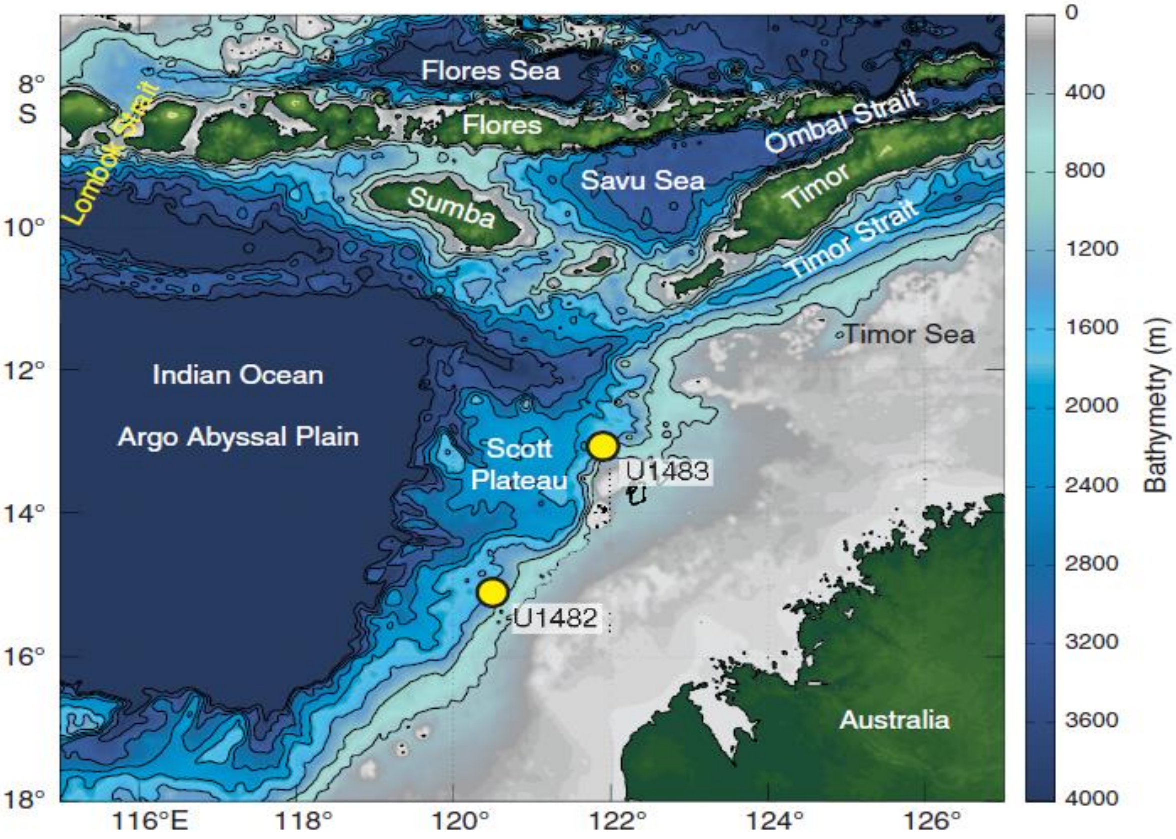

Figure 2.1 This image shows the study area of IODP Site U1482, located in the northwestern Australian shelf, represented with a yellow circle, along with Site U1483 from, Rosenthal et al. (2018).

chalk ~375 meters below the seafloor (mbsf), with layers characterized by secondary lithologies containing different amounts of foraminifers and clay minerals alternating with the primary lithology (Figure 2.3), creating submeter-scale cycles where the boundaries between layers are typically gradual rather than abrupt (Rosenthal et al., 2018).

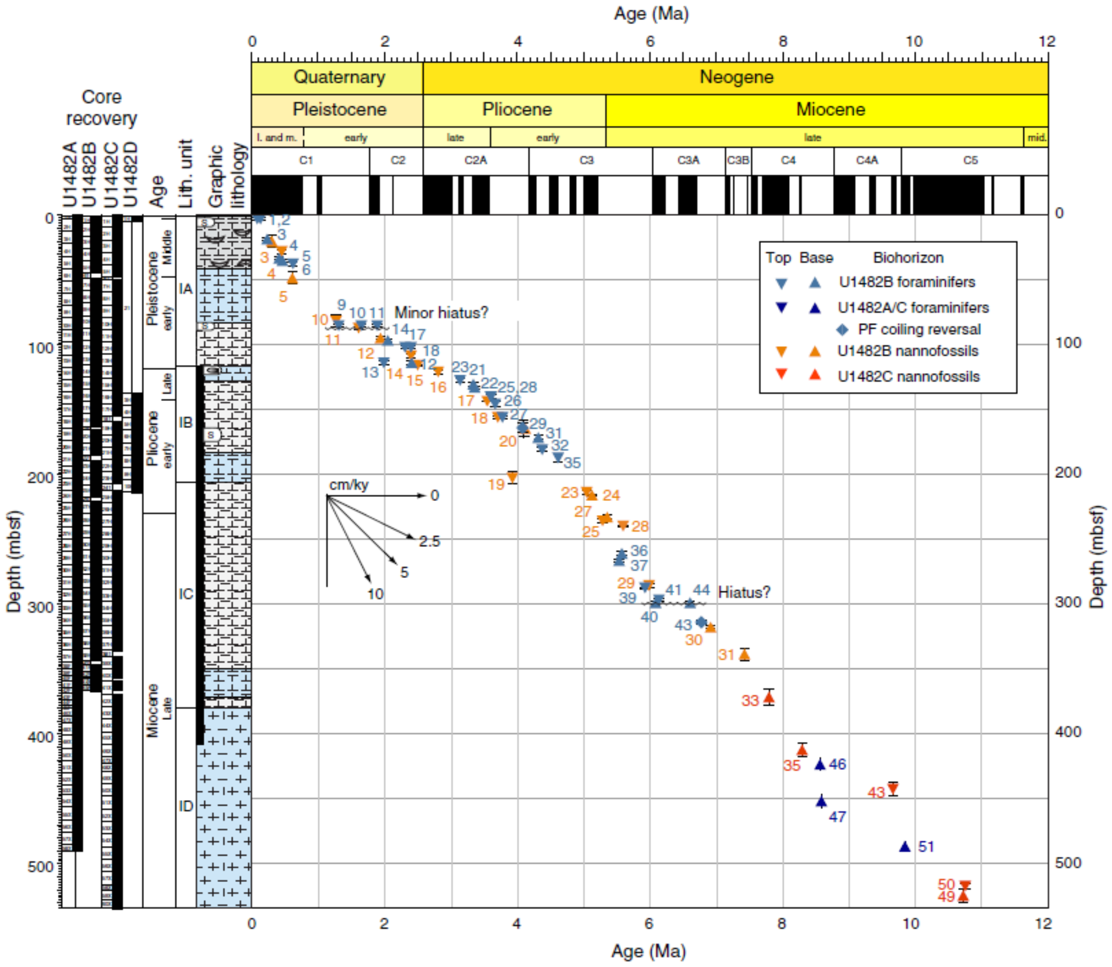

Figure 2.2 The age model image is from Rosenthal et al. (2018), the Y-axis represents depth in meters below sea floor (mbsf),while the X-axis show age. Vertical error bars represent the interval between the two samples that define the bio-horizons.

The detailed late Miocene analysis, with 42 samples from holes A, B, and C, taken from core depths between ~200 and 400 mbsf, covers a time frame between 8.13 Ma and 5.88 Ma (Figure 2.2). Assigned ages are based on an interpolated best-fit third-order polynomial through the shipboard biostratigraphic age constraints (Emma Hanson pers. comm.) and use age calibrations updated to the Geological Timescale (GTS) 2020.

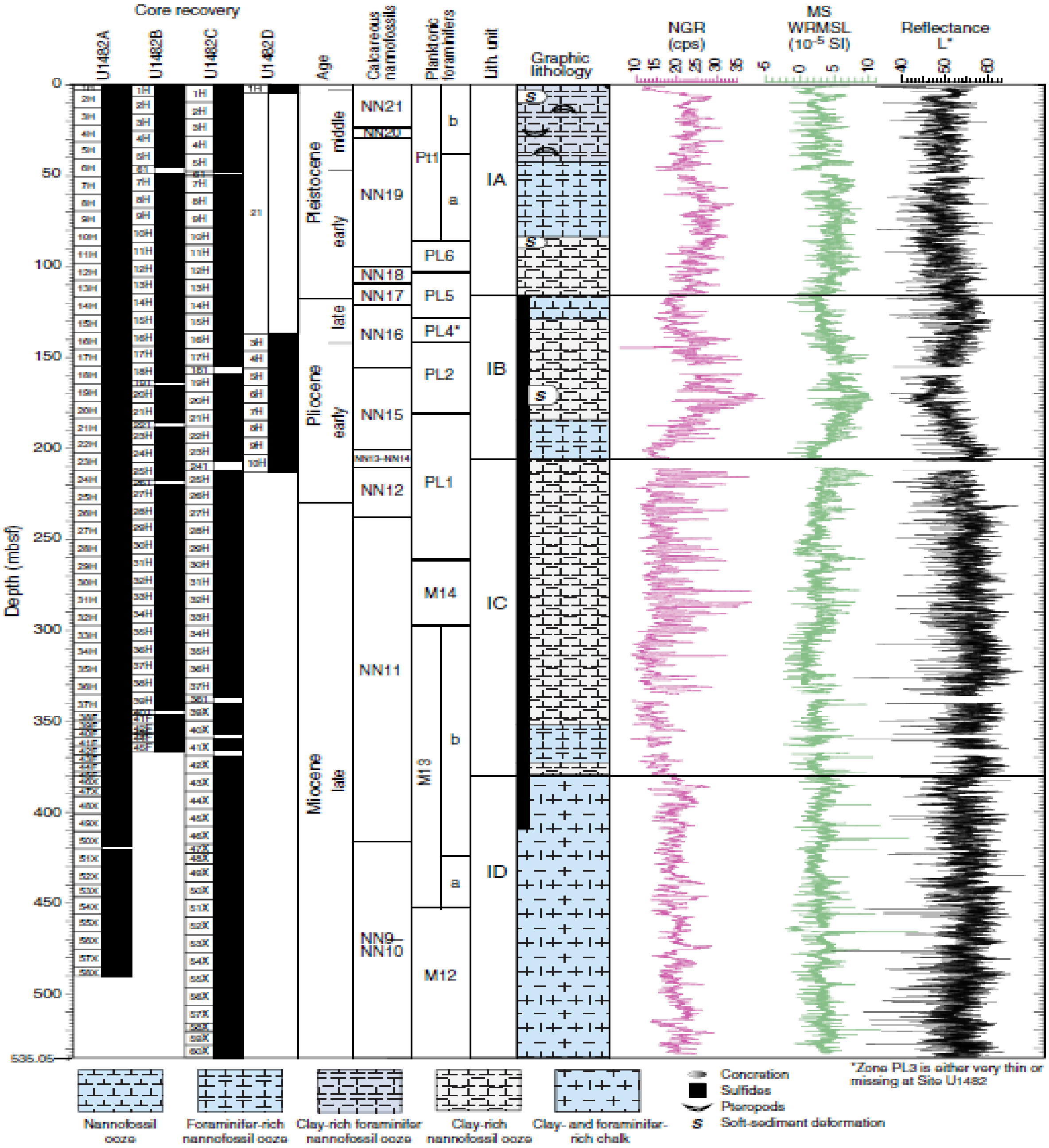

Figure 2.3 This figure provides a lithological summary of IODP Site U1482 from, Rosenthal et al. (2018), showing alternating layers of nannofossil ooze, chalk, and other sediment types. These submeter-scale cycles are critical for understanding sediment deposition and paleoenvironmental conditions during the Late Miocene.

2.2 Preparation of sediment sample

The aim of bulk sediment preparation is to divide the sample into two coccolith size-fraction categories: a very coarse (V.C) and very fine (V.F) coccolith fraction. The process of separating the coccolith fraction (< 20 µm) from the bulk sediment (> 20 µm) is considered straightforward, using a standard 20 µm sieve. However, the task of isolating specific coccolith size fractions within the (< 20 µm) coccolith fraction becomes complex due to their extremely small dimensions. Various separation techniques have been proposed and effectively used in the past few years (Minoletti et al., 2009; Paull & Thierstein, 1987; Stoll & Ziveri, 2002; Zhang et al., 2021). These techniques can broadly be categorized into micro-filtration (Minoletti et al., 2009) and sinking-decanting (Paull & Thierstein, 1987; Stoll & Ziveri, 2002) techniques. For this study, we have employed a novel technique (Hanson, 2023) (shown in Figure 2.4) to isolate coccolith fraction from bulk sediment

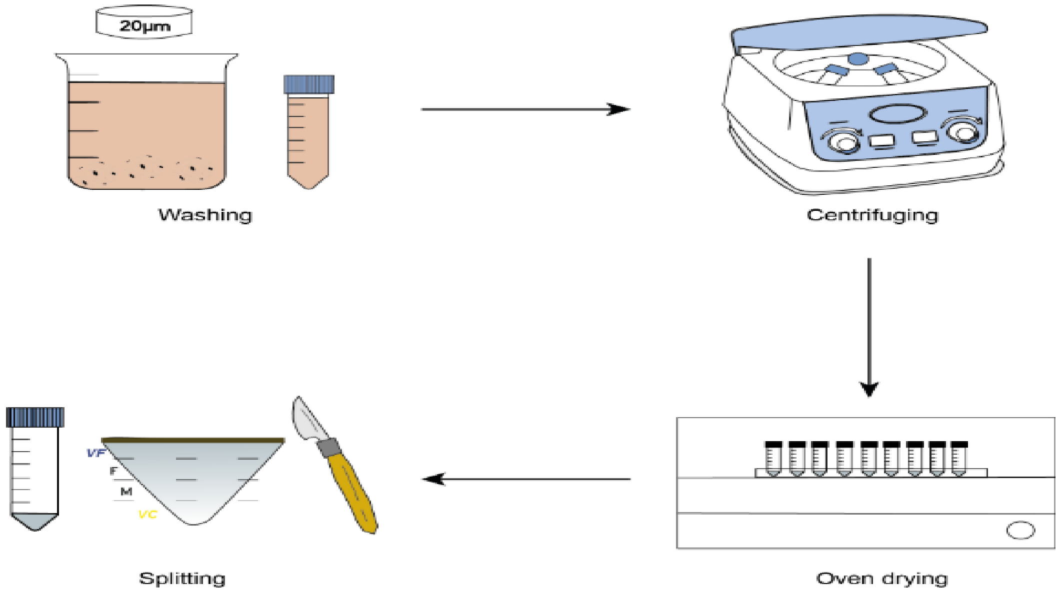

Figure 2.4 This schematic represents the techniques used to isolate very coarse (V.C) and very fine (V.F) coccolith fractions from bulk sediment Hanson (2023). The process includes washing, centrifuging, drying, and separation, which are crucial for generating the distinct size fractions used in isotopic analysis.

because this procedure is highly replicable and straightforward, demanding minimal specialized equipment. This technique is categorized into four key steps washing, centrifuging, drying, and separation (See Figure 2.4).

2.2.1 Washing

Sediment samples measuring two cubic centimeters in volume were taken into a 250 ml glass beaker while retaining a minuscule amount of sample in the original bag for potential future use. Sufficient de-ionized (D.I) water was added to the beaker to submerge the sample and it was left to soak for a duration from 30 minutes to 1 hour to facilitate disaggregation. Subsequently, the samples were rinsed through a 63 µm sieve using DI water until the water became clear, with the < 63 µm fraction suspended in a 1-liter glass beaker and the > 63 µm fraction discarded. The < 63 µm fraction was then subjected to another wash with DI water through a 20 µm sieve until the water was clear, with the < 20 µm fraction suspended and the > 20 µm fraction discarded. The suspended < 20 µm sediment fraction was then transferred to 50-milliliter centrifuge tubes (multiple tubes per sample if necessary). The sieves were meticulously cleaned with DI water and subjected to ultrasonic treatment for about 2 minutes after each sample.

2.2.2 Centrifuging

The centrifuge tubes were loaded into the centrifuge machine and spun at 4,000 rpm for approximately 5 to 6 minutes. After completing the cycle, the clarity of the water was assessed, and if necessary, the tubes were spun for an additional minute. Once sediment had settled at the bottom, the clear water above it was carefully poured off, leaving about <0.5 cm of water above the sediment to avoid disturbing the top layer.

For samples with multiple tubes, they were combined into one by adding enough DI water, then the sediment was resuspended either by shaking or using a vortexer. This final sample tube underwent one last spin at 5,000 rpm for about 6-7 minutes. The clear water was decanted once again, leaving <0.5 cm of water above the sediment to maintain the integrity of the top layer.

2.2.3 Drying

After centrifugation, the tubes containing each sample were positioned upright in a holder and placed in an oven without their lids. Subsequently, the tubes were allowed to air dry overnight at 50°C. Upon completion of drying, the samples resembled broadly triangular 'V' shaped sediment pieces, formed to some extent by the shape of the centrifuge tube's bottom.

I have avoided freeze drying method due to a specific issue and it consumes a lot of time. When subjected to freeze drying, the coccolith fraction formed a fragile bullet shape that easily crumbled and mixed, rendering precise separation impossible (Hanson, 2023). Therefore, the decision was made to utilize the oven drying method instead.

2.2.4 Separation

To initiate the separation process, the bullet-shaped coccolith fraction was delicately removed from the tube and positioned on a piece of filter paper to facilitate easy transfer to the glass vials. Four glass vials were designated and labeled according to the targeted size fractions: very fine (V.F), fine (F), medium (M), and very coarse (V.C). Using a scalpel, the bullet-shaped sample was then divided into these four categories from bottom to top. There was a noticeable variation in color and texture across the size fractions; the V.F fraction appeared significantly consolidated and displayed a darker grey hue, while the V.C fraction exhibited greater friability and lighter grey coloration.

As these extreme categories were earmarked for isotope analysis, distinguishing between them was straightforward as they originated from the upper (V.F) and lower (V.C) sections of the centrifuge tube pellet. The distinct size fractions were then transferred to the appropriately labeled glass vials, and the material was gently re-separated into a powdered form within each vial by gently crushing.

2.3 Particle Size Separation Analysis

Continuing from the innovative separation method outlined earlier, it was necessary to validate the efficacy of the separation and characterize the distribution of coccolith sizes. Previous investigations into separating coccolith size fraction techniques have rarely been conducted through quantitative evaluation, with only a limited number of studies undertaking such rigorous analyses (Stoll & Ziveri, 2002; Zhang et al., 2021). The majority of studies have instead relied on SEM images of the size fraction to showcase the quality of separation (e.g., Hermoso et al., 2015).

For this late Miocene study, 82 slides, comprising 41 very coarse (V.C) coccolith fractions and 41 Very fine (V.F) coccolith fractions, respectively, were prepared. Following the slide preparation technique outlined by Flores & Sierro (1997). This specific technique was selected for slide preparation due to the necessity for particles to be dispersed and to prevent contact between particles that pose a challenge or are impossible to separate in particle size distribution analyses.

2.3.1 Slide Preparation

Sediment samples weighing between 0.005 g and 0.0065 g were transferred into 10.5 ml glass sample vials. A buffered solution containing 0.15 g l^{-1} of sodium carbonate and 0.2 grams per liter of sodium bicarbonate mixed with DI water was added to the sample vials. These vials were then subjected to ultrasonic treatment for 2 minutes at a frequency of 42 kHz. Coverslips were positioned at the bottom of the glass petri dishes, and a mixture of buffer solution and gelatin was poured in until nearly full, close to the dish's edge. The solution in the glass vials was gently agitated, either by shaking or using a vortexer, to resuspend the sediment. After a 2-minute waiting period, 50 µl of this solution was extracted using a micropipette and dispensed onto the coverslip inside the petri dish. The solution was then carefully distributed around the petri dish using the micropipette to achieve a uniform spread over the coverslip and allowed to settle overnight or for a minimum of 8 hours. The next day, excess water was removed by siphoning with strips of tissue, and the coverslip was permitted to air dry before being affixed onto a glass slide using Norland Optical Adhesive.

2.3.2 Microscopy Slide Analysis

The slide samples underwent analysis using a Zeiss Axioscope A.1 microscope at 1,000x magnification, employing circular polarization, and a Märzhäuser Wetzlar motorized XYZ stage. Following the focusing process, a series of continuous imaging was conducted, capturing 20 fields of view with a QI Imaging camera. Concurrently, Microvision Cartograph software facilitated the automatic capture and stitching of sequential image tiles into a single comprehensive image then this image is saved as a tiff file. The resulting exported image encompassed a total area of 0.12 mm^2.

2.3.3 Particle Size Analysis

The exported TIFF images underwent processing utilizing the Fiji (Schindelin et al., 2012), a variant of the open-source ImageJ software specifically tailored for biological-image analysis. Fiji is particularly adept at facilitating particle size distribution analysis, thereby aiding in the comprehensive analysis of the images obtained.

To begin with, the images were initially converted into an 8-bit greyscale format (Figure 2.5), as particle analysis and thresholding steps require this format due to their incompatibility with color images. Additionally, a spatial scale for the images was defined. The images captured using Micro-vision Cartograph software utilized pixels as their standard unit of measurement, with the slides scanned at a scale of 0.03458 µm/pixel under 1,000x magnification. This scale was inputted into the image properties in Fiji, utilizing microns as the units (see Figure 2.6).

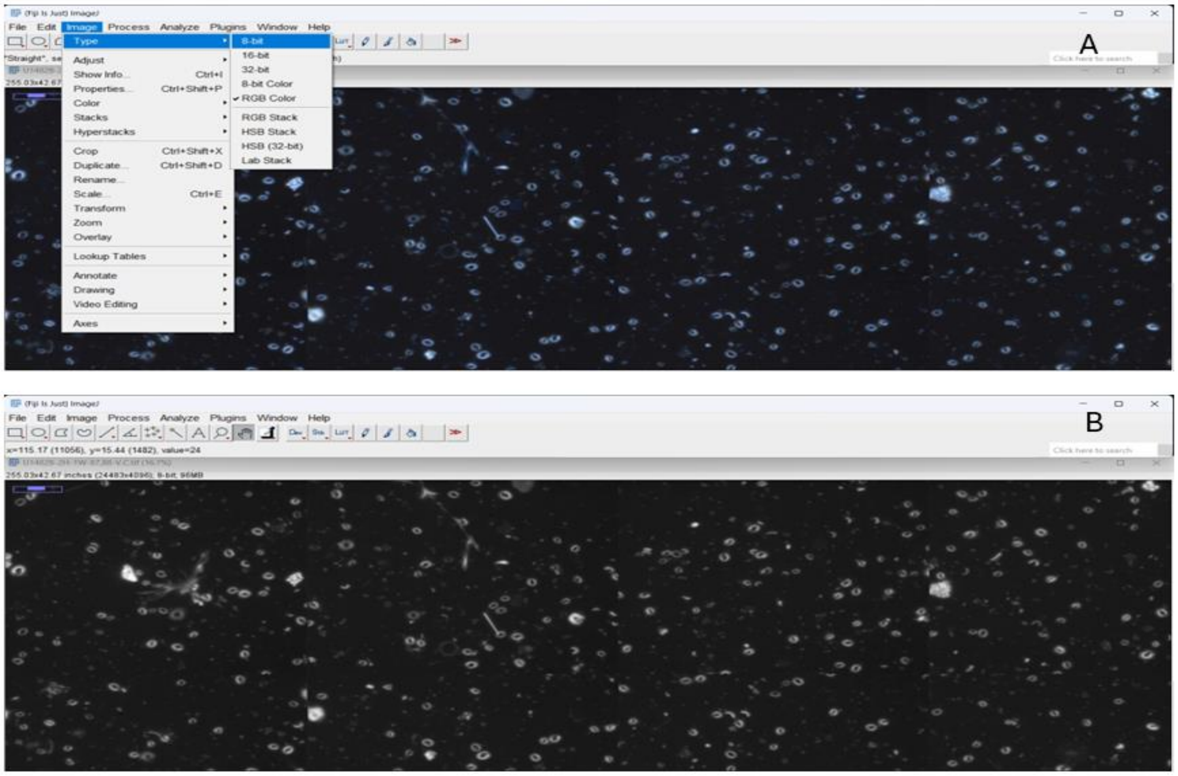

Figure 2.5 Image (A) shows the original Tiff file loaded into ImageJ software, while image (B) displays the 8-bit greyscale version used for particle analysis. Converting the image to 8-bit is essential for accurate thresholding and size distribution analysis.

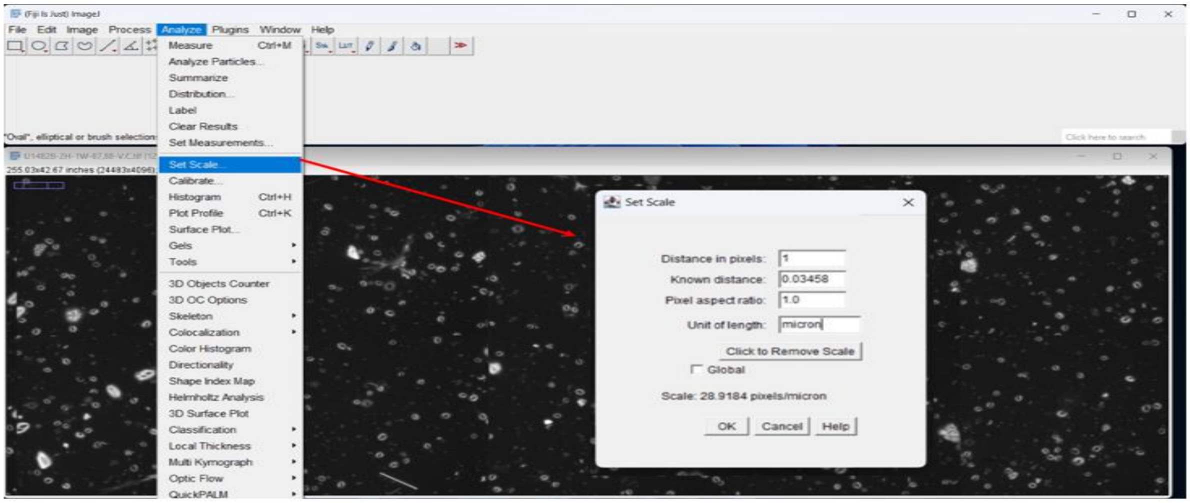

Distance in pixels: 1
Known distance: 0.03458
Pixel aspect ratio: 1.0
Unit of length: micron
☐ Global
Scale: 28.9184 pixels/micron

Figure 2.6This figure illustrates setting the scale for the 8-bit grey image in ImageJ software. Defining the scale is crucial for accurate particle size measurements in subsequent analysis, ensuring that particle areas are calculated in micrometers (µm²).

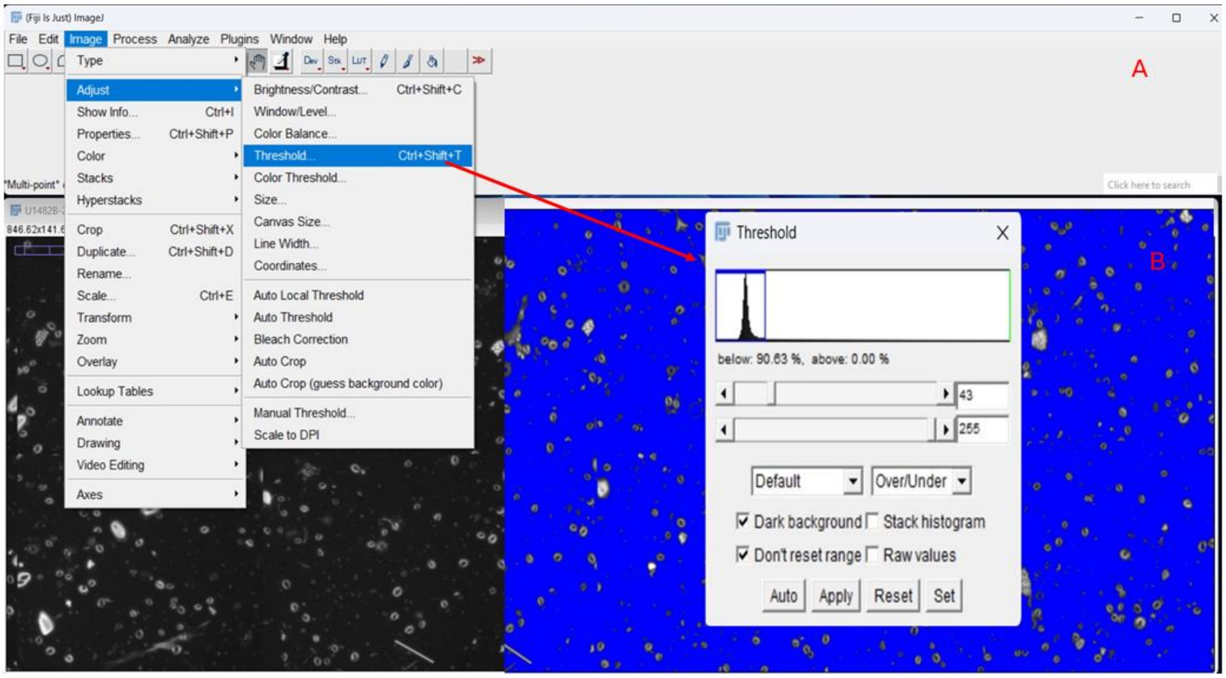

below: 90.63 %, above: 0.00 %
43
255
Default
Over/Under
☑ Dark background ☐ Stack histogram
☑ Don't reset range ☐ Raw values

Figure 2.7 This figure shows the thresholding process in ImageJ, where the slider is used to encapsulate the entire histogram. Thresholding separates particles from the background, which is critical for identifying and measuring coccolith particles in the image.

Thresholding detection was then established using the greyscale image to differentiate the objects of interest (white pixels) from the background (black pixels) (see Figure 2.7 A). While Fiji offers automated threshold determinations, these were found to be inconsistent across all images (Hanson, 2023) Instead, thresholds were set using the histograms generated by Fiji. A threshold encompassing the entire histogram curve was chosen to maintain consistency across samples (see Figure 2.7 B).

Following thresholding, a binary image was generated, highlighting particles (in white) against the background (Dudley et al., 1986). Subsequently, particle size distribution analysis was conducted. Particles with an area larger than 80 μm^2 or less than 1 μm^2 were disregarded due to the limitations of resolving minute coccolith particles with light microscopy and the rarity of very large coccoliths in the material, making large particles more likely to be other biogenic carbonate fragments.

Each particle's area was determined as the total area within the particle margin, including any holes. While hole detection and exclusion within ImageJ are options, for this analysis based on coccolith size, the total coccolith particle area, including any central area 'hole', was considered (see Figure 2.9). The full range of circularity (0.00-1.00) was included in the analysis to account for the diverse shapes of coccoliths, as most are not perfectly circular. The output of the analysis consisted of an image with each particle labeled and numbered, along with a .csv file containing numerical information such as each labeled particle's total area and perimeter.

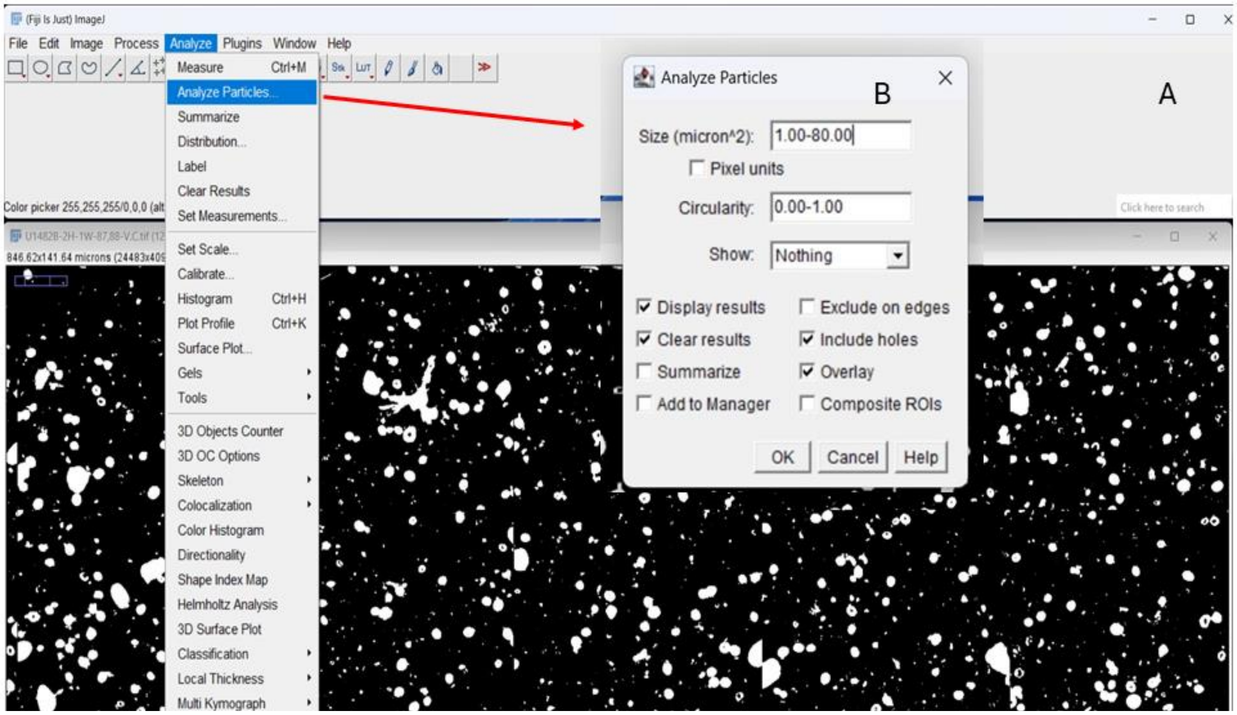

Color picker 255,255,255/0,0,0 (alt

U1482B-2H-1W-87,88-V.C.tif (12

846.62x141.64 microns (24483x409

Analyze Particles

Size (micron^2): 1.00-80.00

☐ Pixel units

Circularity: 0.00-1.00

Show: Nothing

☑ Display results ☐ Exclude on edges

☑ Clear results ☑ Include holes

☐ Summarize ☑ Overlay

☐ Add to Manager ☐ Composite ROIs

Figure 2.9 This figure illustrates setting the particle size detection range in ImageJ software. Particles are selected based on a predefined size range, which excludes any particles too small (<1 µm²) or too large (>80 µm²) to ensure only relevant coccolith particles are measured.

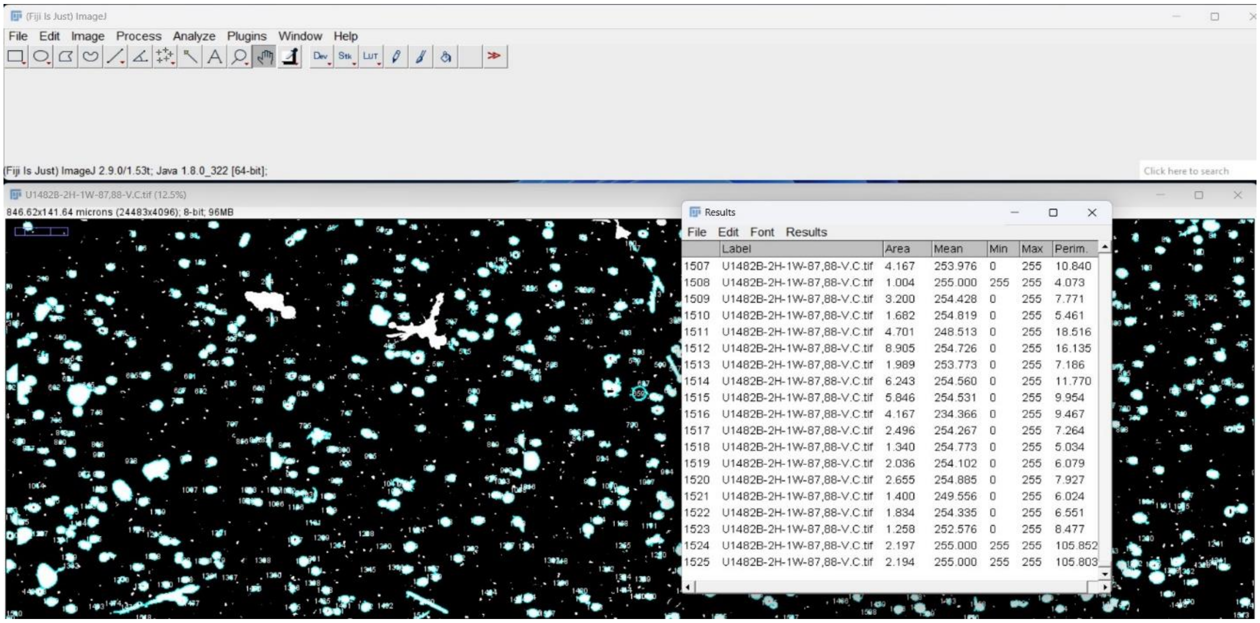

(Fiji Is Just) ImageJ 2.9.0/1.53t; Java 1.8.0_322 [64-bit];

U1482B-2H-1W-87,88-V.C.tif (12.5%)

846.62x141.64 microns (24483x4096); 8-bit; 96MB

	Label	Area	Mean	Min	Max	Perim.
1507	U1482B-2H-1W-87,88-V.C.tif	4.167	253.976	0	255	10.840
1508	U1482B-2H-1W-87,88-V.C.tif	1.004	255.000	255	255	4.073
1509	U1482B-2H-1W-87,88-V.C.tif	3.200	254.428	0	255	7.771
1510	U1482B-2H-1W-87,88-V.C.tif	1.682	254.819	0	255	5.461
1511	U1482B-2H-1W-87,88-V.C.tif	4.701	248.513	0	255	18.516
1512	U1482B-2H-1W-87,88-V.C.tif	8.905	254.726	0	255	16.135
1513	U1482B-2H-1W-87,88-V.C.tif	1.989	253.773	0	255	7.186
1514	U1482B-2H-1W-87,88-V.C.tif	6.243	254.560	0	255	11.770
1515	U1482B-2H-1W-87,88-V.C.tif	5.846	254.531	0	255	9.954
1516	U1482B-2H-1W-87,88-V.C.tif	4.167	234.366	0	255	9.467
1517	U1482B-2H-1W-87,88-V.C.tif	2.496	254.267	0	255	7.264
1518	U1482B-2H-1W-87,88-V.C.tif	1.340	254.773	0	255	5.034
1519	U1482B-2H-1W-87,88-V.C.tif	2.036	254.102	0	255	6.079
1520	U1482B-2H-1W-87,88-V.C.tif	2.655	254.885	0	255	7.927
1521	U1482B-2H-1W-87,88-V.C.tif	1.400	249.556	0	255	6.024
1522	U1482B-2H-1W-87,88-V.C.tif	1.834	254.335	0	255	6.551
1523	U1482B-2H-1W-87,88-V.C.tif	1.258	252.576	0	255	8.477
1524	U1482B-2H-1W-87,88-V.C.tif	2.197	255.000	255	255	105.852
1525	U1482B-2H-1W-87,88-V.C.tif	2.194	255.000	255	255	105.803

Figure 2.8 Data is generated for each particle in a .csv format, including values such as area, perimeter, and circularity.

2.4 Stable Isotope Analysis

Stable isotope analysis was carried out on split samples from the late Miocene study, specifically targeting the V.F and V.C fractions. These analyses were conducted at the BGS Stable Isotope Facility in Keyworth, Nottingham, using a VG Optima mass spectrometer with standard reproducibility of < ± 0.1%. All recorded data were calibrated to the Vienna Pee Dee Belemnite (VPDB) standards for consistency. Before analysis, the samples underwent a plasma ashing process at BGS, a widely accepted method for removing organic matter from samples prior to carbonate stable isotope analysis.

The sample material was then powdered to generate enough CO_2 equivalent to 10 μg of pure calcite. The sample was subsequently reacted with anhydrous phosphoric acid under vacuum conditions at a constant temperature of 25°C overnight. The resulting liberated CO_2 was separated from water vapor under vacuum and collected for further analysis.

2.4.1 Carbon Isotope Analysis

Carbon exists naturally in three isotopic forms, with two being stable (^{12}C and ^{13}C) and one radioactive (^{14}C). These isotopes are present in varying concentrations in the natural environment, with ^{12}C dominating at 98.9%, ^{13}C at 1.1%, and trace amounts of ^{14}C. The presence of radioactive ^{14}C is utilized in radiocarbon dating of organic materials, a widely employed technique in geological, archaeological, and paleontological studies. The $^{13}C/^{12}C$ ratio of a sample, whether it is bulk sediment or foraminifera, is determined and compared to the $^{13}C/^{12}C$ ratio of a known standard, typically laboratory standard calcite. Carbon isotopes ($\delta^{13}C$) are expressed as a per mill (‰) difference to the VPDB standard using the equation provided.

$$\delta^{13}C = \frac{{}^{13}C/{}^{12}C_{sample} - {}^{13}C/{}^{12}C_{standard}}{{}^{13}C/{}^{12}C_{standard}} \times 1000$$

2.4.2 Oxygen Isotope Analysis

Oxygen exists naturally in three stable isotopic forms: ^{16}O, ^{17}O, and ^{18}O, with varying concentrations in the environment. Specifically, ^{16}O predominates at 99.763%, followed by ^{17}O at 0.0375%, and ^{18}O at 0.1995%. The $^{18}O/^{16}O$ ratio of a sample is determined and compared to that of a known standard, typically a laboratory standard calcite. Oxygen isotopes ($\delta^{18}O$) are expressed as per mill (‰) relative to this standard, with positive values indicating enrichment of the heavier isotope compared to the standard, while negative values signify a depletion of the heavier isotope.

$$\delta^{18}O = \frac{{}^{18}O/{}^{16}O_{sample} - {}^{18}O/{}^{16}O_{standard}}{{}^{18}O/{}^{16}O_{standard}} \times 1000$$

3 Results

The sample age range spans from 8.13 Ma to 5.88 Ma, with a total of 84 samples analyzed – the very coarse and very fine coccolith fractions from 42 original sediment samples. Two samples were excluded from the size separation analysis because of persistent drying effects observed on the sample slides that inhibited clear viewing although sample fractions were still analyzed for stable isotopes study - U1482C-40X-4W-33/36 V.C and U1482B-45F-3W-24/26 V.F.

3.1 Particle Size Separation Analysis Results

In this study a size separation technique was employed on bulk sediment samples to produce very coarse (V.C) and very fine (V. F) coccolith fractions for coccolith size and isotope analyses. The particle size distribution for each fraction was analyzed and represented through cumulative percentage plots (Figure 3.1) (see Appendix for rest of the plots). See (Figure 3.2) for examples of bad separation and bad scans. This could be due to the unevenness of the slide or in some cases, uneven distribution of particles, especially smaller ones.

Our analysis revealed distinct differences between the V.C and V.F coccolith fractions across most samples. The cumulative distribution curves consistently showed a higher cumulative percentage for smaller coccoliths in the V.C fractions compared to the V.F fractions, indicating a greater abundance of smaller coccoliths within the V.C samples. The average area of particle size for all V.C fractions was measured at 6.36 μm^2, with a range spanning from 3.81 μm^2 to 11.31 μm^2. The average area for all V.F fractions was 4.70 μm^2, with a range from 2.17 μm^2 to 8.72 μm^2.

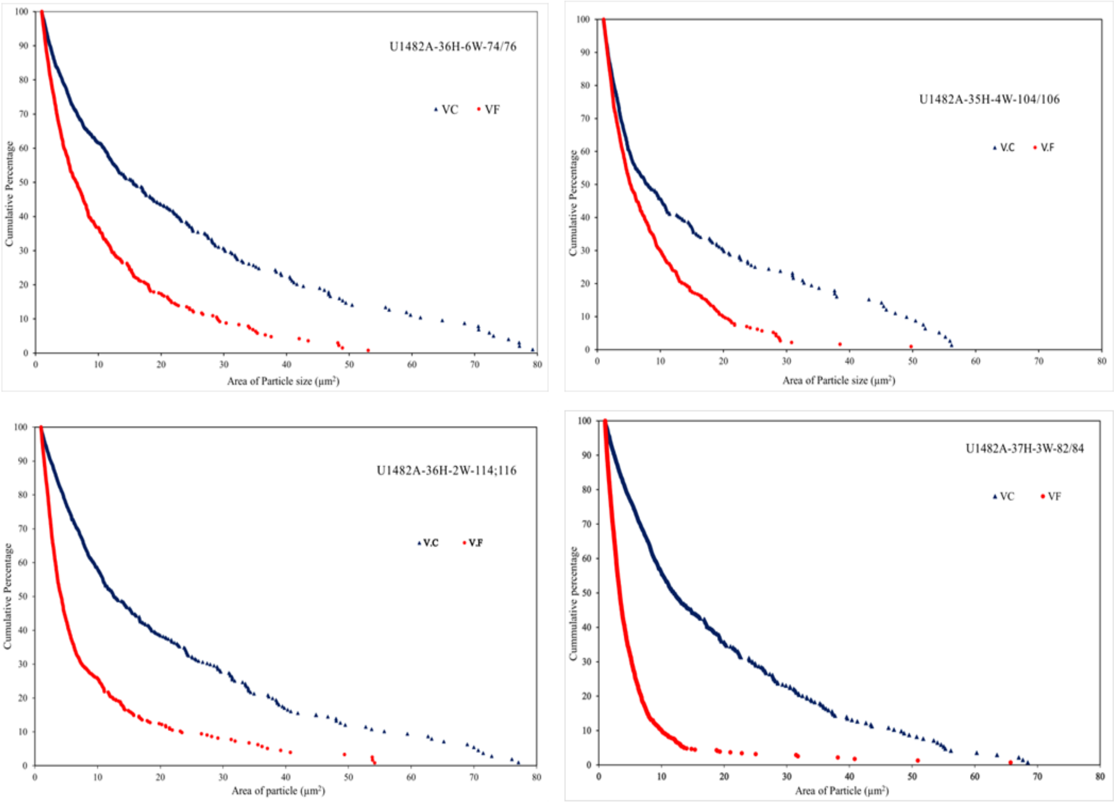

Figure 3.1 Cumulative percentage versus particle size (µm²) distributions for different sediment samples. Blue triangles represent the coarse fraction (V.C), and red circles represent the fine fraction (V.F). The x-axis shows particle size in µm², and the y-axis represents cumulative percentage, highlighting the variation in particle size distribution across samples.

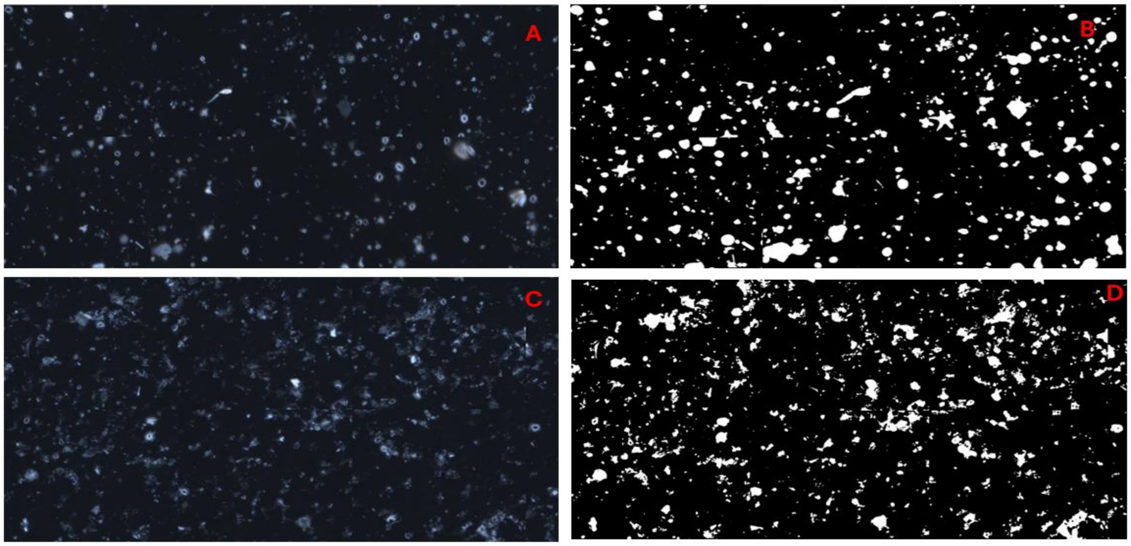

Figure 3.2 Illustration of good vs bad scan and the threshold image it set. Sample U1482A-37H-3W-82/84 V.C (A & B): Image A shows a circular polarized view, while image B displays the threshold applied using Fiji software to distinguish between particles. Although there are very few noticeable unusually large particles, they will be excluded when we set the required size range. This is an example of a high-quality image, with clear and distinct particles without frosting effect. Sample U1482A-37H-5W-24/26 V.F (C & D): over here, C represents a circular polarized image, and D shows the threshold set by Fiji software. In this sample, we can notice that most particles are concentrated closely and produce frosted effect.

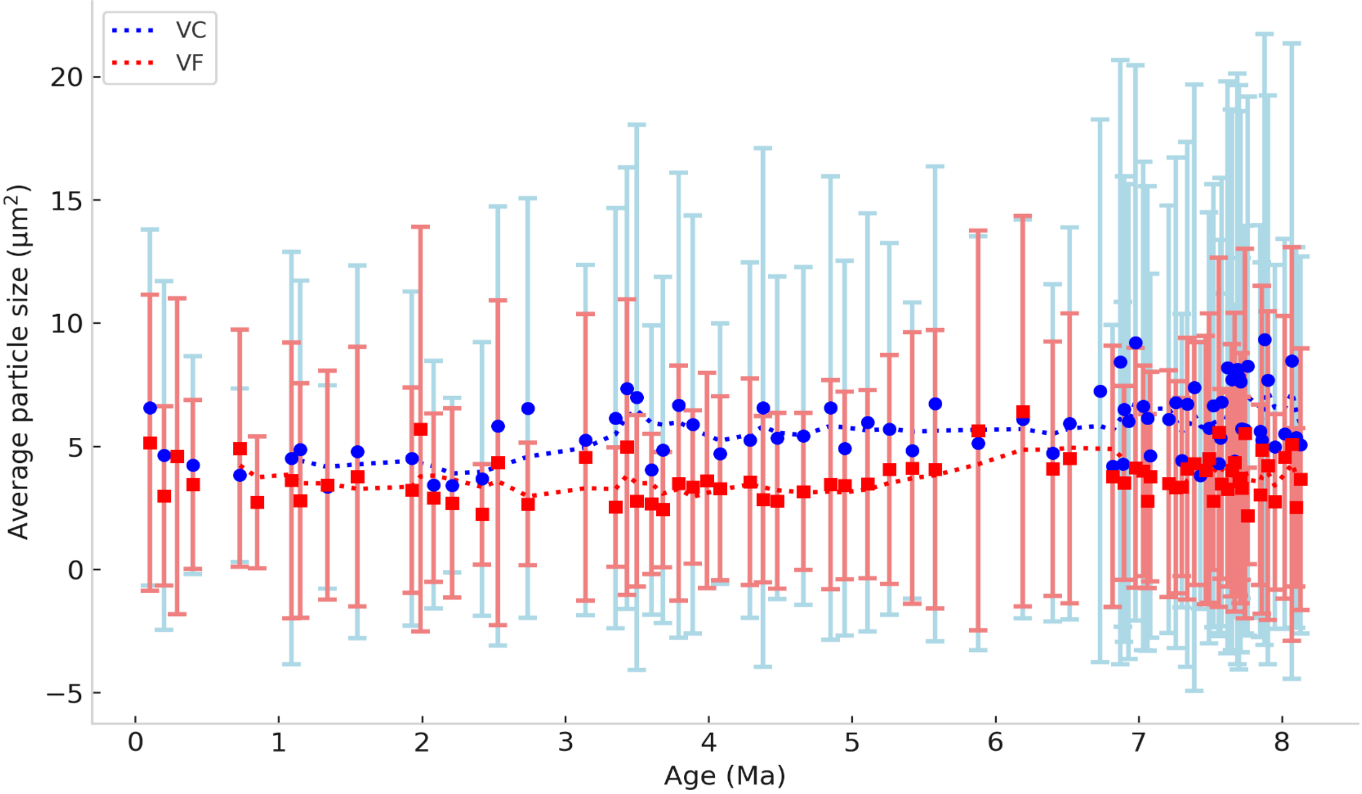

Figure 3.3 This figure shows the mean particle size (µm²) of very coarse (V.C) and very fine (V.F) coccolith fractions over time (Ma). The V.C fraction is represented with larger particle sizes, and the V.F fraction has smaller sizes, with error bars indicating variability within the samples.

out of 36 samples that are plotted, Cumulative plots of 9 samples show poor size separation (see Appendix B), this could be due to human-induced error during the physical separation of the bullet-shaped coccolith (discussed in 2.2.4) or due to imperfect separation with the centrifugation method. This method does not uniformly separate particles by size but relies on the faster settling of larger particles, with the final particle size distribution at the base of the centrifuge tube influenced by both the settling velocity of each particle (related to size) and the particle's initial distance to the base. Smaller particles near the base can mix with larger particles due to their shorter travel distance, leading to a preferential distribution of larger coccoliths at the bottom and smaller ones at the top, although this separation is not perfect (Hanson, 2023).

The plot of the mean particle size (μm^2) with Age (Ma) (Figure 3.3), reveals a clear distinction between the V.C and V.F fractions. The V.C data consistently exhibit higher mean particle sizes compared to the V.F data across all the samples. The error bars, representing standard deviation, indicate some variability within each group, with occasional overlap. However, the overall trends demonstrate successful separation. Moving average lines for both fractions further highlight distinct trends, with the V.C mean particle size remaining consistently above that of the V.F. This effective separation is evident from younger sediments to older age groups, confirming the efficacy of the experimental method in differentiating between very coarse and very fine particles. The separation is particularly clear in the youngest and oldest sediments, with less variability and overlap, showcasing the method's robustness across varying age ranges.

3.2 Carbon Isotope Analysis

We examined the distribution of carbon isotopes within late Miocene samples, dating from 8.13 Ma to 5.88 Ma. The carbon isotope data ($\delta^{13}C$ ‰ VPDB) shows variability over time, with noticeable trends in the dataset (Figure 3.4).

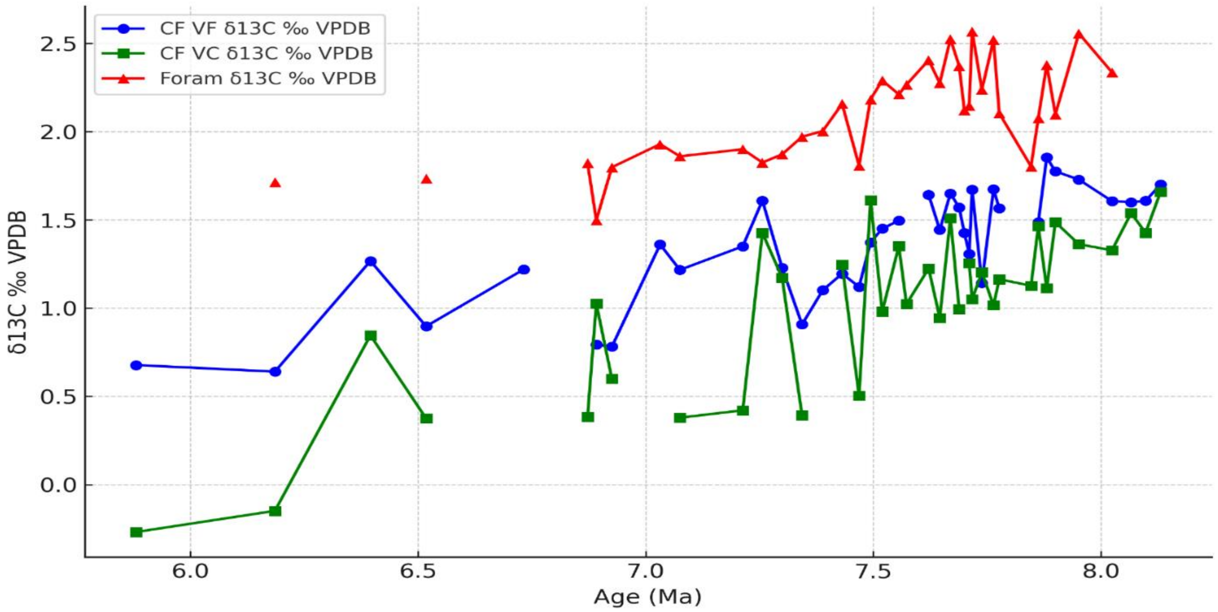

Figure 3.4 Carbon isotope composition of planktic foraminifera *Trilobatus sacculifer* and the two coccolith size fractions (V.C and V.F).

Each sample type (V.C, V.F, and foraminifera) fluctuates across different ages and shows an overall decreasing trend from 8.13 Ma to 5.88 Ma. The *Trilobatus sacculifer* (planktic foraminifera) δ^{13}C foram values are the most positive of the three records, showing a general decreasing trend over the observed period, starting with values between ~2.0 and 2.5‰ at ~7.5 and 8.0 Ma, which then decline to values consistently below 2.0‰ after ~7.4 Ma, before reaching a minimum of 1.50‰ at 6.8 Ma. The V.F coccolith fraction δ^{13}C ($\delta^{13}C_{V.F}$) is offset to lower values from the *T. sacculifer* δ^{13}C values by ~0.5 to 1.0‰ throughout the record, with $\delta^{13}C_{V.C}$ values ranging from ~0.6‰ to 1.9‰. The $\delta^{13}C_{V.F}$ also shows the general decreasing trend through the study interval, although with more variability than the planktic foraminifera data, for example, the interval of four low values between ~7.3 and 7.5 Ma.

3.3 Oxygen Isotope Analysis

All of the late Miocene oxygen isotope records show more stability over the whole period 8.13 Ma to 5.88 Ma than the $\delta^{13}C$ records, although with small scale fluctuations in the data (Figure 3.5).

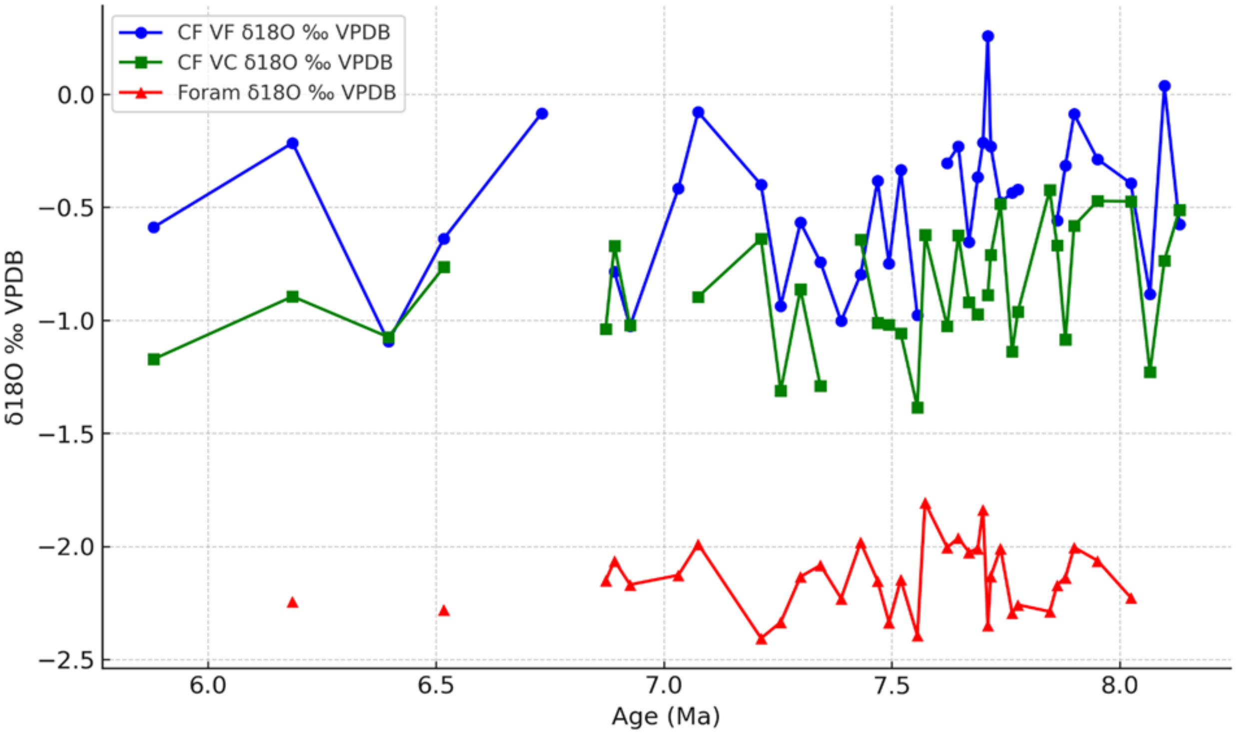

Figure 3.5 Oxygen isotope composition of planktic foraminifera *Trilobatus sacculifer* and the two coccolith size fractions V.C and V.F.

There are some gaps within the data across all three sample types, with some analyses failing due to insufficient cooling in the external cold finger of the isotope gas line. The $\delta^{18}O_{Foram}$ records values are consistently more negative than the coccolith fractions, by ~1‰ or more, and vary between -2.40‰ and -1.80‰ with a range of 0.59‰, although with no overall trend across the whole record. The $\delta^{18}O_{V.F}$ values are the most positive of the three records, with offsets from the $\delta^{18}O_{V.C}$ fraction of up to 0.5‰ for most of the record, but in some instances up to ~1‰.

Overall, $\delta^{18}O_{V.F}$ ranges from ~0 to -1‰, which is a positive offset of ~1 to 1.5‰ from $\delta^{18}O_{foram}$. The $\delta^{18}O_{V.C}$ data is similar to the $\delta^{18}O_{V.F}$ but with an ~0.5‰ positive offset, with value ranging from -1.35‰ at ~7.5 Ma to -0.42‰ at ~7.8 Ma. The $\delta^{18}O_{V.C}$ values also show significant fluctuations between 8.1 Ma – ~7 Ma, followed by a slight decreasing overall trend.

4 Discussion

4.1 Size Changes

The findings of this study indicate that the newly implemented size separation technique has proven to be effective (Figure 3.3). Throughout the entire dataset, the average particle size of the V.C fraction (μm^2) consistently exceeds that of the V.F fraction (μm^2). Additionally, there is a noticeable trend in the size variation of larger coccoliths from 8 million years ago (Ma) to the present. Specifically, larger coccolith sizes were prevalent between 8 Ma and 7 Ma, medium sizes were dominant from 7 Ma to 3 Ma, and from 3 Ma to the present, smaller coccoliths have been observed. Our findings are consistent with those of Bolton et al. (2016), who studied two tropical sites – ODP Site 925 in the western Atlantic and NGHP-01-01A in the Kerala-Konkan basin of Arabian sea - also observed a similar trend in the reduction of coccolith sizes from 8 Ma to 5 Ma. The correlation between those sites and IODP Site U1482 in the eastern central Indian Ocean, strengthens the evidence for a widespread pattern of coccolith size changes, suggesting a potential common driving factor influencing different tropical regions.

The selection against coccolithophore species with larger cell sizes – reflected in the coccolith size records - are interpreted to be driven by constraints on the extent of calcification, influenced by environmental CO_2 levels. The view of previous studies (Bolton et al., 2016; Bolton & Stoll, 2013; Suchéras-Marx & Henderiks, 2014) is that CO_2 levels declined during the late Miocene, and this was the driver of the onset of differences in the $\delta^{13}C$ values of large- to small-coccolith size fractions, indicating different strategies for using carbon.

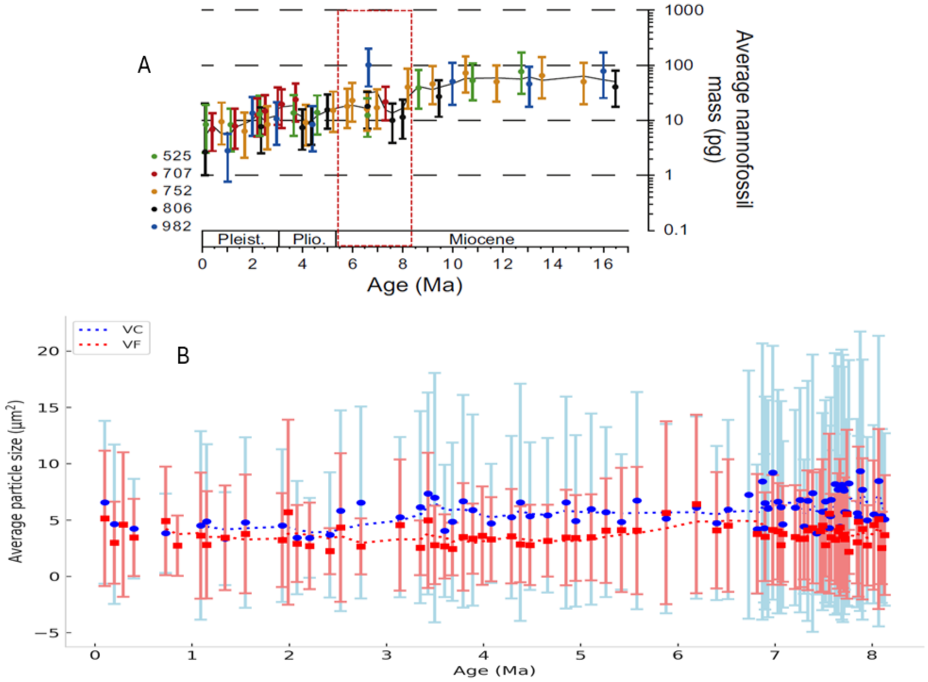

Figure 4.1 This figure consists of two sections: (A) the average nannofossil mass (in picograms) over time from 16 Ma, with error bars representing minimum and maximum values from, Suchéras-Marx and Henderiks (2014). The rectangle highlights the age range that coincides roughly with the samples from this study. (B) shows the average particle size for both very coarse (V.C) and very fine (V.F) coccolith fractions, with error bars indicating variability within the measurements.

In this explanation, larger coccolithophores have a greater surface area-to-volume ratio, making them more sensitive to changing CO_2 levels during the diffusive uptake of DIC from seawater. When carbon availability is limited, these larger species rely more heavily on bicarbonate (HCO_3^-) for photosynthesis, consequently leaving less bicarbonate available for calcification. The production of larger, heavily calcifying coccoliths thus involves spending more energy under low CO_2 conditions, and as this energy cost for calcification increases, the production of smaller coccoliths by smaller cells becomes more advantageous. The evolutionary response of coccolithophores during low CO_2 conditions is a selection for smaller cell sizes (Suchéras-Marx & Henderiks, 2014). The overall smaller size shift from 8 Ma to 5.5 Ma from our data set coincides with the increase in the relative abundance of smaller coccoliths from 9 Ma – 4 Ma ago (Figure 4.1), suggesting that the evolution of coccolithophores to smaller sizes, for more effective utilization of available carbon during low CO_2 conditions, was a successful strategy to maintain higher rates of productivity and calcification.

4.2 Carbon Isotope Changes

Both the planktic foraminifera isotopes and coccolith isotopes (V.C and V.F) show a decreasing trend towards more negative values throughout the period from 8 Ma to 5.5 Ma. There is a

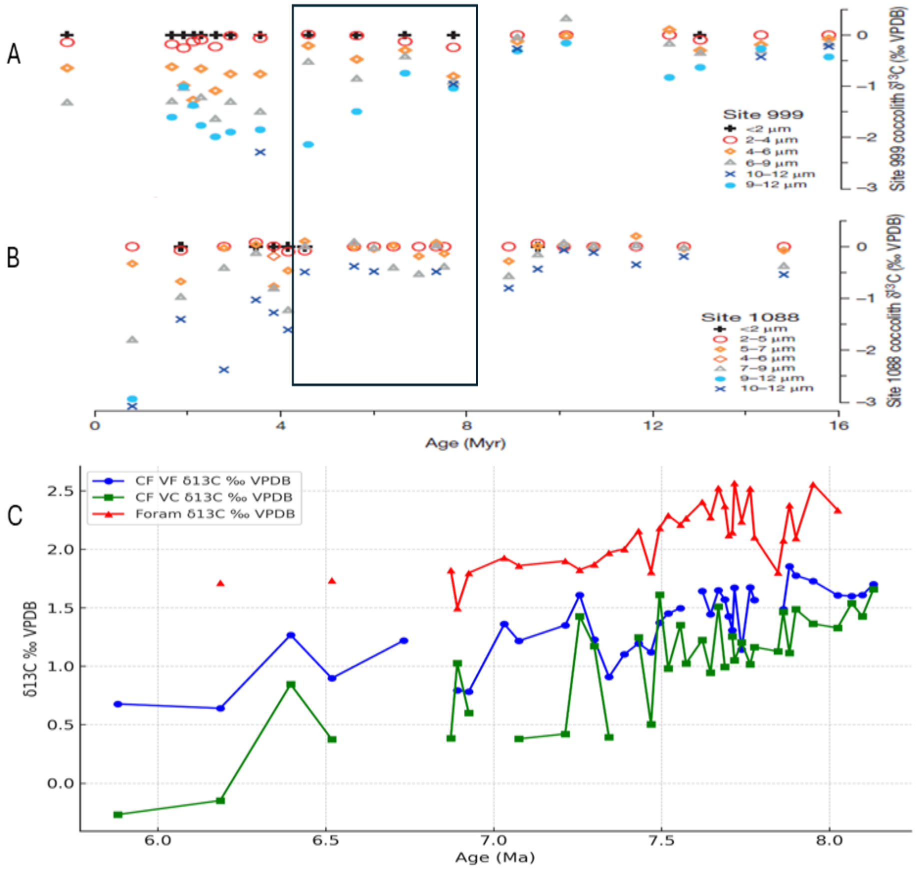

Figure 4.2 This figure shows $\delta^{13}C$ values plotted for three different sites: (A) ODP Site 999 and (B) ODP Site 1088 from, Bolton and Stoll (2013), and (C) IODP Site U1482 (from this study). The Y-axis represents $\delta^{13}C$ values (‰ VPDB), and the X-axis shows age (Ma). The rectangle shows the approximate age of this study samples.

noticeable offset around ~ 8 Ma between the coccolith size fractions, and another offset of ~ 7.2 Ma and from this point, the offset continues to increase. $\delta^{13}C_{V.F}$ is always more positive than $\delta^{13}C_{V.C}$. The planktic foraminifera isotope values show a decreasing trend until ~6.8 Ma and then seem to remain stable for the rest of the record.

We have compared our isotopic fractions records against Bolton et al (2016) (Figure 4.2), and our findings confirm and follow the significant $\delta^{13}C$ isotopic offset between large and small coccolith size fractions from 8.13 Ma to 5.5 Ma, aligning with the trends documented by Bolton and Stoll (2013) and Bolton et al. (2016) (Figure 4.2). Our high-resolution data fills the gaps between data points in Bolton et al. (2016). The differences between the expected isotopic values of inorganic calcite and those of the large and small coccolithophores size fractions are known as 'vital effects' (Bolton & Stoll, 2013; Dudley et al., 1986). Larger coccoliths show more isotopic variations due to their increased dependence on bicarbonate for photosynthesis under low CO_2 levels whereas, smaller coccoliths typically exhibit more stable isotopic signatures and with values closer to inorganic calcite (/planktic foraminiferal calcite) because they are less affected by CO_2 limitations due to their lower surface area to volume ratio. The emergence of a significant isotopic offset in Bolton and Stoll (2013) is ~7 Ma ago (Figure 4.2) but in our records, the offset begins earlier ~8 Ma ago. In Figure 4.4, the IODP site U1482 $\delta^{13}C$ isotopic data is compared against the Mass Accumulation rates of carbonate from the Atlantic sites (Drury et al., 2021), Pacific (Gastaldello et al., 2024), and eastern Equatorial Pacific (Lyle et al., 2019) as a marker for the timing of the LMBB. This comparison shows that the main phase of isotopic divergence in the IODP site U1482 records matches closely with the onset of biogenic bloom from ~8 to 7 Ma (see Figure 4.4).

In the modern ocean, IODP Site U1482 in the eastern equatorial Indian Ocean has the lowest surface ocean DIC, followed by ODP Site 999 in the Caribbean Sea, and then ODP Site 1088 in the Southern Ocean (Wu et al., 2019) (Figure 4.3). It is likely that the same relative spatial pattern of surface ocean DIC held in the late Miocene between these sites, which is consistent with a pattern of inferred carbon limitation from the magnitude and or the timing of the onset of small-to-large coccolith δ^{13}C offsets. For example, IODP Site U1482 shows the small-to-large coccolith isotope offset first at ~8 Ma, followed by ODP Site 999 at ~7 Ma, whilst ODP Site 1088 in the high DIC surface waters of the Southern Ocean, (see Figure 4.3) still shows relatively little isotope fractionation from small-to-large coccoliths.

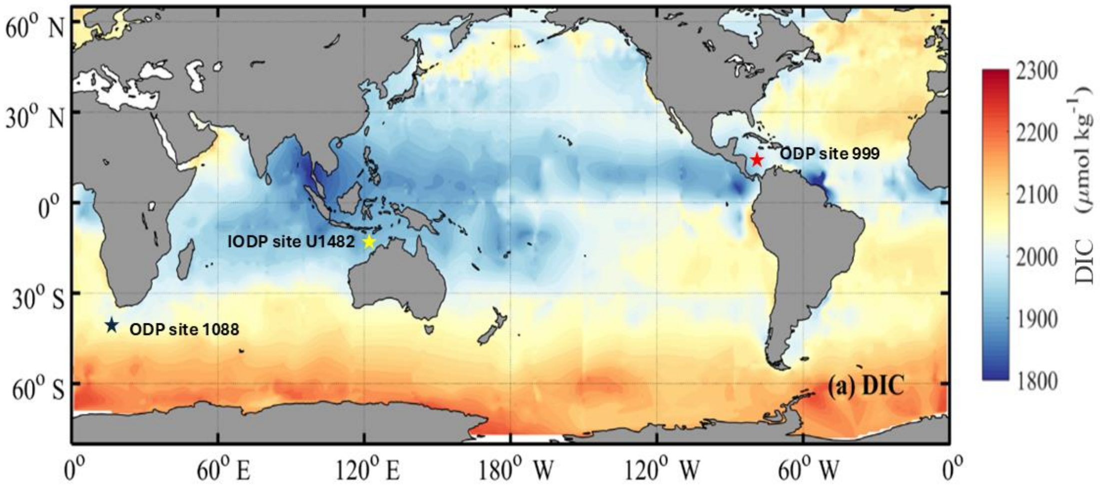

Figure 4.3: Dissolved Inorganic Carbon (DIC) concentrations in the global oceans. This map shows modern-day DIC distribution, with IODP Site U1482, ODP Sites 999 and ODP 1088 marked for reference. The color gradient represents DIC concentrations in μmol/kg, highlighting areas of high and low DIC, which are essential in studying past ocean carbon cycling and productivity changes during the late Miocene. from, Wu et al. (2019).

The timing of the start of the $\delta^{13}C_{V.F}$ to $\delta^{13}C_{V.C}$ offset in IODP Site U1482 and ODP Site 999, between 8 Ma and 7 Ma, is consistent with the start of the LMBB and does not align well with any

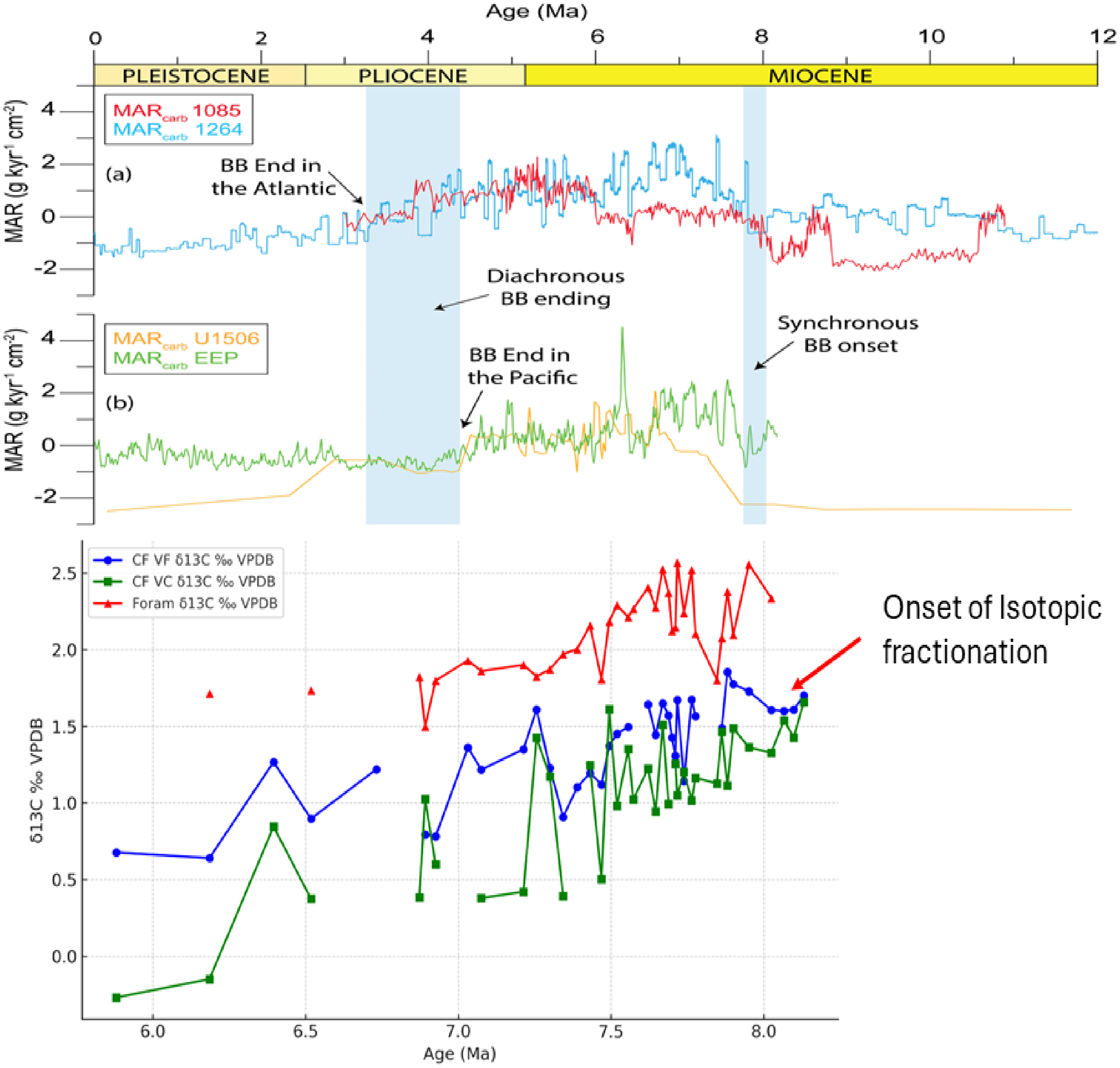

Figure 4.4 Image from, Gastaldello et al. (2024), compares mass accumulation rates of carbonate (MAR$_{carbonate}$) across the Atlantic and Pacific against the δ^{13}C values from the IODP site U1482 (Indian Ocean).

significant change in atmospheric CO$_2$ concentrations or shift in the global climate from benthic foraminiferal oxygen isotope data (Steinthorsdottir et al., 2021a). Together with the pattern of the size of small-to-large coccolith δ^{13}C offsets with site-specific DIC noted above, it is judged more likely that the development of $\delta^{13}C_{V.F}$ to $\delta^{13}C_{V.C}$ offset in the late Miocene is related to increased productivity, especially at tropical to sub-tropical ocean locations, a strengthening of carbonate export – as show with increased carbonate mass accumulation rates – and an increased biological pump resulting in the lowering of surface ocean DIC (Figure 4.3). In this case, coccolith isotopic offsets need to be interpreted in terms of global atmospheric CO_2 concentrations and changes in surface ocean productivity.

4.3 Changes in Oxygen Isotopes

All of the late Miocene oxygen isotope records show more stability over the whole period 5.88 Ma to 8.13 Ma than $\delta^{13}C$ records, although with small-scale fluctuations in the data. The $\delta^{18}O_{foram}$ records exhibit values that are consistently more negative than the coccolith fractions by ~1‰ or more, with variability of 0.59‰ and no overall trend. The $\delta^{18}O_{V.F}$ values are the most positive among the three records, with offsets from the $\delta^{18}O_{V.C}$ fraction up to 0.5‰ for most of the record, occasionally reaching around 1‰ and from the $\delta^{18}O_{foram}$ values by 1‰ to 1.5‰ positive offset (Figure 3.5). The $\delta^{18}O_{V.C}$ data closely resembles the $\delta^{18}O_{V.F}$ but with an ~0.5‰ positive offset, ranging from -1.35‰ at ~7.5 Ma to -0.42‰ at ~7.8 Ma.

The $\delta^{18}O$ offsets between the $\delta^{18}O_{V.C}$, $\delta^{18}O_{V.F,}$ and $\delta^{18}O_{foram}$ can be compared against data from culture studies shown in Figure 4.5 , which also includes data for inorganic calcite and can be used as an approximation to planktic foraminiferal $\delta^{18}O$. The late Miocene data show that $\delta^{18}O_{V.C}$ is offset from $\delta^{18}O_{foram}$ to heavier values by ~1‰, and the $\delta^{18}O_{V.F}$ is slightly, but consistently, heavier than the $\delta^{18}O_{V.C}$ Compared to the modern culture data, this would put both the V.C and V.F fraction as being predominantly composed of the isotopically heavy group dominated by modern species such as *Emiliania huxleyi and Gephyrocapsa oceanica*. From unpublished assemblage data of

IODP Site U1482 (Jones, 2021), more than 50% of coccoliths in the late Miocene of the IODP site U1482 are reticulofenestrids – part of the same family as modern *Emiliania* and *Gephyrocapsa* species. In the late Miocene, these coccoliths of the genus *Reticulofenestra* span a larger size range, of up to 10 µm in some cases, and are abundant in both V.F and V.C size fractions. On this basis, we conclude that the dominant $\delta^{18}O$ isotopic signature of both V.F and V.C fractions come from these *Reticulofenestra* coccoliths and, like their modern descendants, these coccolith have a distinct positive $\delta^{18}O$ signature relative to inorganic (planktic foraminifera) calcite. These results show that the $\delta^{18}O$ signature of the heavy group is not a recently evolved feature of the dominant, small cell, Plio-Pleistocene *Gephyrocapsa* and *Emiliania* species.

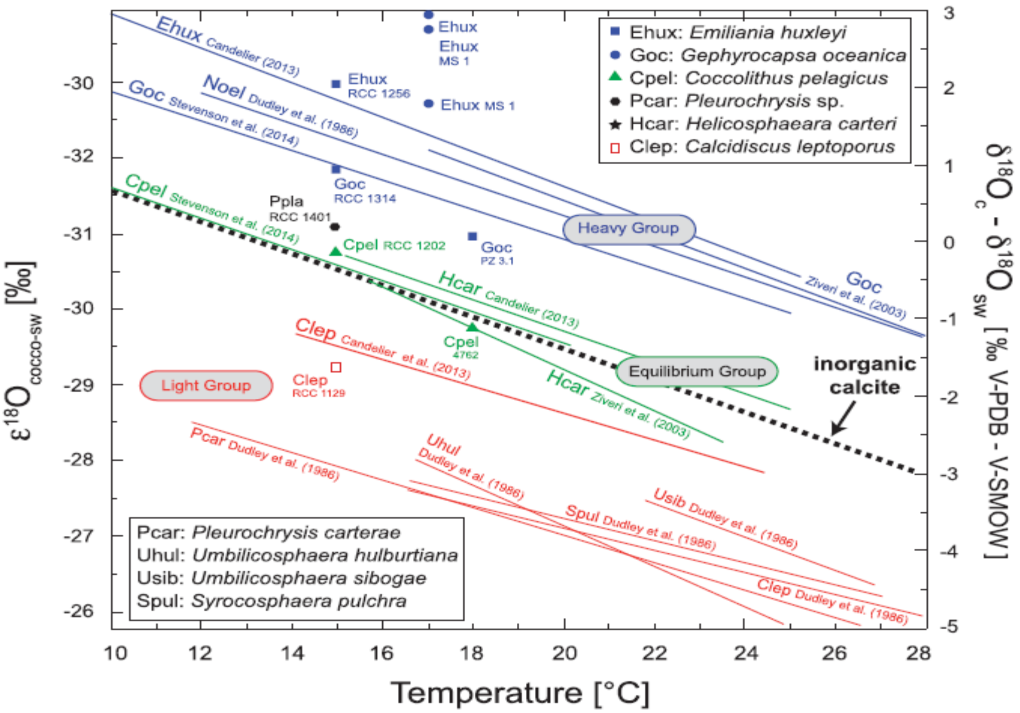

Figure 4.5 Image from, Hermoso (2014), showing the compilation of existing oxygen isotopic values of cultured coccoliths against a broad temperature spectrum on the horizontal axis. The Y-axis on the left $\varepsilon^{18}O$ represents the oxygen isotope fractionation of coccolith relative to seawater, measured in permil (‰) and Y-axis to the right represents the difference in $\delta^{18}O$ between the calcite in coccoliths and seawater, again measured in permil (‰). The plot includes data for various coccolithophore species, grouped into "Heavy," "Light," and "Equilibrium" groups, with inorganic calcite as a reference.

The slight negative offset of the V.C fraction from the V.F fraction also makes sense, if this V.C fraction preferentially contains more of the typically large *Calcidiscus leptoporous* (~5–10µm) coccoliths, which are offset to lighter values than inorganic calcite (Hermoso, 2014). Even though a small part of the assemblage relative to *Reticulofenestra*, the concentration of *Calcidiscus* species in the large fraction would explain its consistently lighter $\delta^{18}O$ values than the V.F fraction, although both V.F and V.C being substantially (~1 to 1.5‰) heavier than the planktic foraminifera.

The finding of such large and consistent offsets between $\delta^{18}O_{Foram}$ and both $\delta^{18}O_{V.F}$ and $\delta^{18}O_{V.C}$ during the late Miocene indicates the presence of strong isotopic fractionations towards heavier values within *Reticulofenestra* species at this time. Hermoso (2014) proposes that the oxygen isotopic composition of both large and smaller coccolithophores is in modern cultures, and should have been in the past, influenced by the availability of DIC. For instance, the more positive $\delta^{18}O_{V.F}$ values of the heavy group are the result of the efficient use of Carbon Concentrating Mechanisms (CCMs) to cope with low DIC availability. These smaller modern coccolithophore species in the heavy group can concentrate CO_2 internally, which leads to a higher $\delta^{18}O$ value of coccolith calcite. On the other hand, taxa like *Calcidiscus* generally utilize bicarbonate (HCO_3^-) and have more negative $\delta^{18}O$ values. In a nutrient-rich environment, the smaller coccolithophores can dominate because they can quickly take advantage of the available nutrients and out-compete larger species in these conditions. Larger coccolithophores, which rely more on bicarbonate and are less efficient at concentrating CO_2, may struggle to calcify in DIC-depleted conditions. Although the nutrient levels are high, the inability to effectively utilize the available DIC can reduce the abundance of larger coccolithophores while the smaller coccolithophores thrive in a low DIC and high nutrient environment because of their efficient CCM strategies and exhibit more positive $\delta^{18}O$ values (Hermoso, 2014).

The convergence of the large and small coccoliths to similar $\delta^{18}O$ values is a prediction of modern culture studies at high DIC concentrations (Hermoso, 2014). The convergence in values should, however, also approach closer to equilibrium inorganic calcite (~planktic foraminiferal calcite), with the small coccolithophore, isotopically heavy group, becoming lighter in $\delta^{18}O$, and the larger coccolithophore, isotopically lighter group, becoming heavier in $\delta^{18}O$ (Hermoso, 2014). In the IODP site U1482 late Miocene data, the $\delta^{18}O_{V.F}$ and $\delta^{18}O_{V.C}$ values have converged to some degree but remain offset by more than 1 ‰ heavier than planktic foraminiferal $\delta^{18}O$. In assemblages dominated by *Reticulofenestra* species, this would suggest that even in the late Miocene, the rapid growth of these species imparts a heavy $\delta^{18}O$ isotopic signature from the uptake, conversion to bicarbonate and use of CO_2, and maybe a persistent feature of this family through time.

5 Conclusions

In conclusion, this study aimed to determine whether late Miocene coccolith isotopic fractionation was driven by declining CO_2 levels or productivity. Using a novel size separation technique, we have successfully isolated very coarse and very fine coccolith fractions from bulk sediment. Detailed slide scanning and particle size measurements confirmed the effectiveness of this technique. Our findings reveal a long-term size reduction of coccoliths from ~8 Ma ago to the present. We observed a notable offset of $\delta^{13}C_{V.C}$ and $\delta^{13}C_{V.F}$ around 7 – 8 Ma ago. This shift did not correlate with declining CO_2 levels but was more likely associated with the onset of Late Miocene Biogenic Bloom (LMBB), increased tropical productivity, and strengthened biological pump of dissolved inorganic carbon (DIC) from the surface to deep waters.

The $\delta^{18}O$ data showed more similarity between very fine and very coarse fractions, with only a slight offset of fine to coarse. Additionally, both $\delta^{18}O_{V.C}$ and $\delta^{18}O_{V.F}$ are showing consistent offset with $\delta^{18}O_{Foram}$ data. This pattern is observed in more recent periods, similar to modern coccolith and inorganic calcite. This finding implies that the $\delta^{18}O$ vital effect of the heavy group-modern *reticulofenestrids* were also present in the late Miocene, despite the different and larger species of *reticulofenestrids* at that time. Overall, the findings of the study suggests that late

Miocene isotopic fractionation was more influenced by the productivity changes, particularly those associated with LMBB rather than declining CO_2. These findings contribute to our knowledge of the complex interactions between biological processes and climatic factors during the late Miocene. Future research should aim to further investigate the vital effects observed in coccoliths and foraminifera to enhance our interpretation of past oceanic conditions and the factors driving them.

References

Baumann, K. H., Čepek, M., & Kinkel, H. (1999). Coccolithophores as Indicators of Ocean Water Masses, Surface-Water Temperature, and Paleoproductivity — Examples from the South Atlantic. In G. Fischer & G. Wefer (Eds.), *Use of Proxies in Paleoceanography: Examples from the South Atlantic* (pp. 117-144). Springer Berlin Heidelberg. https://doi.org/10.1007/978-3-642-58646-0_4

Berger, W. H., Kroenke, L. W., Mayer, L. A., Backman, J., Janecek, T. R., Krissek, L. A., Leckie, M., Lyle, M., Bassinot, F., Corfield, R., Delaney, M., Hagen, R., Jansen, E., Lange, C., Lind, I. L., Marsters, J., Mosher, D., Musgrave, R., Prentice, M., . . . Wu, G. (1992). The record of Ontong Java Plateau, main results of ODP Leg 130. *Geological Society of America bulletin*, *104*(8).

Bhatti, J. S., Apps, J. A., & Lal, R. (2005). Anthropogenic Changes and the Global Carbon Cycle. In *Climate Change and Managed Ecosystems*. CRC Press.

Billard, C., & Inouye, I. (2004). What is new in coccolithophore biology? In H. R. Thierstein & J. R. Young (Eds.), *Coccolithophores: from molecular processes to global impact* (pp. 1-29). Springer Berlin Heidelberg. https://doi.org/10.1007/978-3-662-06278-4_1

Bolton, C. T., Hernández-Sánchez, M. T., Fuertes, M.-Á., González-Lemos, S., Abrevaya, L., Mendez-Vicente, A., Flores, J.-A., Probert, I., Giosan, L., Johnson, J., & Stoll, H. M. (2016). Decrease in coccolithophore calcification and CO_2 since the middle Miocene. *Nature Communications*, *7*(1), 10284. https://doi.org/10.1038/ncomms10284

Bolton, C. T., & Stoll, H. M. (2013). Late Miocene threshold response of marine algae to carbon dioxide limitation. *Nature*, *500*(7464), 558-562. https://doi.org/10.1038/nature12448

Bowen, M. G., Clift, P. D., Hahn, A., Kulhanek, D. K., Lyle, M., Vincent, S. M., & Zhou, P. (2020). Chemical weathering and erosion responses to changing monsoon climate in the Late Miocene of Southwest Asia. *Geological Magazine*, *157*(6), 939-955. https://doi.org/10.1017/S0016756819000608

Bown, P. R., Gibbs, S. J., Sheward, R. M., O'Dea, S. A., & Higgins, D. (2014). Searching for cells: the potential of fossil coccospheres in coccolithophore research. *Journal of Nannoplankton Research*.

Bown, P. R., Lees, J. A., & Young, J. R. (2004). Calcareous nannoplankton evolution and diversity through time. *Coccolithophores: from molecular processes to global impact*, 481-508.

Cavaleiro, C., Voelker, A. H. L., Stoll, H., Baumann, K.-H., & Kucera, M. (2020). Coccolithophore productivity at the western Iberian Margin during the Middle Pleistocene (310–455 ka) – evidence from coccolith Sr⁄Ca data. *Climate of the Past*, *16*(6), 2017-2037. https://doi.org/10.5194/cp-16-2017-2020

Cortese, G., Gersonde, R., Hillenbrand, C.-D., & Kuhn, G. (2004). Opal sedimentation shifts in the World Ocean over the last 15 Myr. *Earth and Planetary Science Letters*, *224*(3), 509-527. https://doi.org/https://doi.org/10.1016/j.epsl.2004.05.035

Curry, W., Shackleton, N., Richter, C., Backman, J., Bassinot, F., Bickert, T., et al. (1995). Leg synthesis. Proceedings Ocean Drilling Program, . *Ocean Drilling Program.*

de Vargas, C., Aubry, M.-P., Probert, I., & Young, J. (2007). Origin and Evolution of Coccolithophores: From Coastal Hunters to Oceanic Farmers. *Evolution of primary producers in the Sea*.

Dickens, G. R., & Owen, R. M. (1999). The Latest Miocene–Early Pliocene biogenic bloom: a revised Indian Ocean perspective. *Marine Geology*, *161*(1), 75-91. https://doi.org/10.1016/S0025-3227(99)00057-2

Diester-Haass, L., Billups, K., & Emeis, K. C. (2005). In search of the late Miocene–early Pliocene "biogenic bloom" in the Atlantic Ocean (Ocean Drilling Program Sites 982, 925, and 1088). *PALEOCEANOGRAPHY*, *20*(4), PA4001-n/a. https://doi.org/10.1029/2005PA001139

Ding, L., Spicer, R., Yang, J., Xu, Q., Cai, F., Li, S., Lai, Q., Wang, H., Spicer, T., & Yue, Y. (2017). Quantifying the rise of the Himalaya orogen and implications for the South Asian monsoon. *Geology*, *45*(3), 215-218.

Drury, A. J., Liebrand, D., Westerhold, T., Beddow, H. M., Hodell, D. A., Rohlfs, N., Wilkens, R. H., Lyle, M., Bell, D. B., & Kroon, D. (2021). Climate, cryosphere and carbon cycle controls on Southeast Atlantic orbital-scale carbonate deposition since the Oligocene (30–0 Ma). *Climate of the Past*, *17*(5), 2091-2117.

Dudley, W. C., Blackwelder, P., Brand, L., & Duplessy, J.-C. (1986). Stable isotopic composition of coccoliths. *Marine Micropaleontology*, *10*(1), 1-8. https://doi.org/10.1016/0377-8398(86)90021-6

Dunkley Jones, T., Bown, P. R., Pearson, P. N., Wade, B. S., Coxall, H. K., & Lear, C. H. (2008). Major shifts in calcareous phytoplankton assemblages through the Eocene-Oligocene transition of Tanzania and their implications for low-latitude primary production. *PALEOCEANOGRAPHY*, *23*(4). https://doi.org/10.1029/2008PA001640

Ezard, T. H. G., Aze, T., Pearson, P. N., & Purvis, A. (2011). Interplay Between Changing Climate and Species' Ecology Drives Macroevolutionary Dynamics. *Science*, *332*(6027), 349-351. https://doi.org/10.1126/science.1203060

Falkowski, P. G., Katz, M. E., Knoll, A. H., Quigg, A., Raven, J. A., Schofield, O., & Taylor, F. J. R. (2004). evolution of modern eukaryotic phytoplankton. *Science*, *305*(5682), 354-360. https://doi.org/10.1126/science.1095964

Farrell, J. W., Raffi, I., Janecek, T. R., Murray, D. W., Levitan, M., Dadey, K. A., Emeis, K.-C., Lyle, M., Flores, J.-A., & Hovan11, S. (1995). 35. Late Neogene sedimentation patterns in the eastern equatorial Pacific Ocean. In *Proceedings of the ocean drilling program, scientific results* (Vol. 138, pp. 2419-2426). Ocean Drilling Program.

Feely, R. A., Takahashi, T., & Wanninkhof, R. (2005). Sources and sinks of carbon dioxide in the surface oceans. *Geochimica et Cosmochimica Acta*, *69*(10), A723.

Flores, J. A., & Sierro, F. J. (1997). Revised technique for calculation of calcareous nannofossil accumulation rates. *Micropaleontology*, *43*(3), 321-324. https://doi.org/10.2307/1485832

Gard, G. (1987). Observation of a Dimorphic Coccosphere. *Abhandlungen der Geologischen Bundesanstalt.*, *39*, 85-87.

Gastaldello, M. E., Agnini, C., Westerhold, T., Drury, A. J., & Alegret, L. (2024). A benthic foraminifera perspective of the Late Miocene-Early Pliocene Biogenic Bloom at ODP Site 1085 (Southeast Atlantic Ocean). *Palaeogeography, palaeoclimatology, palaeoecology*, *638*, 112040. https://doi.org/https://doi.org/10.1016/j.palaeo.2024.112040

Grant, K. M., & Dickens, G. R. (2002). Coupled productivity and carbon isotope records in the southwest Pacific Ocean during the late Miocene–early Pliocene biogenic bloom. *Palaeogeography, palaeoclimatology, palaeoecology*, *187*(1-2), 61-82.

Hannisdal, B., Henderiks, J., & Liow, L. H. (2012). Long-term evolutionary and ecological responses of calcifying phytoplankton to changes in atmospheric CO_2. *Glob Change Biol*, *18*(12), 3504-3516. https://doi.org/10.1111/gcb.12007

Hanson, E. M. (2023). *Novel Approaches to High-Resolution studies of Calcareous Nannoplankton* [PhD, University of Birmingham.]. https://etheses.bham.ac.uk/id/eprint/13844/

Haq, B. U. (1980). Biogeographic History of Miocene Calcareous Nannoplankton and Paleoceanography of the Atlantic Ocean. *Micropaleontology*, *26*(4), 414-443. https://doi.org/10.2307/1485353

Haunost, M., Riebesell, U., & Bach, L. T. (2020). The Calcium Carbonate Shell of *Emiliania huxleyi* Provides Limited Protection Against Viral Infection. *Frontiers in Marine Science*, *7*. https://doi.org/https://doi.org/10.3389/fmars.2020.530757

Henderiks, J., Bartol, M., Pige, N., Karatsolis, B. T., & Lougheed, B. C. (2020). Shifts in Phytoplankton Composition and Stepwise Climate Change During the Middle Miocene. *Paleoceanography and Paleoclimatology*, *35*(8). https://doi.org/10.1029/2020PA003915

Herbert, T. D., Lawrence, K. T., Tzanova, A., Peterson, L. C., Caballero-Gill, R., & Kelly, C. S. (2016). Late Miocene global cooling and the rise of modern ecosystems. *Nature geoscience*, *9*(11), 843-847. https://doi.org/10.1038/ngeo2813

Hermoso, M. (2014). Coccolith-Derived Isotopic Proxies in Palaeoceanography: Where Geologists Need Biologists. *Cryptogamie, Algologie*, *35*(4), 323-351, 329. https://doi.org/10.7872/crya.v35.iss4.2014.323

Hermoso, M., Candelier, Y., Browning, T. J., & Minoletti, F. (2015). Environmental control of the isotopic composition of subfossil coccolith calcite: Are laboratory culture data transferable to the natural environment? *GeoResJ (Amsterdam)*, *7*, 35-42. https://doi.org/10.1016/j.grj.2015.05.002

Hermoyian, C. S., & Owen, R. M. (2001). Late Miocene-early Pliocene biogenic bloom: Evidence from low-productivity regions of the Indian and Atlantic Oceans. *PALEOCEANOGRAPHY*, *16*(1), 95-100. https://doi.org/10.1029/2000PA000501

Hönisch, B., Royer, D. L., Breecker, D. O., Polissar, P. J., Bowen, G. J., Henehan, M. J., Cui, Y., Steinthorsdottir, M., McElwain, J. C., Kohn, M. J., Pearson, A., Phelps, S. R., Uno, K. T., Ridgwell, A., Anagnostou, E., Austermann, J., Badger, M. P. S., Barclay, R. S., Bijl, P. K., . . . Zhang, L. (2023). Toward a Cenozoic history of atmospheric CO_2. *Science*, *382*(6675). https://doi.org/10.1126/science.adi5177

Honjo, S. (1976). Coccoliths: Production, transportation and sedimentation. *Marine Micropaleontology*, *1*, 65-79. https://doi.org/https://doi.org/10.1016/0377-8398(76)90005-0

Hovan, S. A. (1995). 28. Late Cenozoic atmospheric circulation intensity and climatic history recorded by Eolian deposition in the Eastern Equatorial Pacific Ocean, Leg 138. *Proceedings of the Ocean Drilling Program, Scientific Results. Proceedings of the Ocean Drilling Program, Scientific Results*, 615-625.

Hutchinson, G. E. (1967). *A treatise on limnology, introduction to lake biology and the limnoplankton* (Vol. 2). Wiley.

Isenberg, H. D., Lavine, L. S., Moss, M. L., Kupferstein, D., & Lear, P. E. (1963). Calcification in a marine coccolithophorid. *Annals of the New York Academy of Sciences*, *109*(1), 49-64.

Jian, Q. (2003). Trends and Advances of the Global Change Studies on Carbon Cycle. *Advance in Earth Sciences*.

Jones, A. P. (2021). *Macroevolutionary dynamics and diversity of coccolithophores across long-term cooling periods of the Cenozoic* [Phd, University of Birmingham]. https://etheses.bham.ac.uk//id/eprint/12111/

Jordan, R. W. (2009). Coccolithophores. In M. Schaechter (Ed.), *Encyclopedia of Microbiology (Third Edition)* (pp. 593-605). Academic Press. https://doi.org/https://doi.org/10.1016/B978-012373944-5.00249-2

Karatsolis, B. T., Lougheed, B. C., De Vleeschouwer, D., & Henderiks, J. (2022). Abrupt conclusion of the late Miocene-early Pliocene biogenic bloom at 4.6-4.4 Ma. *Nat Commun*, *13*(1), 353-353. https://doi.org/10.1038/s41467-021-27784-6

Krijgsman, W., Capella, W., Simon, D., Hilgen, F. J., Kouwenhoven, T. J., Meijer, P. T., Sierro, F. J., Tulbure, M. A., van den Berg, B. C. J., van der Schee, M., & Flecker, R. (2018). The Gibraltar Corridor: Watergate of the Messinian Salinity Crisis. *Marine Geology*, *403*, 238-246. https://doi.org/https://doi.org/10.1016/j.margeo.2018.06.008

Lagabrielle, Y., Goddéris, Y., Donnadieu, Y., Malavieille, J., & Suarez, M. (2009). The tectonic history of Drake Passage and its possible impacts on global climate. *Earth and Planetary Science Letters*, *279*(3), 197-211. https://doi.org/10.1016/j.epsl.2008.12.037

Lewitus, E., Bittner, L., Malviya, S., Bowler, C., & Morlon, H. (2018). Clade-specific diversification dynamics of marine diatoms since the Jurassic. *Nature Ecology & Evolution*, *2*(11), 1715-1723. https://doi.org/10.1038/s41559-018-0691-3

Lyle, M., & Baldauf, J. (2015). Biogenic sediment regimes in the Neogene equatorial Pacific, IODP Site U1338: Burial, production, and diatom community. *Palaeogeography, palaeoclimatology, palaeoecology*, *433*, 106-128. https://doi.org/10.1016/j.palaeo.2015.04.001

Lyle, M., Drury, A. J., Tian, J., Wilkens, R., & Westerhold, T. (2019). Late Miocene to Holocene high-resolution eastern equatorial Pacific carbonate records: stratigraphy linked by dissolution and paleoproductivity. *Climate of the Past*, *15*(5), 1715-1739.

Margalef, R. (1978). Phytoplankton communities in upwelling areas. The example of NW Africa. *Oecologia aquatica*, *3*(3), 97-132.

Marino, M., Maiorano, P., Lirer, F., & Pelosi, N. (2009). Response of calcareous nannofossil assemblages to paleoenvironmental changes through the mid-Pleistocene revolution at Site 1090 (Southern Ocean). *Palaeogeography, palaeoclimatology, palaeoecology*, *280*(3-4), 333-349.

Milliman, J. D. (1993). Production and accumulation of calcium carbonate in the ocean: Budget of a nonsteady state. *Global Biogeochemical Cycles*, *7*(4), 927-957. https://doi.org/10.1029/93gb02524

Minoletti, F., Hermoso, M., & Gressier, V. (2009). Separation of sedimentary micron-sized particles for palaeoceanography and calcareous nannoplankton biogeochemistry. *Nat Protoc*, *4*(1), 14-24. https://doi.org/10.1038/nprot.2008.200

Molnar, P. (2005). Mio-Pliocene growth of the Tibetan Plateau and evolution of East Asian climate. *Palaeontologia Electronica*, *8*(1), 1-23.

Müller, M. N., Lebrato, M., Riebesell, U., Barcelos E Ramos, J., Schulz, K. G., Blanco-Ameijeiras, S., Sett, S., Eisenhauer, A., & Stoll, H. M. (2014). Influence of temperature and CO_2 on the strontium and magnesium composition of coccolithophore calcite. *Biogeosciences*, *11*(4), 1065-1075. https://doi.org/10.5194/bg-11-1065-2014

Munk, W. H., & Riley, G. A. (1952). Absorption of nutrients by aquatic plants. *Journal of Marine Research*, *11*(2). https://escholar.library.yale.edu/journal_of_marine_research/772

Olson, D. B., Hitchcock, G. L., Fine, R. A., & Warren, B. A. (1993). Maintenance of the low-oxygen layer in the central Arabian Sea. *Deep Sea Research Part II: Topical Studies in Oceanography*, *40*(3), 673-685.

Orr, J. C., Fabry, V. J., Aumont, O., Bopp, L., Doney, S. C., Feely, R. A., Gnanadesikan, A., Gruber, N., Ishida, A., Joos, F., Key, R. M., Lindsay, K., Maier-Reimer, E., Matear, R., Monfray, P., Mouchet, A., Najjar, R. G., Plattner, G.-K., Rodgers, K. B., . . . Yool, A. (2005). Anthropogenic ocean acidification over the twenty-first century and its impact on calcifying organisms. *Nature*, *437*(7059), 681-686. https://doi.org/10.1038/nature04095

Paull, C. K., & Thierstein, H. R. (1987). Stable isotopic fractionation among particles in Quaternary coccolith-sized deep-sea sediments. *PALEOCEANOGRAPHY*, *2*(4), 423-429. https://doi.org/10.1029/PA002i004p00423

Pillot, Q., Suchéras-Marx, B., Sarr, A. C., Bolton, C. T., & Donnadieu, Y. (2023). A Global Reassessment of the Spatial and Temporal Expression of the Late Miocene Biogenic Bloom. *Paleoceanography and Paleoclimatology*, *38*(3). https://doi.org/10.1029/2022pa004564

Pisias, N. G., Mayer, L. A., Janecek, T. R., Baldauf, J. G., Bloomer, S. F., Dadey, K. A., Emeis, K.-C., Farrell, J., Flores, J.-A., & Galimov, E. M. (1995). Proceedings of the Ocean Drilling Program; scientific results; eastern Equatorial Pacific, covering Leg 138 of the cruises of the drilling vessel JOIDES Resolution, Balboa, Panama, to San Diego, California, Sites 844-854, 1 May-4 July 1991. Proceedings of the Ocean Drilling Program. Scientific results,

Raven, J. A., & Falkowski, P. G. (1999). Oceanic sinks for atmospheric CO_2. *Plant Cell and Environment*, *22*, 741-755.

Rea, D. K. (1994). The paleoclimatic record provided by eolian deposition in the deep sea: The geologic history of wind. *Reviews of Geophysics*, *32*(2), 159-195.

Rea, D. K., Snoeckx, H., & Joseph, L. H. (1998). Late Cenozoic eolian deposition in the North Pacific: Asian drying, Tibetan uplift, and cooling of the northern hemisphere. *PALEOCEANOGRAPHY*, *13*(3), 215-224.

Renaudie, J. (2016). Quantifying the Cenozoic marine diatom deposition history: links to the C and Si cycles. *Biogeosciences*, *13*(21), 6003-6014. https://doi.org/10.5194/bg-13-6003-2016

Rock, J., Taylor, L., & Allen, R. (2018). Coccolithophore Relief: An Art and Science Interrogation of Ocean Acidification. *Junctures-the Journal for Thematic Dialogue*, 86.

Rögl, F. (1999). Mediterranean and Paratethys: facts and hypotheses of an Oligocene to Miocene paleogeography: short overview. *Geologica carpathica: international geological journal*, *50*(4), 339.

Rosenthal, Y., Holbourn, A. E., Kulhanek, D. K., Aiello, I. W., Babila, T. L., Bayon, G., & Zhang, Y. G. (2018). Expedition 363 summary. In A. E. H. Y. Rosenthal, D. K. Kulhanek & S. the Expedition (Eds.), *Proceedings of the International Ocean Discovery Program* (Vol. 363). https://doi.org/https://doi.org/10.14379/iodp.proc.363.103.2018

Rost, B., & Riebesell, U. (2004). Coccolithophores and the biological pump: responses to environmental changes. In H. R. Thierstein & J. R. Young (Eds.), *Coccolithophores: from molecular processes to global impact* (pp. 99-125). Springer Berlin Heidelberg. https://doi.org/10.1007/978-3-662-06278-4_5

Roveri, M., Flecker, R., Krijgsman, W., Lofi, J., Lugli, S., Manzi, V., Sierro, F. J., Bertini, A., Camerlenghi, A., De Lange, G., Govers, R., Hilgen, F. J., Hübscher, C., Meijer, P. T., & Stoica, M. (2014). The Messinian Salinity Crisis: Past and future of a great challenge for marine sciences. *Marine Geology*, *352*, 25-58. https://doi.org/10.1016/j.margeo.2014.02.002

Rowson, J. D., Leadbeater, B. S. C., & Green, J. C. (1986). Calcium carbonate deposition in the motile (Crystallolithus) phase of *Coccolithus pelagicus* (*Prymnesiophyceae*). *British Phycological Journal*, *21*(4), 359-370. https://doi.org/10.1080/00071618600650431

Sabine, C. L., Feely, R. A., Gruber, N., Key, R. M., Lee, K., Bullister, J. L., Wanninkhof, R., Wong, C. S., Douglas, W. R. W., Tilbrook, B., Millero, F. J., Peng, T.-H., Kozyr, A., Ono, T., & Rios, A. F. (2004). The Oceanic Sink for Anthropogenic CO_2. *Science*, *305*(5682), 367-371. https://doi.org/10.1126/science.1097403

Schindelin, J., Arganda-Carreras, I., Frise, E., Kaynig, V., Longair, M., Pietzsch, T., Preibisch, S., Rueden, C., Saalfeld, S., Schmid, B., Tinevez, J.-Y., White, D. J., Hartenstein, V., Eliceiri, K., Tomancak, P., & Cardona, A. (2012). Fiji: an open-source platform for biological-image analysis. *Nat Methods*, *9*(7), 676-682. https://doi.org/10.1038/nmeth.2019

Schmidt, D. N., Thierstein, H. R., & Bollmann, J. (2004). The evolutionary history of size variation of planktic foraminiferal assemblages in the Cenozoic. *Palaeogeography, palaeoclimatology, palaeoecology*, *212*(1), 159-180. https://doi.org/https://doi.org/10.1016/j.palaeo.2004.06.002

Schneider, B., & Schmittner, A. (2006). Simulating the impact of the Panamanian seaway closure on ocean circulation, marine productivity and nutrient cycling. *Earth and Planetary Science Letters*, *246*(3), 367-380. https://doi.org/https://doi.org/10.1016/j.epsl.2006.04.028

Sheward, R. M., Poulton, A. J., Gibbs, S. J., Daniels, C. J., & Bown, P. R. (2017). Physiology regulates the relationship between coccosphere geometry and growth phase in coccolithophores. *Biogeosciences*, *14*(6), 1493-1509. https://doi.org/10.5194/bg-14-1493-2017

Si, W., & Rosenthal, Y. (2019). Reduced continental weathering and marine calcification linked to late Neogene decline in atmospheric CO_2. *Nature geoscience*, *12*(10), 833-838. https://doi.org/10.1038/s41561-019-0450-3

Silva, P. C., Throndsen, J., & Eikrem, W. (2007). Revisiting the nomenclature of haptophytes. *Phycologia (Oxford)*, *46*(4), 471-475. https://doi.org/10.2216/07-22.1

Singh, R. K., Gupta, A. K., & Das, M. (2012). Paleoceanographic significance of deep-sea benthic foraminiferal species diversity at southeastern Indian Ocean Hole 752A during the Neogene. *Palaeogeography, palaeoclimatology, palaeoecology*, *361-362*, 94-103. https://doi.org/https://doi.org/10.1016/j.palaeo.2012.08.008

Steinthorsdottir, M., Coxall, H. K., De Boer, A. M., Huber, M., Barbolini, N., Bradshaw, C. D., Burls, N. J., Feakins, S. J., Gasson, E., Henderiks, J., Holbourn, A. E., Kiel, S., Kohn, M. J., Knorr, G., Kürschner, W. M., Lear, C. H., Liebrand, D., Lunt, D. J., Mörs, T., . . . Strömberg, C. A. E. (2021a). The Miocene: The Future of the Past. *Paleoceanography and Paleoclimatology*, *36*(4). https://doi.org/10.1029/2020pa004037

Steinthorsdottir, M., Coxall, H. K., de Boer, A. M., Huber, M., Barbolini, N., Bradshaw, C. D., Burls, N. J., Feakins, S. J., Gasson, E., Henderiks, J., Holbourn, A. E., Kiel, S., Kohn, M. J., Knorr, G., Kürschner, W. M., Lear, C. H., Liebrand, D., Lunt, D. J., Mörs, T., . . . Strömberg, C. A. E. (2021b). The Miocene: The Future of the Past. *Paleoceanography and Paleoclimatology*, *36*(4), n/a. https://doi.org/10.1029/2020PA004037

Stoll, H. M., & Ziveri, P. (2002). Separation of monospecific and restricted coccolith assemblages from sediments using differential settling velocity. *Marine Micropaleontology*, *46*(1), 209-221. https://doi.org/10.1016/S0377-8398(02)00040-3

Suchéras-Marx, B., & Henderiks, J. (2014). Downsizing the pelagic carbonate factory: Impacts of calcareous nannoplankton evolution on carbonate burial over the past 17 million years. *Global and planetary change*, *123*, 97-109. https://doi.org/10.1016/j.gloplacha.2014.10.015

Suchéras-Marx, B., Viseur, S., Walker, C. E., Beaufort, L., Probert, I., & Bolton, C. (2022). Coccolith size rules – What controls the size of coccoliths during coccolithogenesis? *Marine Micropaleontology*, *170*, 102080. https://doi.org/https://doi.org/10.1016/j.marmicro.2021.102080

Suto, I. (2006). The explosive diversification of the diatom genus Chaetoceros across the Eocene/Oligocene and Oligocene/Miocene boundaries in the Norwegian Sea. *Marine Micropaleontology*, *58*(4), 259-269. https://doi.org/https://doi.org/10.1016/j.marmicro.2005.11.004

Tauxe, L., & Feakins, S. J. (2020). A Reassessment of the Chronostratigraphy of Late Miocene C_3 -C_4 Transitions. *Paleoceanography and Paleoclimatology*, *35*(7). https://doi.org/10.1029/2020PA003857

Taylor, A. R., Brownlee, C., & Wheeler, G. L. (2017). Coccolithophore Cell Biology: Chalking Up Progress. *Annual review of marine science*, *9*, 283-310.

Tréguer, P., Bowler, C., Moriceau, B., Dutkiewicz, S., Gehlen, M., Aumont, O., Bittner, L., Dugdale, R., Finkel, Z., Iudicone, D., Jahn, O., Guidi, L., Lasbleiz, M., Leblanc, K., Levy, M., & Pondaven, P. (2018). Influence of diatom diversity on the ocean biological carbon pump. *Nature geoscience*, *11*(1), 27-37. https://doi.org/10.1038/s41561-017-0028-x

Tyrrell, T., & Merico, A. (2004). *Emiliania huxleyi*: bloom observations and the conditions that induce them. In H. R. Thierstein & J. R. Young (Eds.), *Coccolithophores: from molecular processes to global impact* (pp. 75-97). Springer Berlin Heidelberg. https://doi.org/10.1007/978-3-662-06278-4_4

Wang, C., Dai, J., Zhao, X., Li, Y., Graham, S. A., He, D., Ran, B., & Meng, J. (2014). Outward-growth of the Tibetan Plateau during the Cenozoic: A review. *Tectonophysics*, *621*, 1-43. https://doi.org/https://doi.org/10.1016/j.tecto.2014.01.036

Wang, K. X., Yao, M. Y., & Xu, L. J. (2001). A focus topic of global change study: carbon cycle. *Journal of Zhejiang University (Agriculture and Life Sciences)*, *27*(5), 473-478.

Westbroek, P., Brown, C. W., van Bleijswijk, J., Brownlee, C., Brummer, G. J., Conte, M., Egge, J., Fernández, E., Jordan, R., & Knappertsbusch, M. (1993). A model system approach to biological climate forcing. The example of *Emiliania huxleyi*. *Global and planetary change*, *8*(1-2), 27-46.

Westerhold, T., Marwan, N., Drury, A. J., Liebrand, D., Agnini, C., Anagnostou, E., Barnet, J. S. K., Bohaty, S. M., De Vleeschouwer, D., Florindo, F., Frederichs, T., Hodell, D. A., Holbourn, A. E., Kroon, D., Lauretano, V., Littler, K., Lourens, L. J., Lyle, M., Pälike, H., . . . Zachos, J. C. (2020). An astronomically dated record of Earth's climate and its predictability over the last 66 million years. *Science*, *369*(6509), 1383-1387. https://doi.org/doi:10.1126/science.aba6853

Winter, W. G. S. (1994). *Coccolithophores* (2009/05/11 ed., Vol. 75). Cambridge University Press. https://doi.org/10.1017/S0025315400015496

Wu, Y., Hain, M. P., Humphreys, M. P., Hartman, S., & Tyrrell, T. (2019). What drives the latitudinal gradient in open-ocean surface dissolved inorganic carbon concentration? *Biogeosciences*, *16*(13), 2661-2681. https://doi.org/10.5194/bg-16-2661-2019

Wyrtki, K. (1971). Oceanographic Atlas of the International Indian Ocean Expedition. *National Science Foundation*, 351.

Young, J. R. (1997). Guidelines for coccolith and calcareous nanofossil terminology. *Palaeontology*, *40*, 875-912.

Young, J. R., Didymus, J. M., Brown, P. R., Prins, B., & Mann, S. (1992). Crystal assembly and phylogenetic evolution in heterococcoliths. *Nature*, *356*(6369), 516-518.

Young, J. R., & Henriksen, K. (2003). Biomineralization Within Vesicles: The Calcite of Coccoliths. *Reviews in Mineralogy and Geochemistry*, *54*(1), 189-215. https://doi.org/10.2113/0540189

Zhang, H., Liu, C., Mejía, L. M., & Stoll, H. (2021). Technical note: Accelerate coccolith size separation via repeated centrifugation. *Biogeosciences*, *18*(5), 1909-1916. https://doi.org/10.5194/bg-18-1909-2021

Zhang, L., Chen, M., Xiang, R., Zhang, L., & Lu, J. (2009). Productivity and continental denudation history from the South China Sea since the late Miocene. *Marine Micropaleontology*, *72*(1), 76-85. https://doi.org/10.1016/j.marmicro.2009.03.006

Appendix A: Good Plots

All the charts below are Cumulative percentage versus particle size (µm²) distributions for different sediment samples. Blue circles represent the coarse fraction (V.C), and red circles represent the fine fraction (V.F). The x-axis shows area of particle size in (µm²), and the y-axis represents cumulative percentage, highlighting the variation in particle size distribution across different samples.

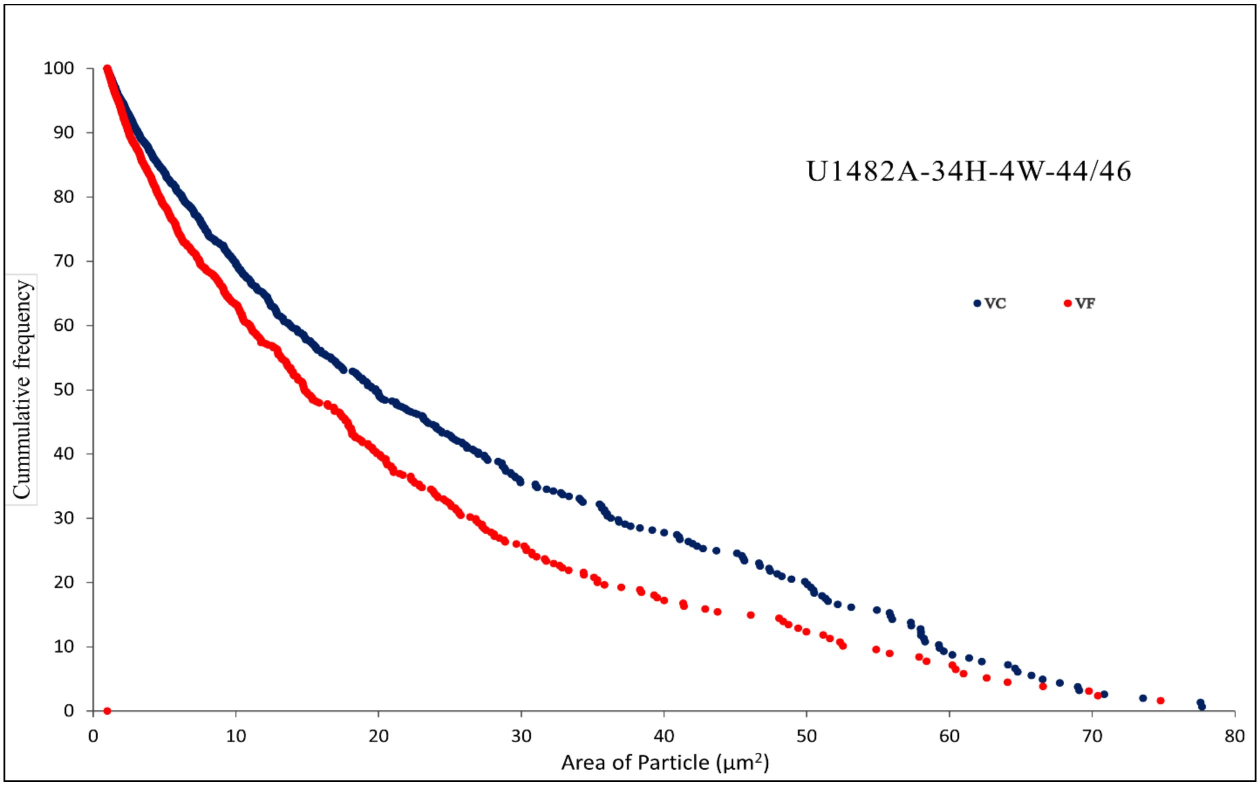

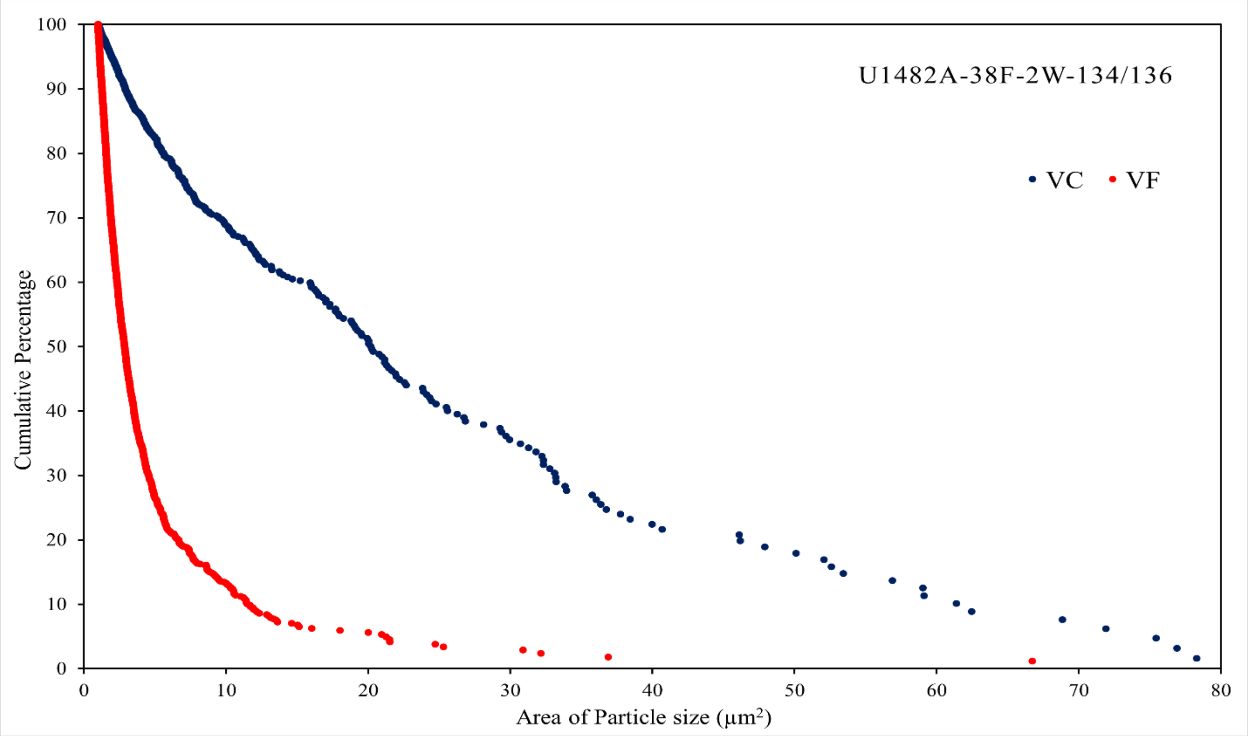
U1482A-38F-2W-134/136
VC
VF
Cumulative Percentage
Area of Particle size (μm²)
0
10
20
30
40
50
60
70
80
90
100
0
10
20
30
40
50
60
70
80

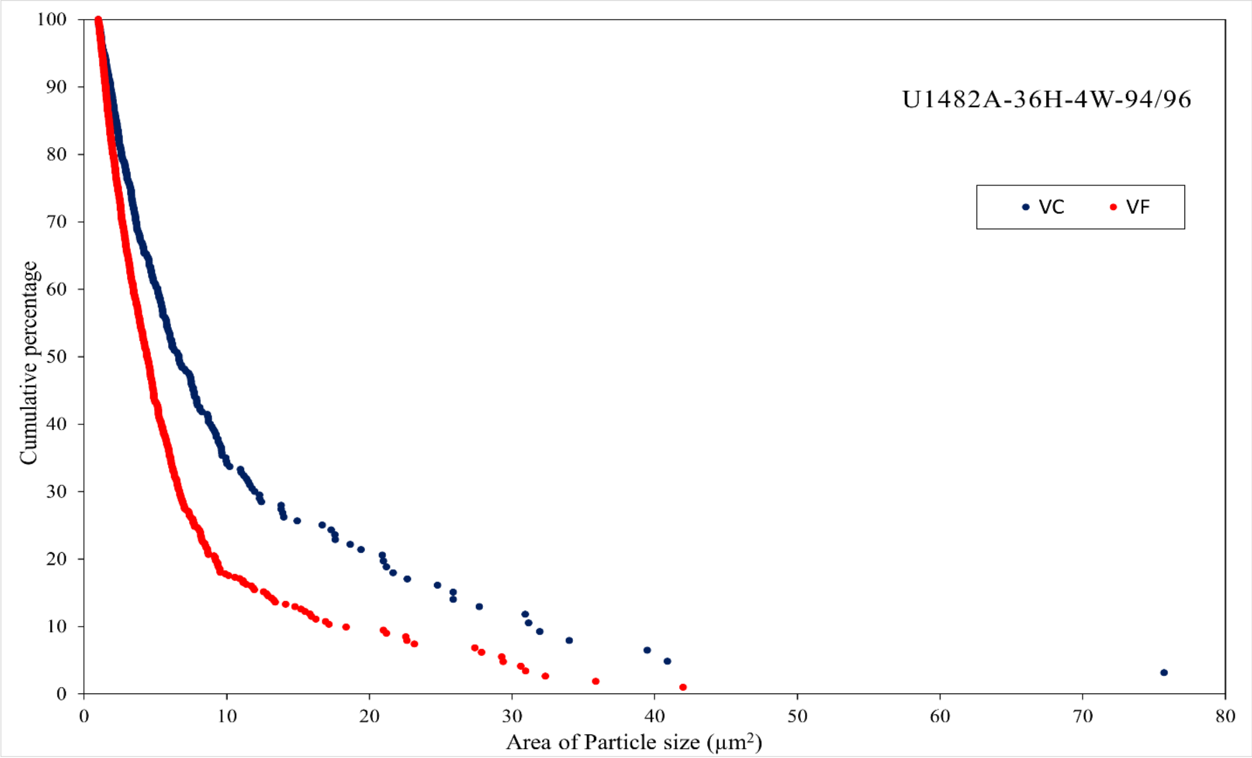
U1482A-36H-4W-94/96
VC
VF
Cumulative percentage
Area of Particle size (μm²)
0
10
20
30
40
50
60
70
80
90
100
0
10
20
30
40
50
60
70
80

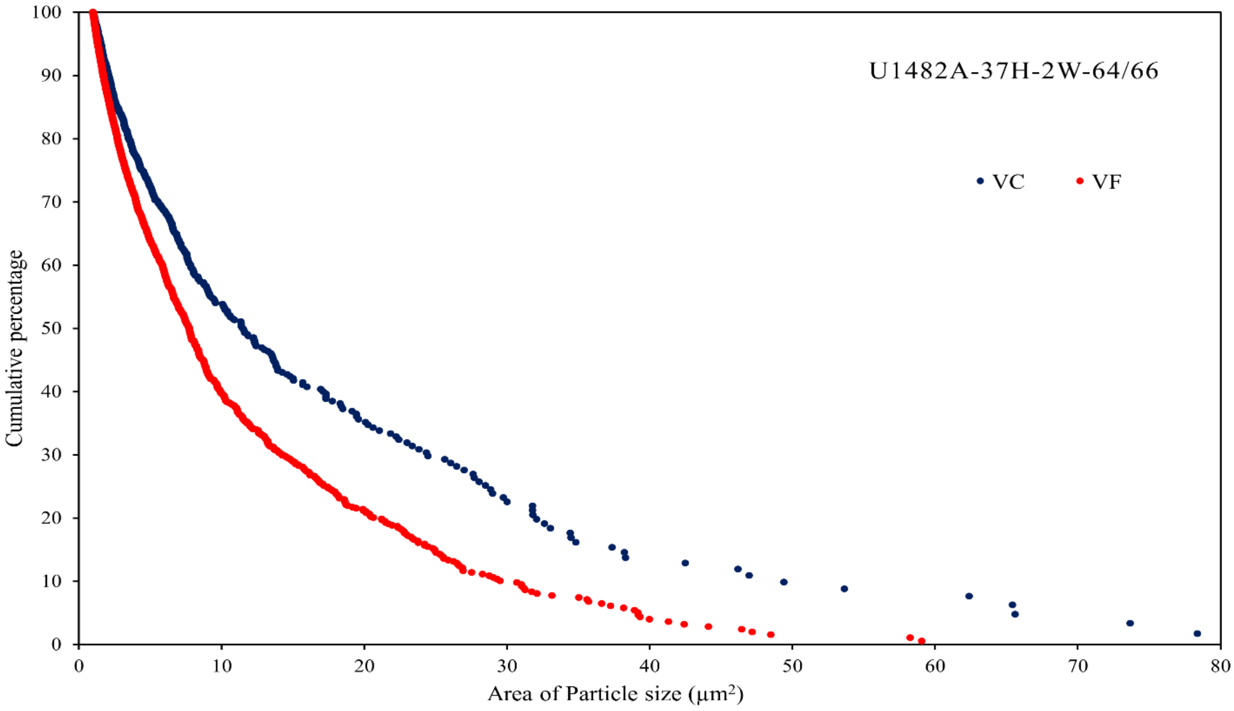
U1482A-37H-2W-64/66
• VC
• VF
Cumulative percentage
Area of Particle size (µm²)
0
10
20
30
40
50
60
70
80
90
100
0
10
20
30
40
50
60
70
80

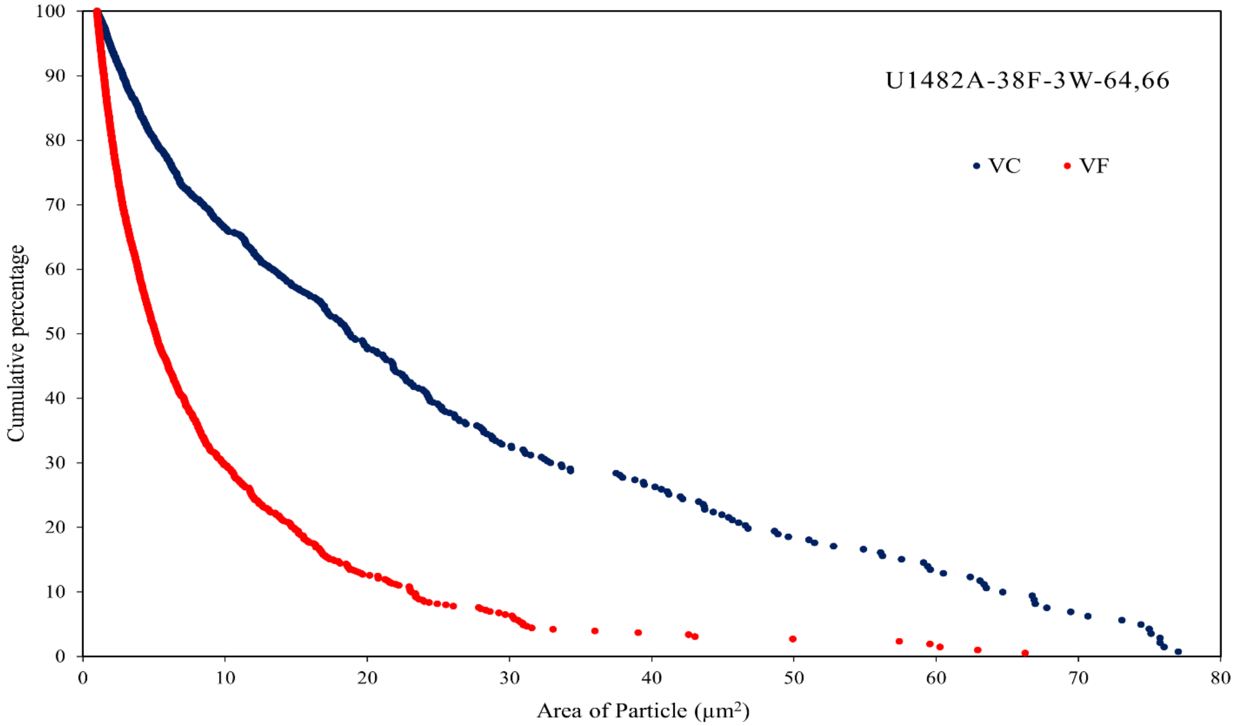
U1482A-38F-3W-64,66
• VC
• VF
Cumulative percentage
Area of Particle (µm²)
0
10
20
30
40
50
60
70
80
90
100
0
10
20
30
40
50
60
70
80

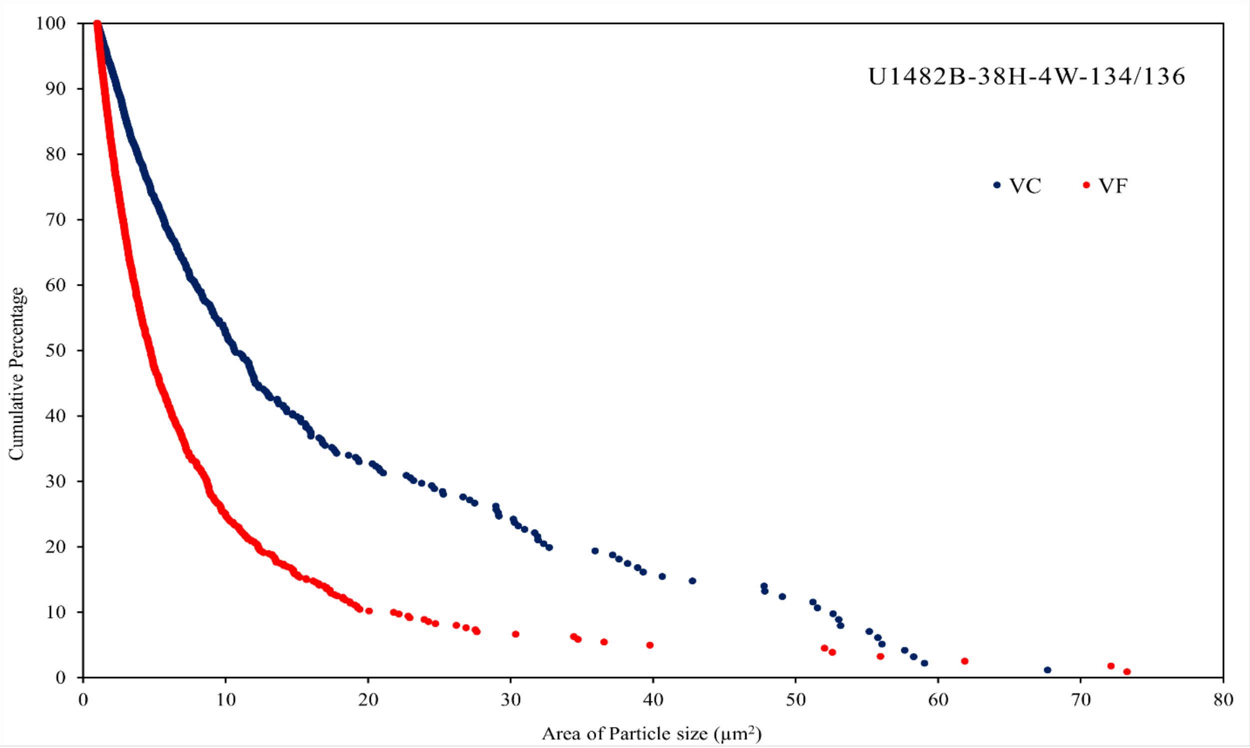
U1482B-38H-4W-134/136
VC
VF
Cumulative Percentage
Area of Particle size (μm²)
0
10
20
30
40
50
60
70
80
90
100
0
10
20
30
40
50
60
70
80

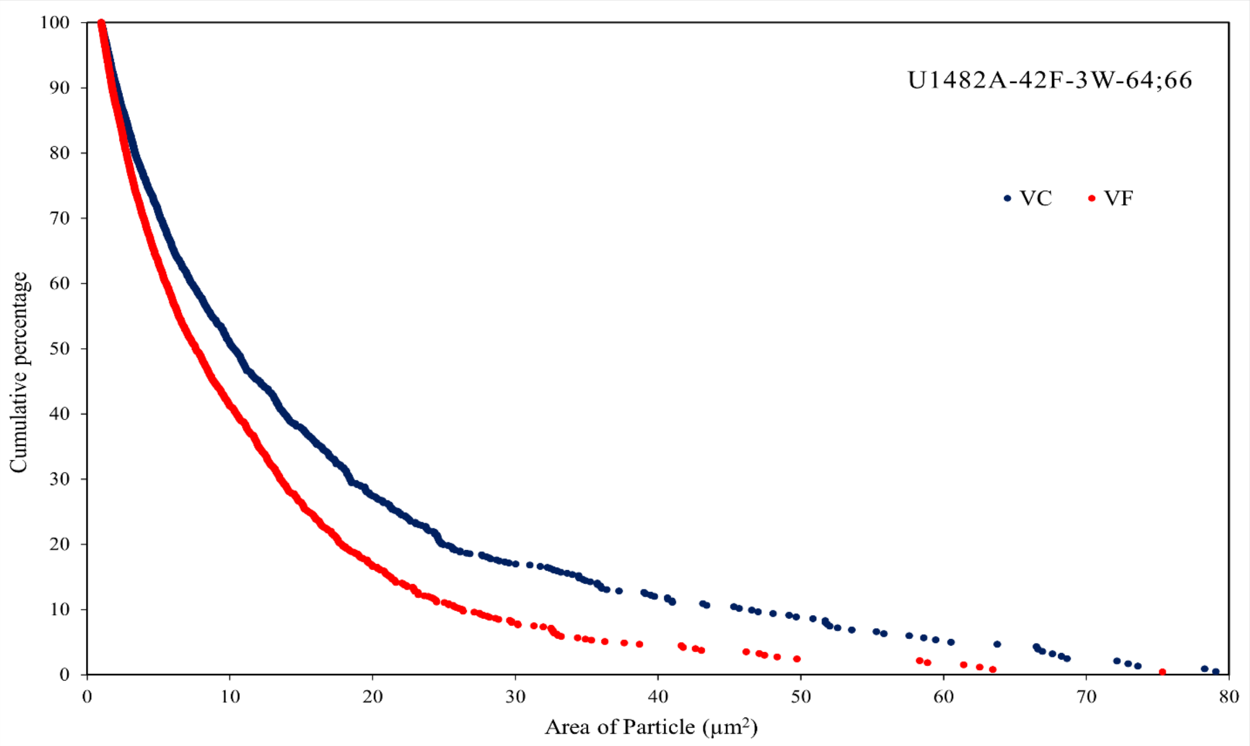
U1482A-42F-3W-64;66
VC
VF
Cumulative percentage
Area of Particle (μm²)
0
10
20
30
40
50
60
70
80
90
100
0
10
20
30
40
50
60
70
80

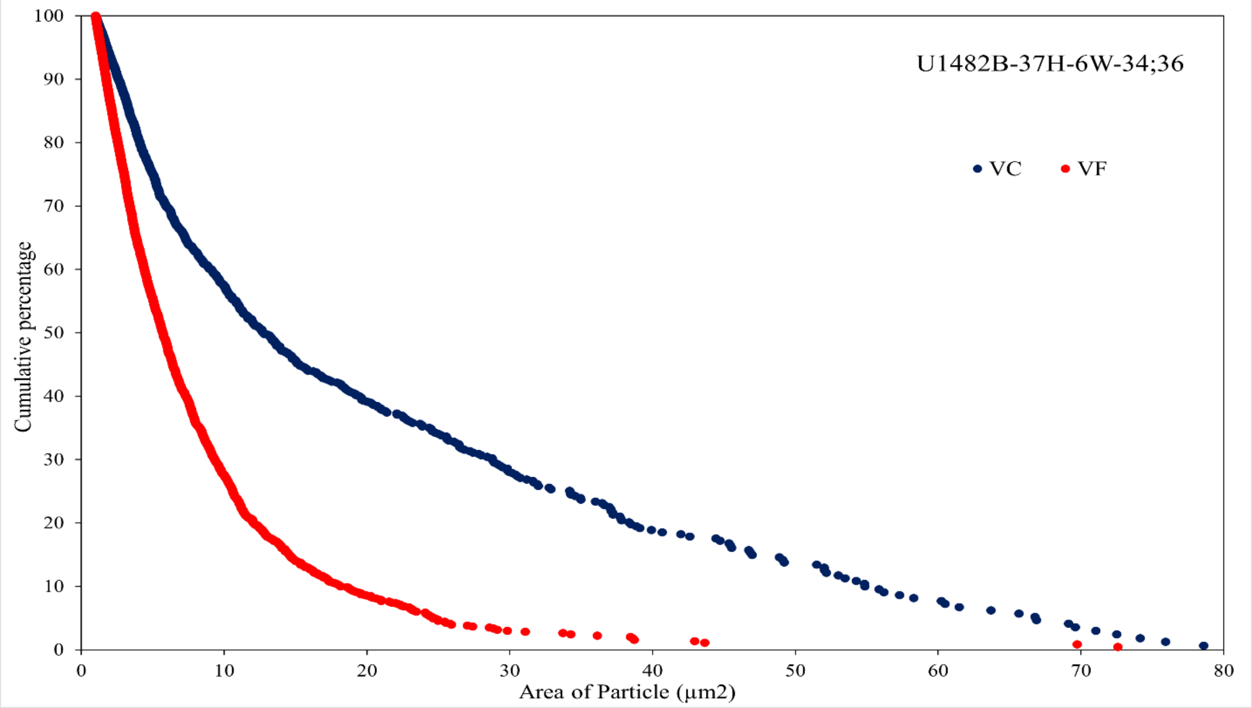

U1482B-37H-6W-34;36
● VC
● VF
Cumulative percentage
100
90
80
70
60
50
40
30
20
10
0
0
10
20
30
40
50
60
70
80
Area of Particle (µm2)

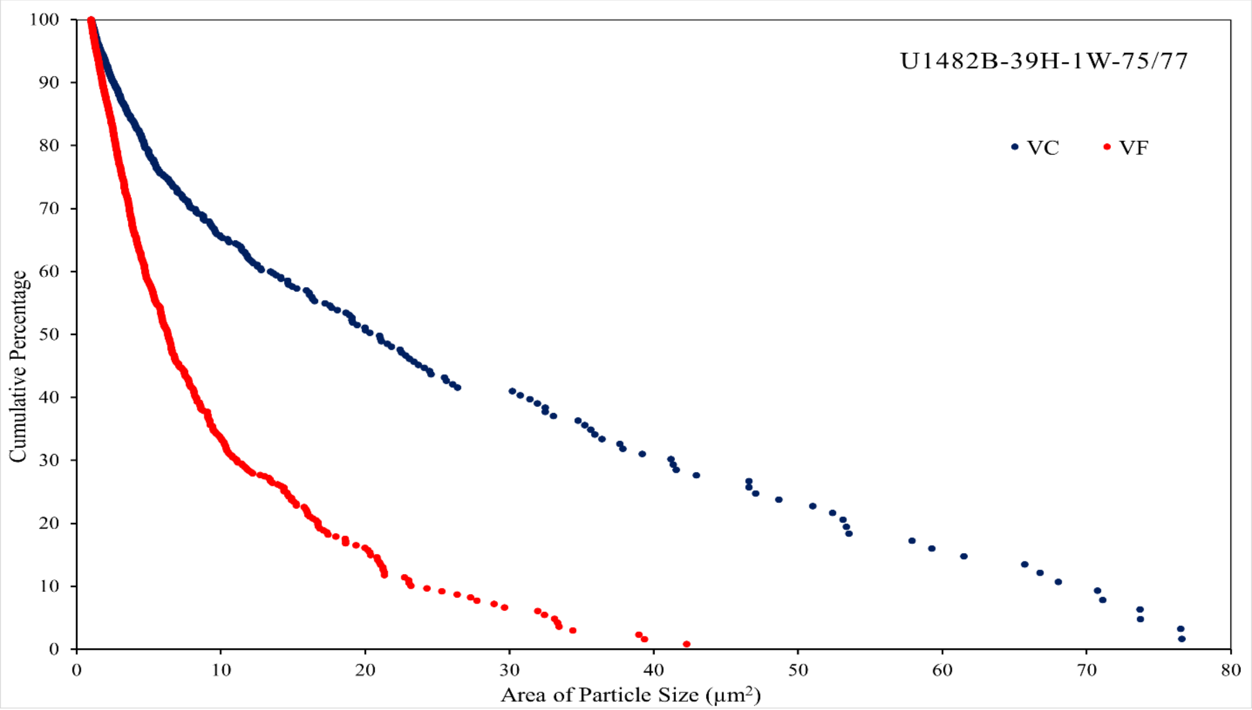

U1482B-39H-1W-75/77
● VC
● VF
Cumulative Percentage
100
90
80
70
60
50
40
30
20
10
0
0
10
20
30
40
50
60
70
80
Area of Particle Size (µm²)

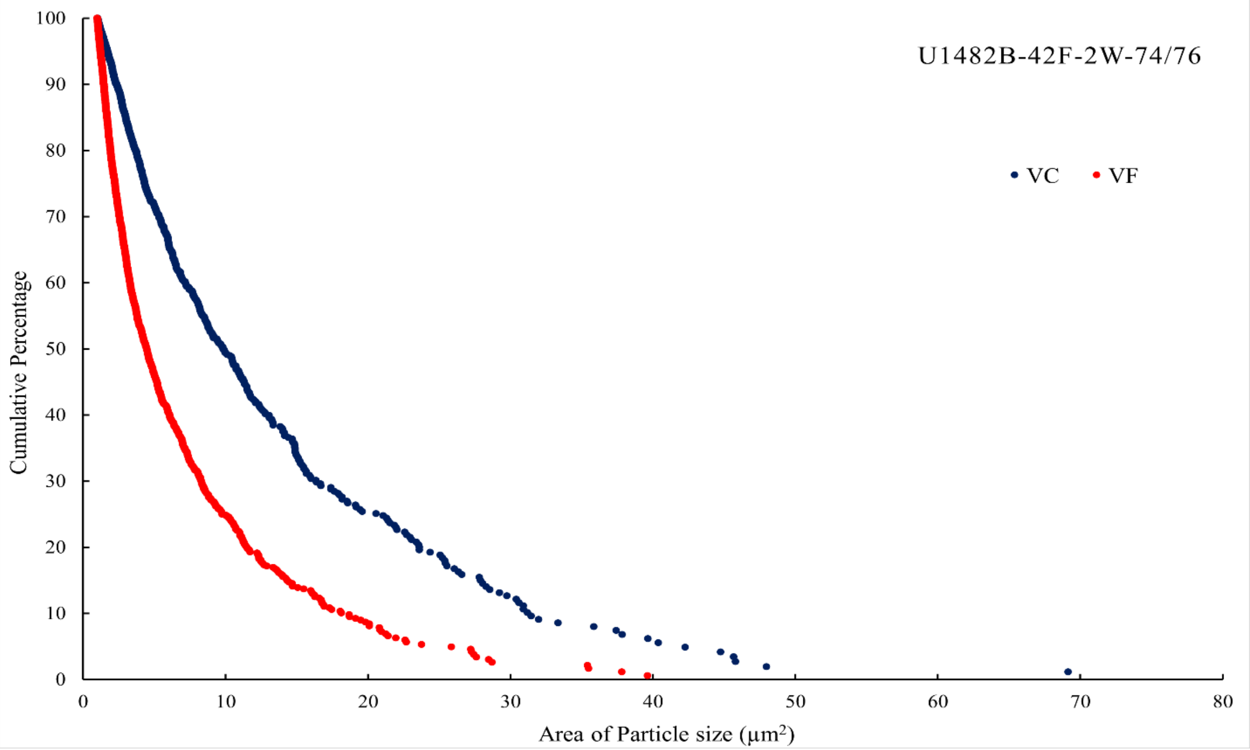
U1482B-42F-2W-74/76
● VC
● VF
Cumulative Percentage
Area of Particle size (μm²)
0
10
20
30
40
50
60
70
80
90
100
0
10
20
30
40
50
60
70
80

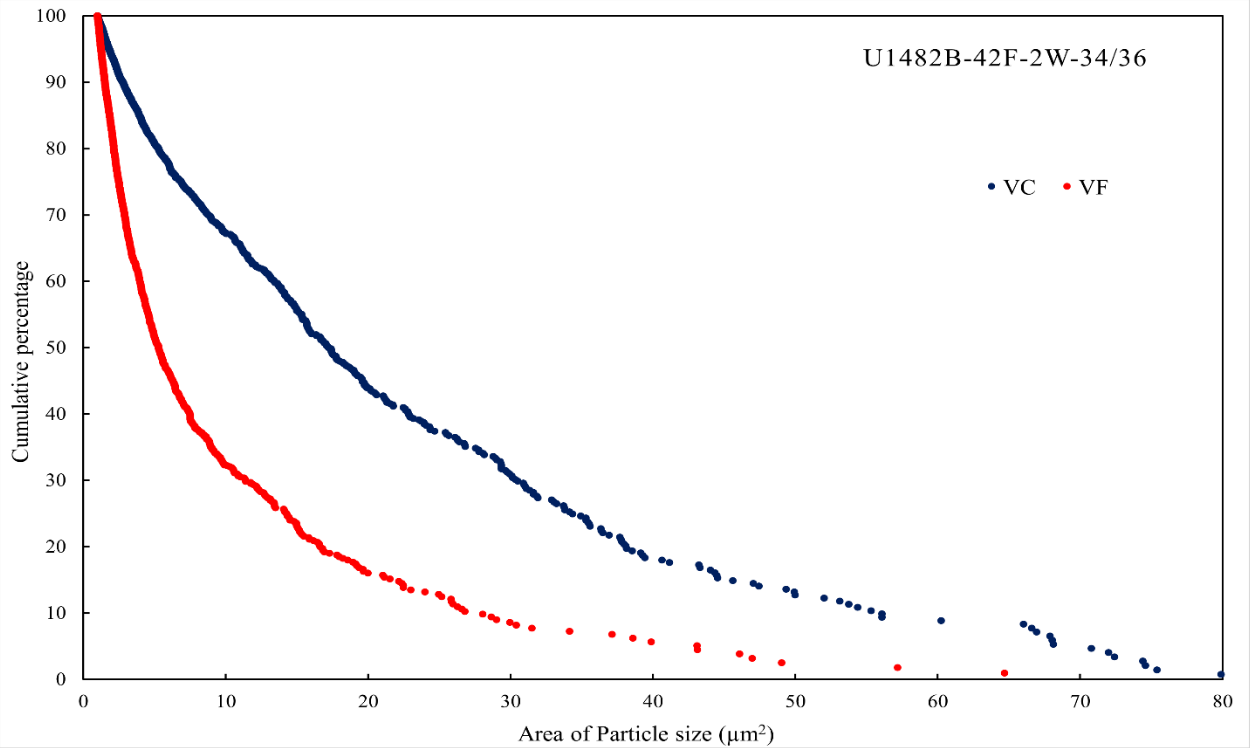
U1482B-42F-2W-34/36
● VC
● VF
Cumulative percentage
Area of Particle size (μm²)
0
10
20
30
40
50
60
70
80
90
100
0
10
20
30
40
50
60
70
80

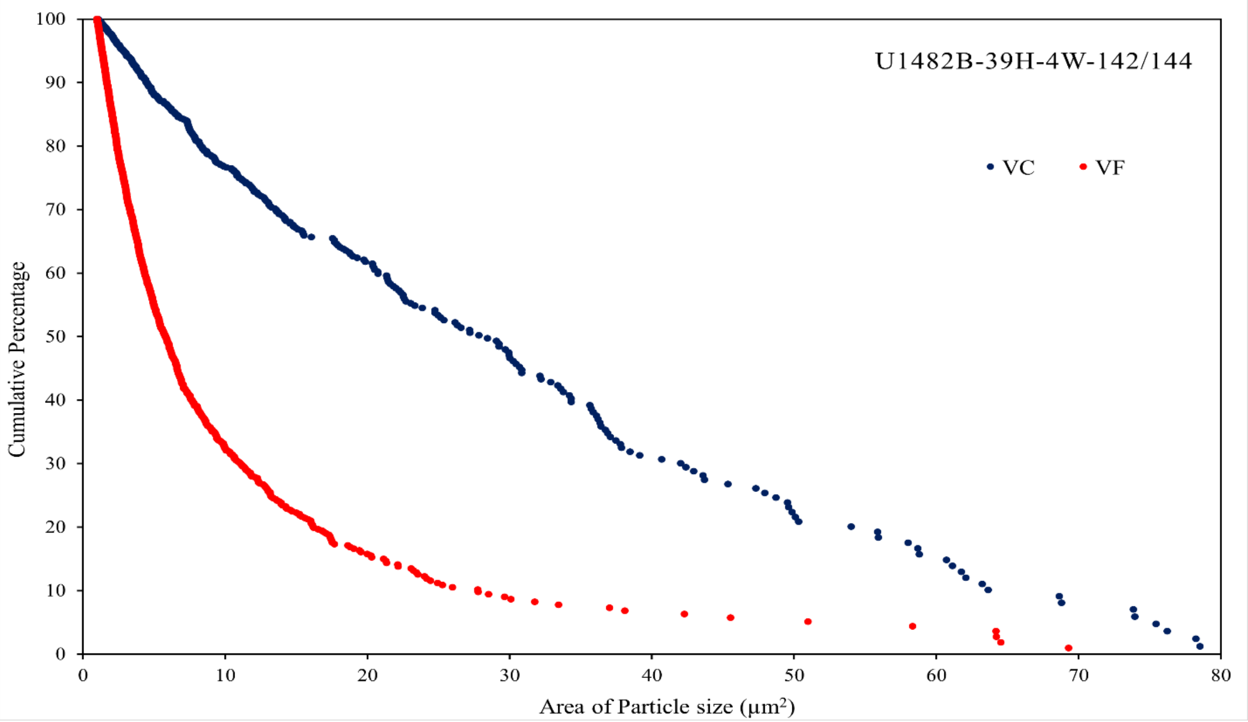
U1482B-39H-4W-142/144
● VC ● VF
Cumulative Percentage
Area of Particle size (μm²)
0
10
20
30
40
50
60
70
80
90
100
0
10
20
30
40
50
60
70
80

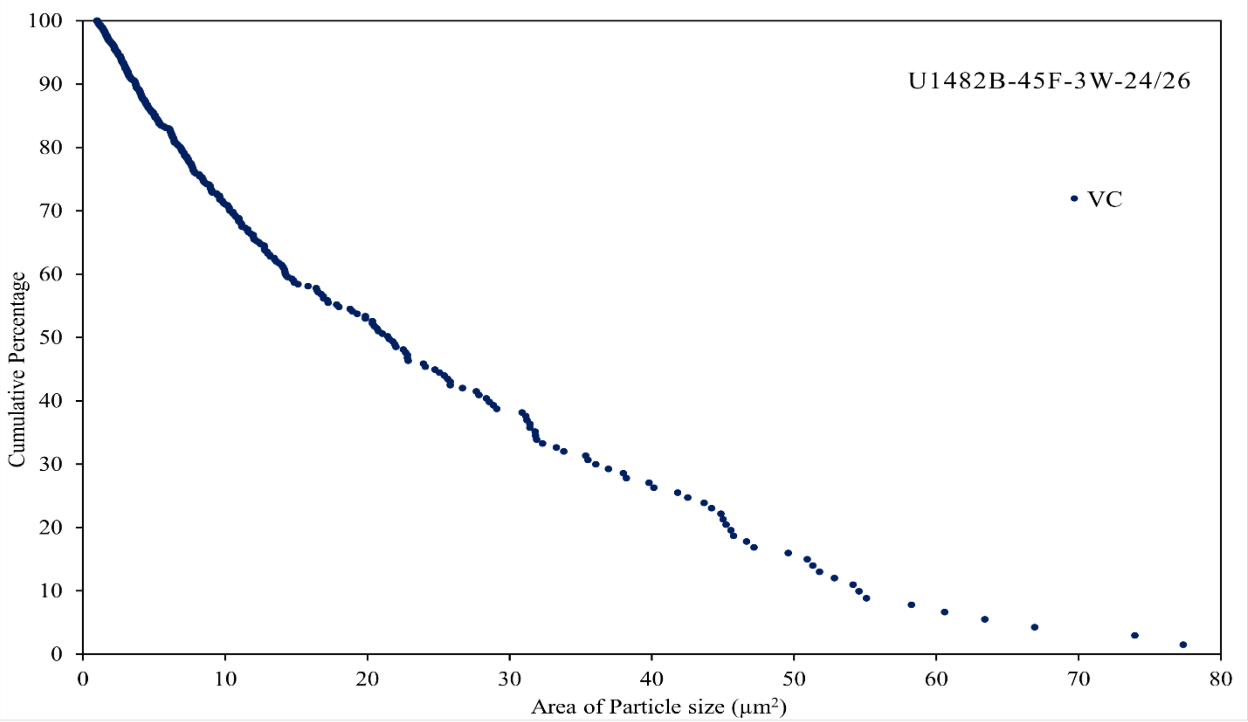
U1482B-45F-3W-24/26
● VC
Cumulative Percentage
Area of Particle size (μm²)
0
10
20
30
40
50
60
70
80
90
100
0
10
20
30
40
50
60
70
80

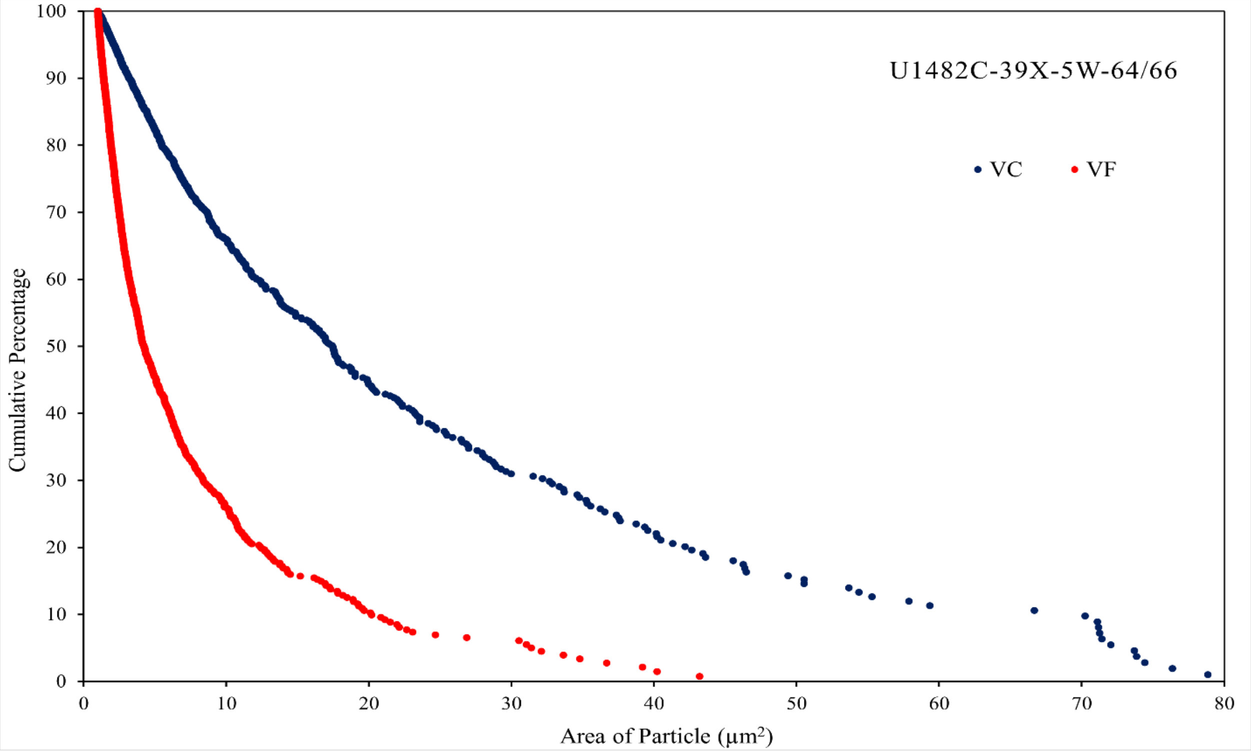
U1482C-39X-5W-64/66
VC
VF
Cumulative Percentage
100
90
80
70
60
50
40
30
20
10
0
0
10
20
30
40
50
60
70
80
Area of Particle (μm²)

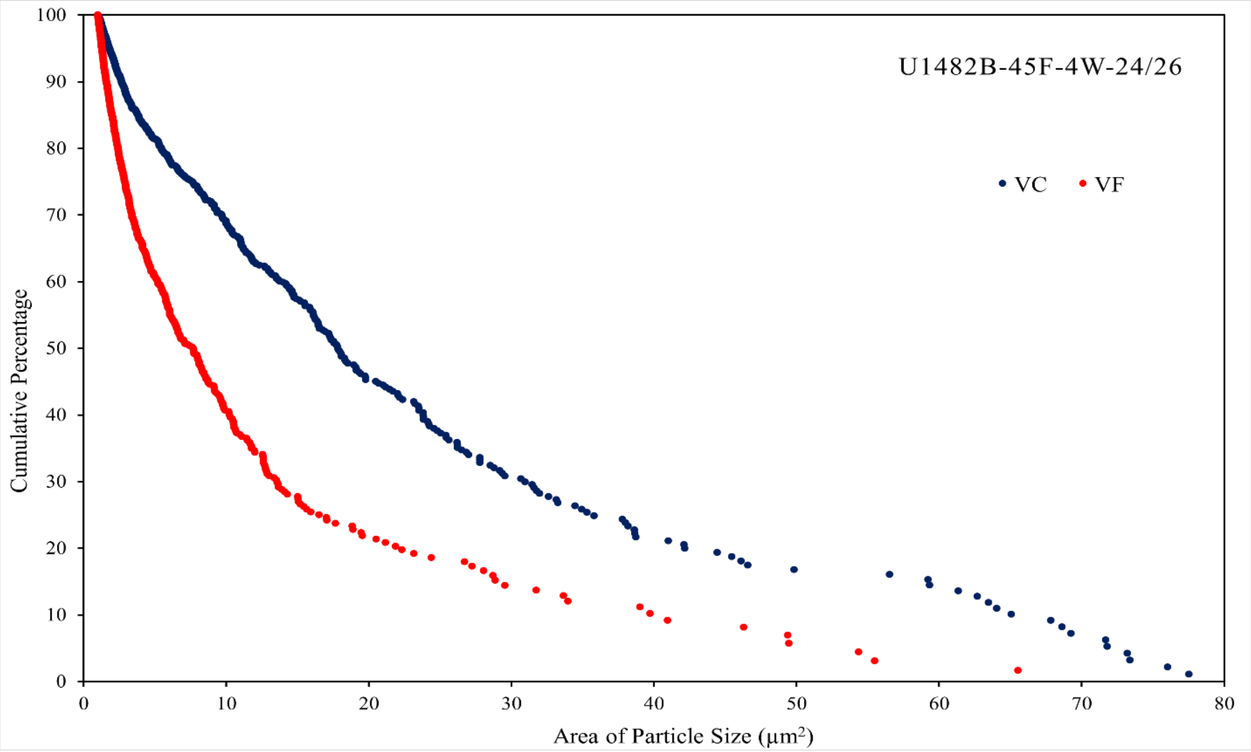
U1482B-45F-4W-24/26
VC
VF
Cumulative Percentage
100
90
80
70
60
50
40
30
20
10
0
0
10
20
30
40
50
60
70
80
Area of Particle Size (μm²)

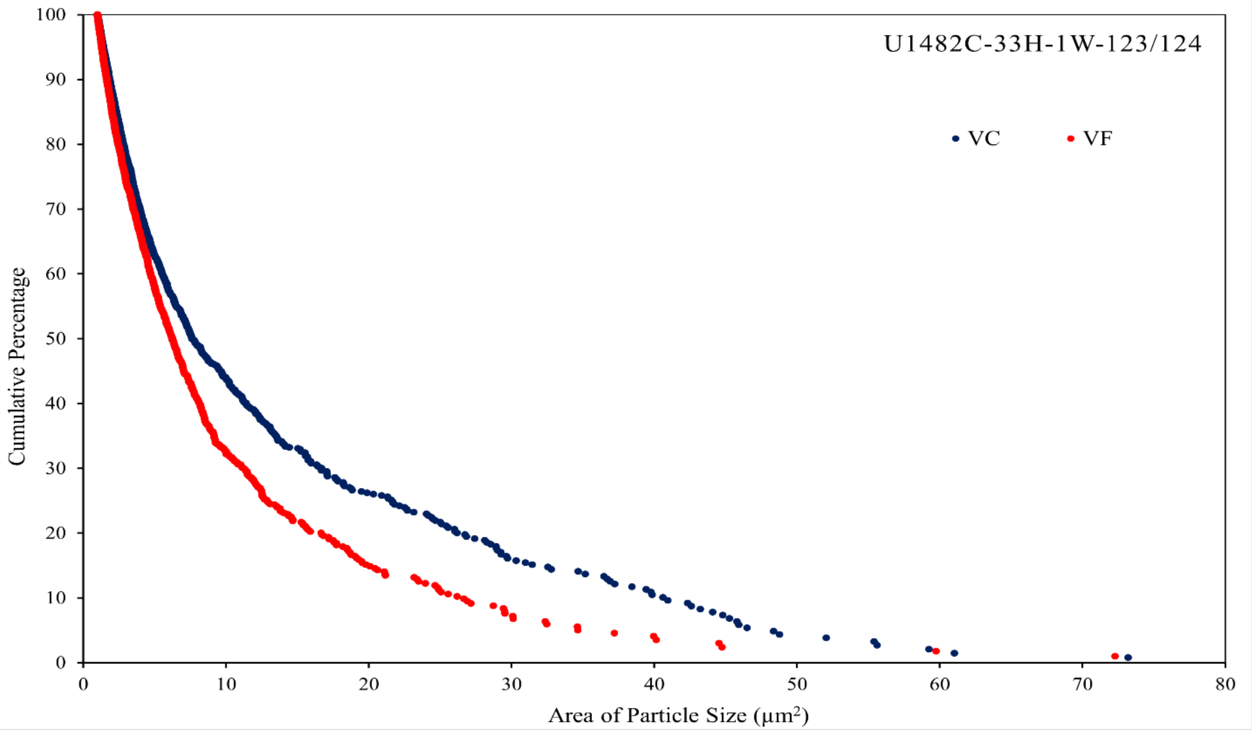
U1482C-33H-1W-123/124
VC
VF
Cumulative Percentage
Area of Particle Size (µm²)
0
10
20
30
40
50
60
70
80
90
100
0
10
20
30
40
50
60
70
80

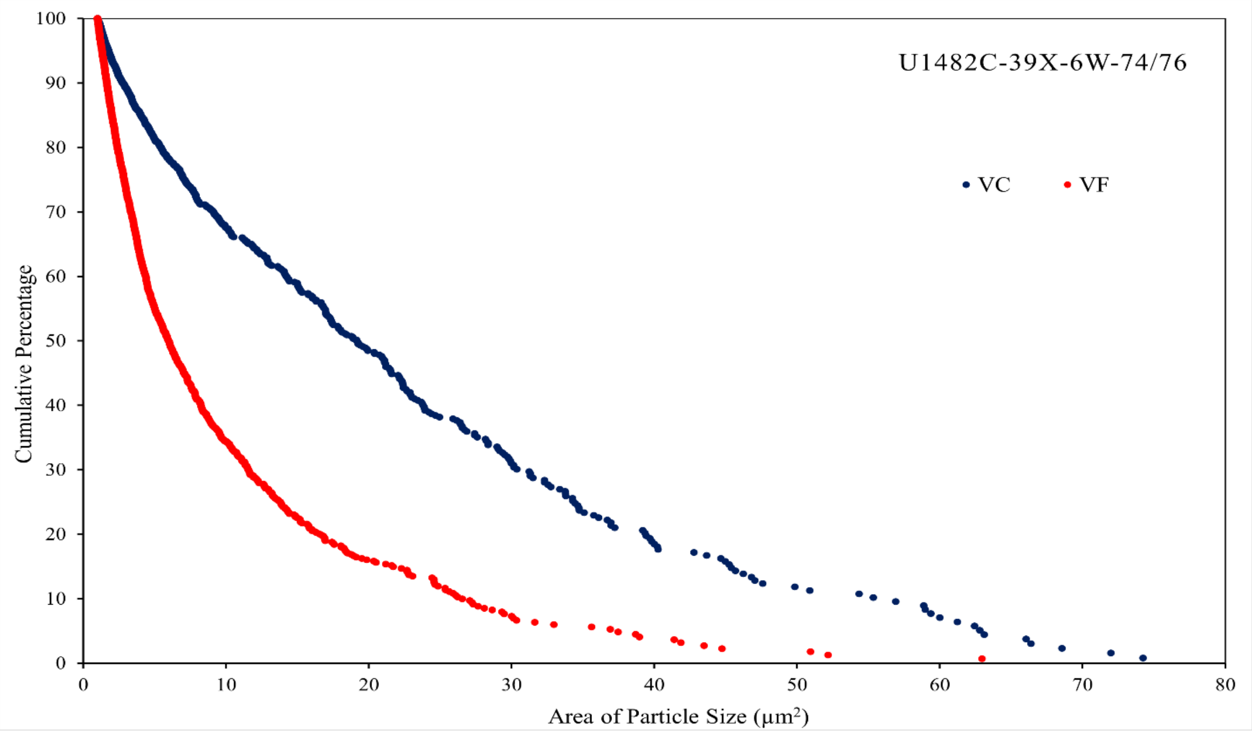
U1482C-39X-6W-74/76
VC
VF
Cumulative Percentage
Area of Particle Size (µm²)
0
10
20
30
40
50
60
70
80
90
100
0
10
20
30
40
50
60
70
80

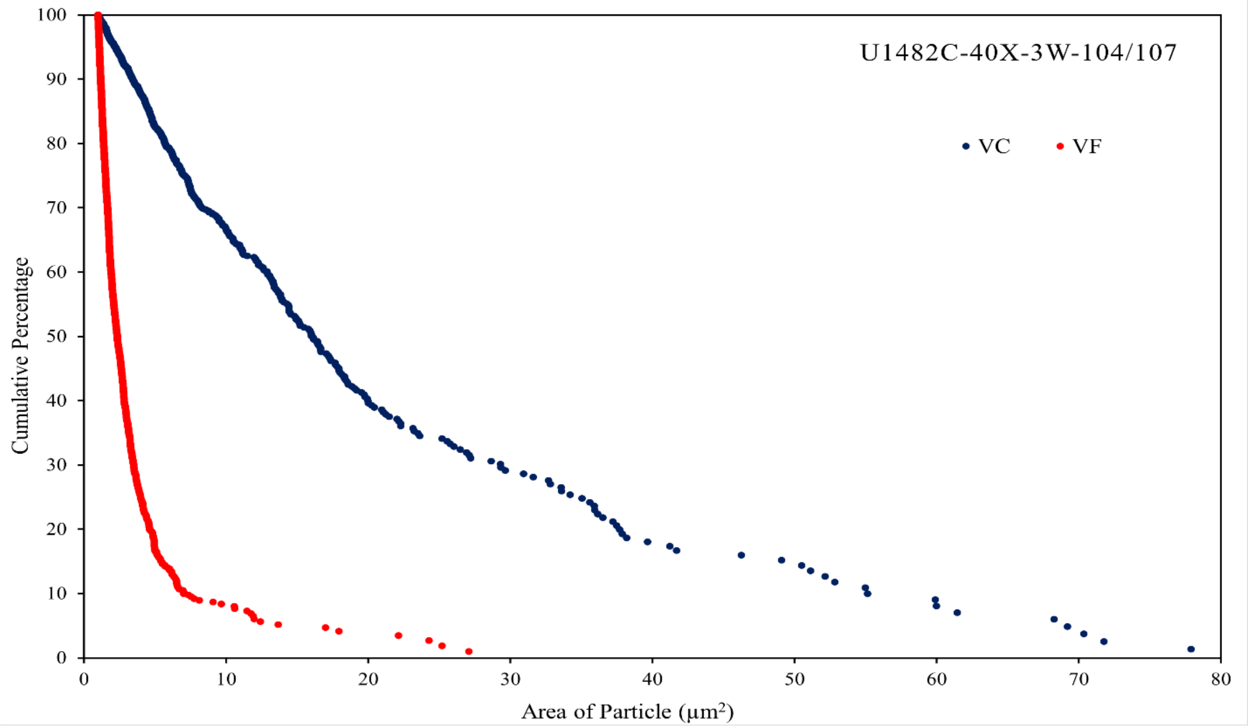
U1482C-40X-3W-104/107
VC
VF
Cumulative Percentage
Area of Particle (μm²)
0
10
20
30
40
50
60
70
80
90
100
0
10
20
30
40
50
60
70
80

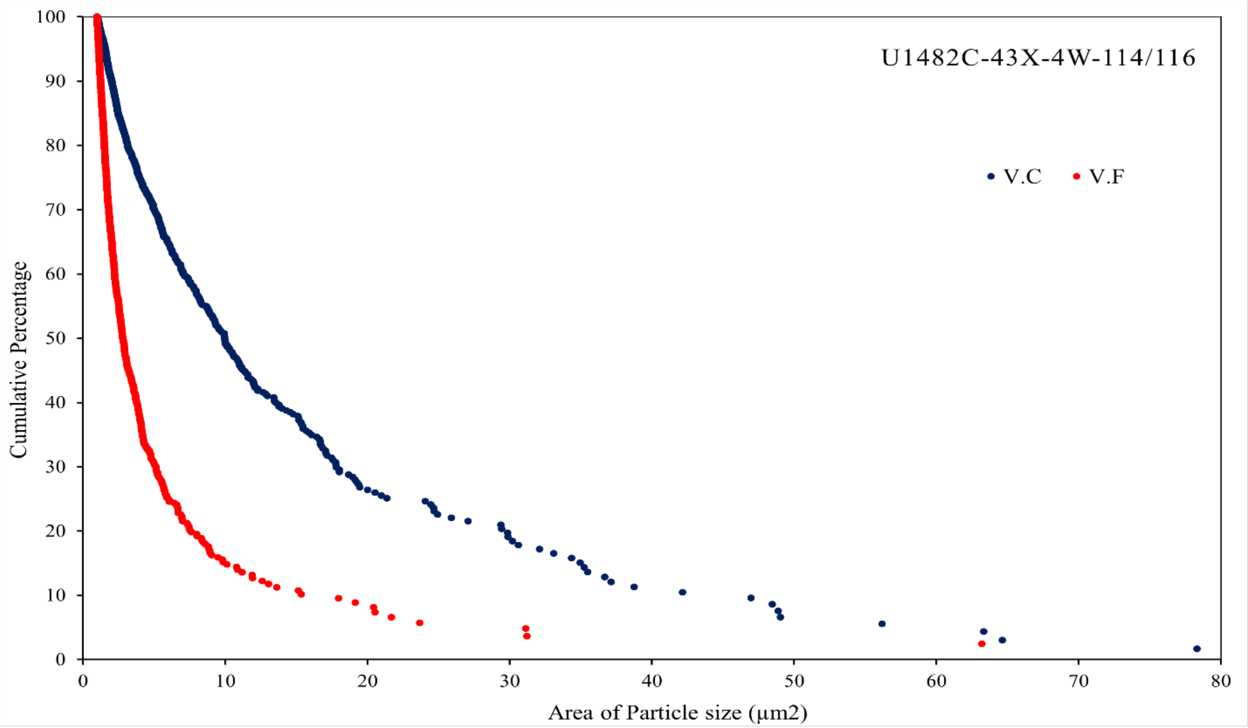
U1482C-43X-4W-114/116
V.C
V.F
Cumulative Percentage
Area of Particle size (μm2)
0
10
20
30
40
50
60
70
80
90
100
0
10
20
30
40
50
60
70
80

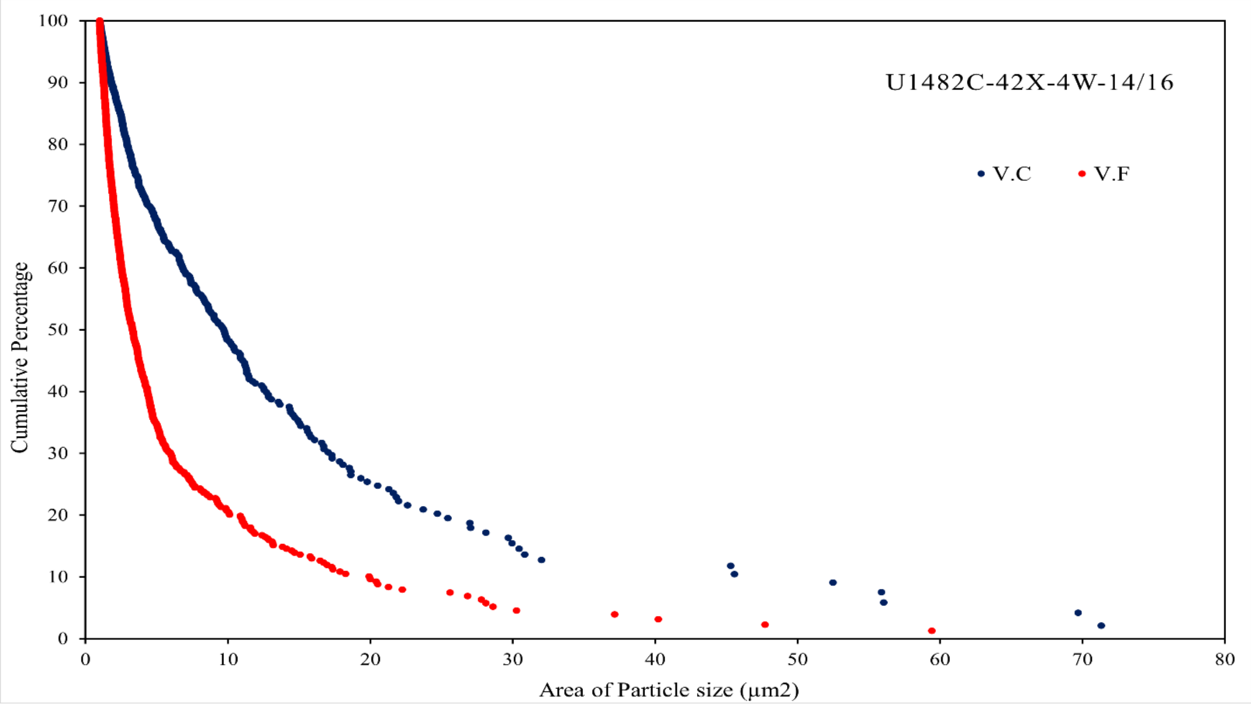
U1482C-42X-4W-14/16
V.C
V.F
Cumulative Percentage
100
90
80
70
60
50
40
30
20
10
0
0
10
20
30
40
50
60
70
80
Area of Particle size (µm2)

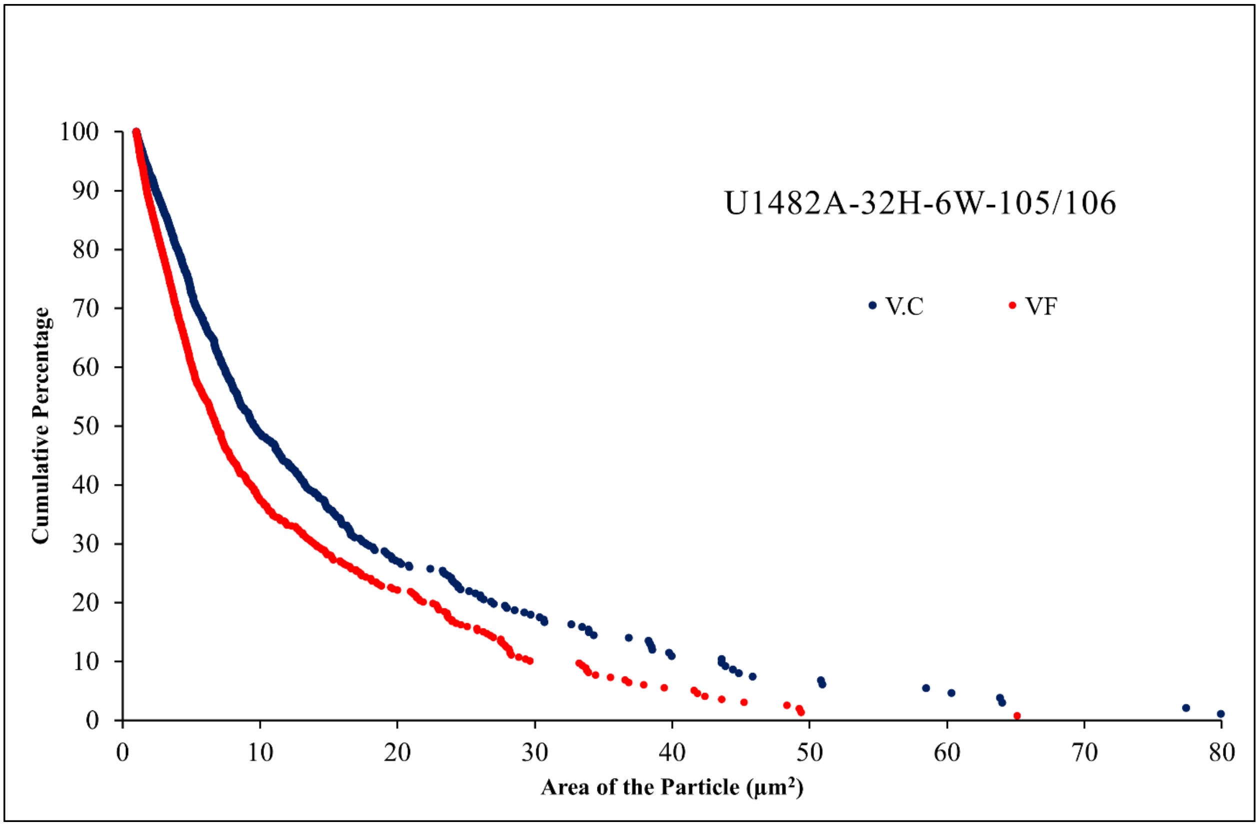
U1482A-32H-6W-105/106
V.C
VF
Cumulative Percentage
100
90
80
70
60
50
40
30
20
10
0
0
10
20
30
40
50
60
70
80
Area of the Particle (µm²)

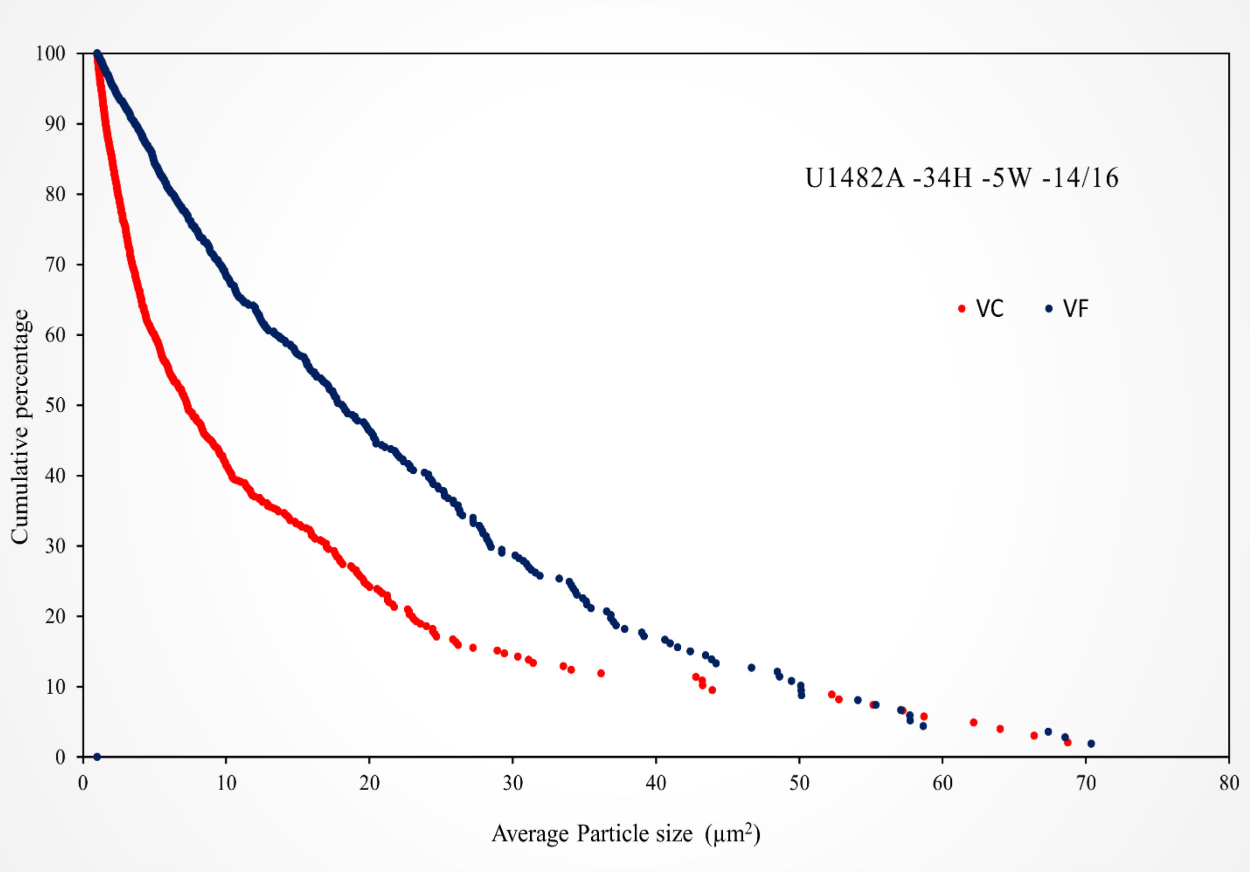
U1482A -34H -5W -14/16
● VC
● VF
Cumulative percentage
100
90
80
70
60
50
40
30
20
10
0
0
10
20
30
40
50
60
70
80
Average Particle size (μm²)

Appendix B: Bad Plots

All the charts below are Cumulative percentage versus particle size (µm²) distributions for different sediment samples. Blue circles represent the coarse fraction (V.C), and red circles represent the fine fraction (V.F). The x-axis shows area of particle size in (µm²), and the y-axis represents cumulative percentage, highlighting the variation in particle size distribution across different samples. These plots were considered bad because of the inaccurate separation between V.C and V.F particles either partially or fully in some cases.

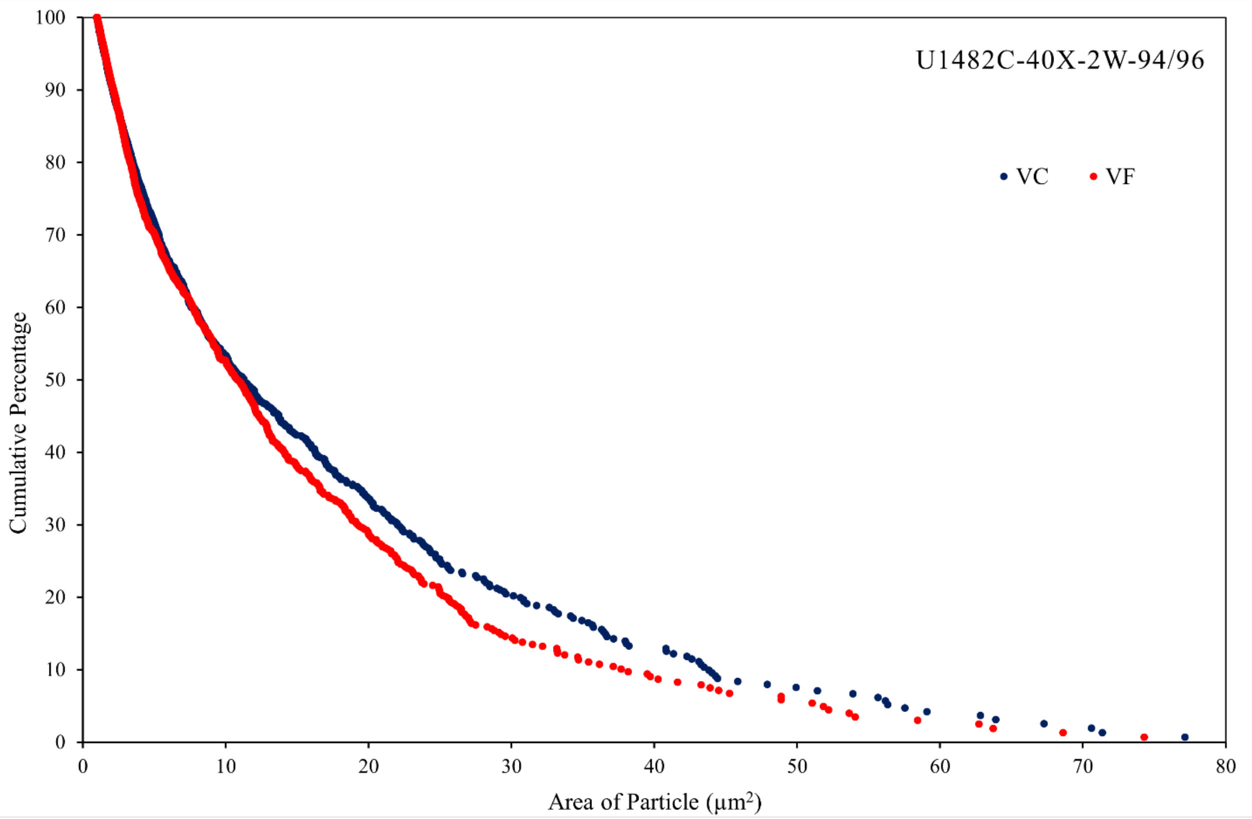

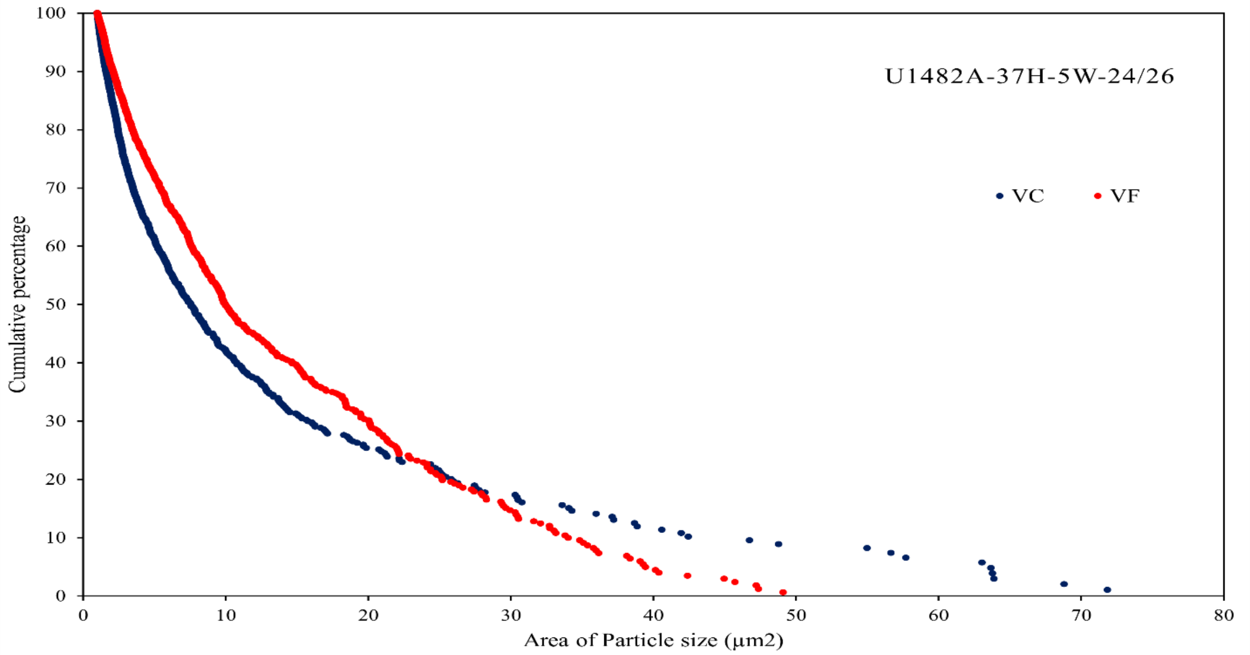
U1482A-37H-5W-24/26
VC
VF
Cumulative percentage
Area of Particle size (μm2)
0
10
20
30
40
50
60
70
80
90
100
0
10
20
30
40
50
60
70
80

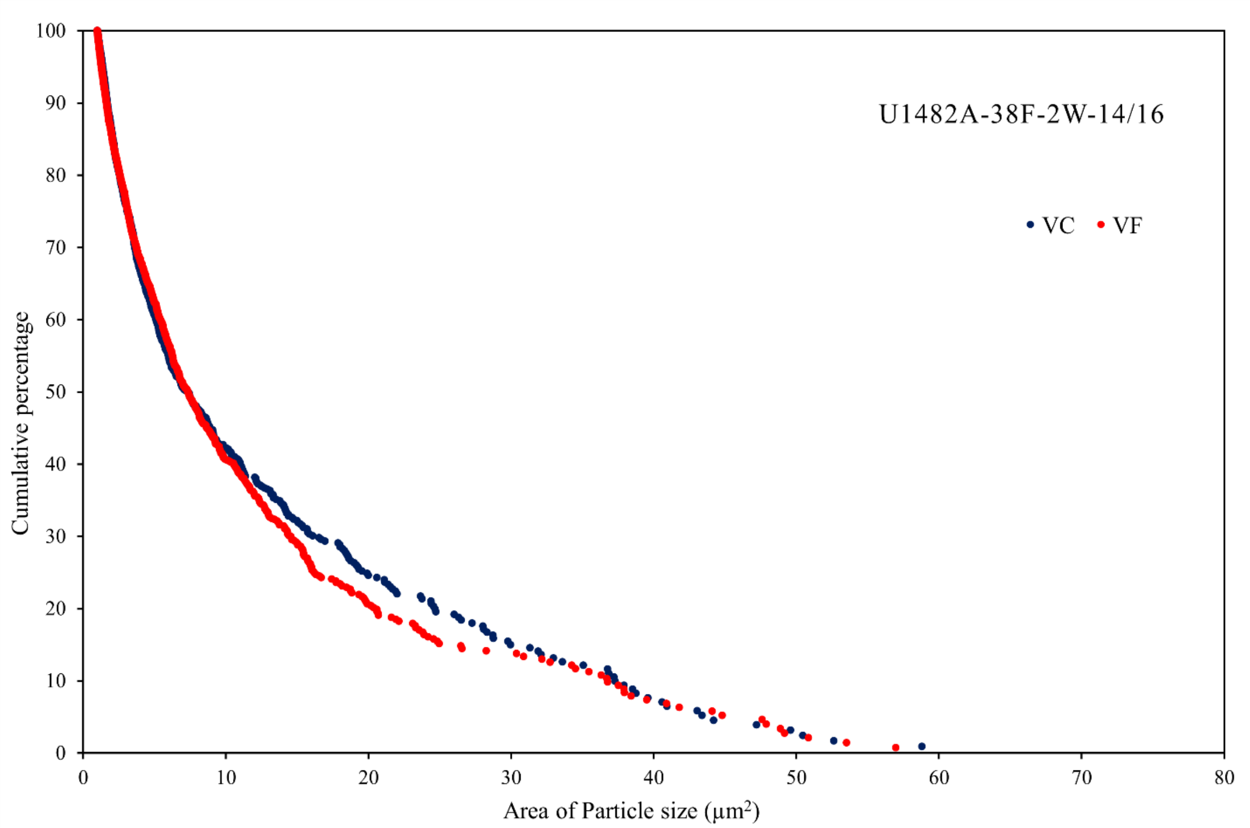
U1482A-38F-2W-14/16
VC
VF
Cumulative percentage
Area of Particle size (μm²)
0
10
20
30
40
50
60
70
80
90
100
0
10
20
30
40
50
60
70
80

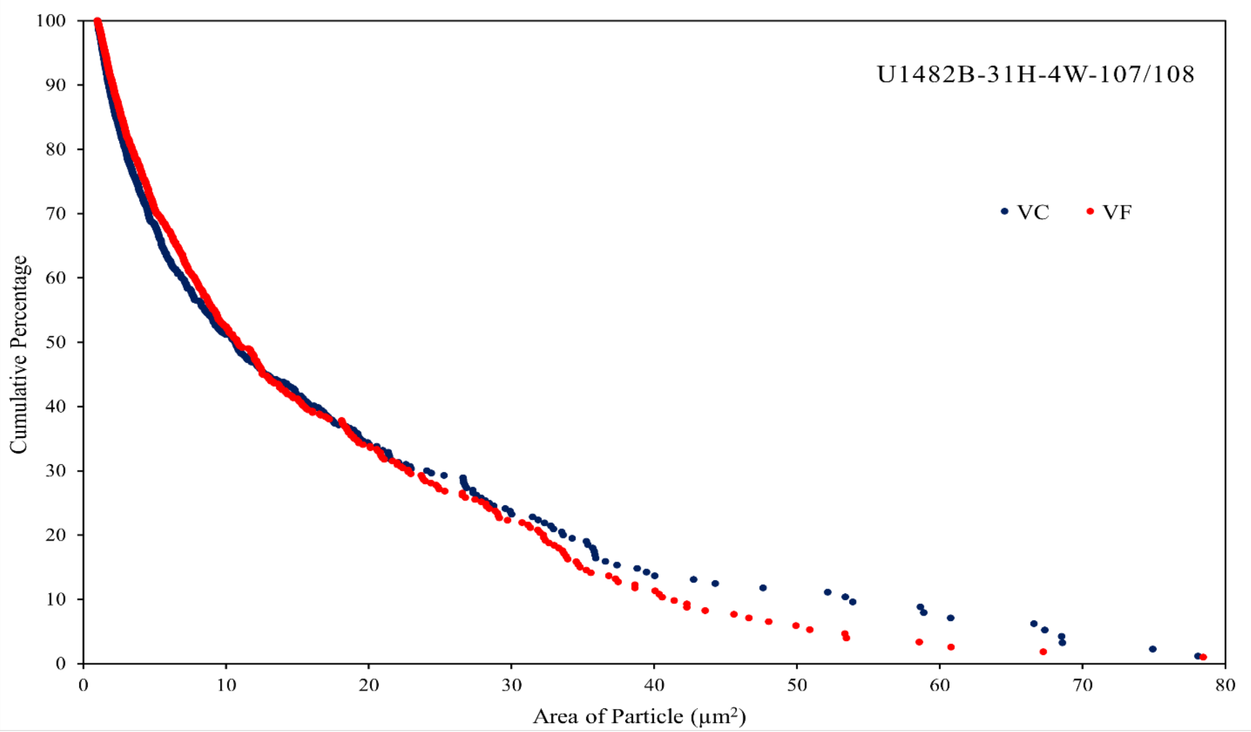
U1482B-31H-4W-107/108
VC
VF
Cumulative Percentage
Area of Particle (μm²)
0
10
20
30
40
50
60
70
80
90
100
0
10
20
30
40
50
60
70
80

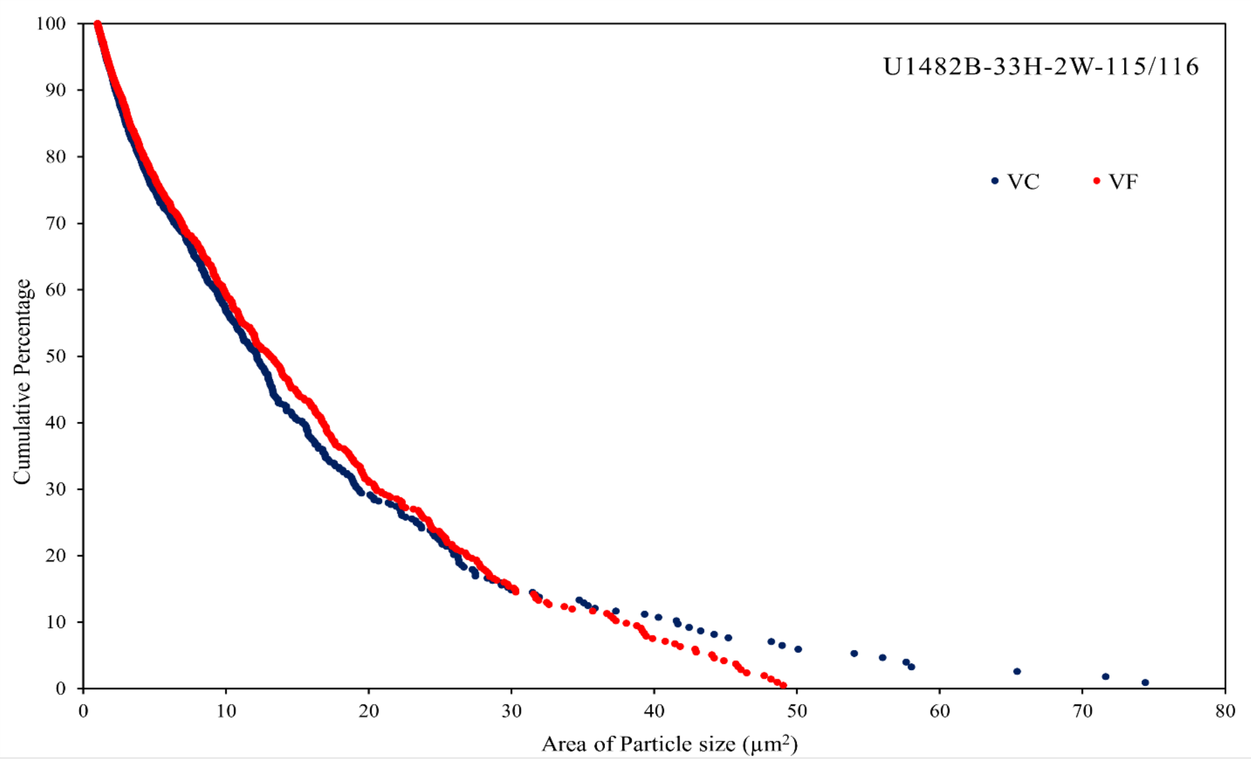
U1482B-33H-2W-115/116
VC
VF
Cumulative Percentage
Area of Particle size (μm²)
0
10
20
30
40
50
60
70
80
90
100
0
10
20
30
40
50
60
70
80

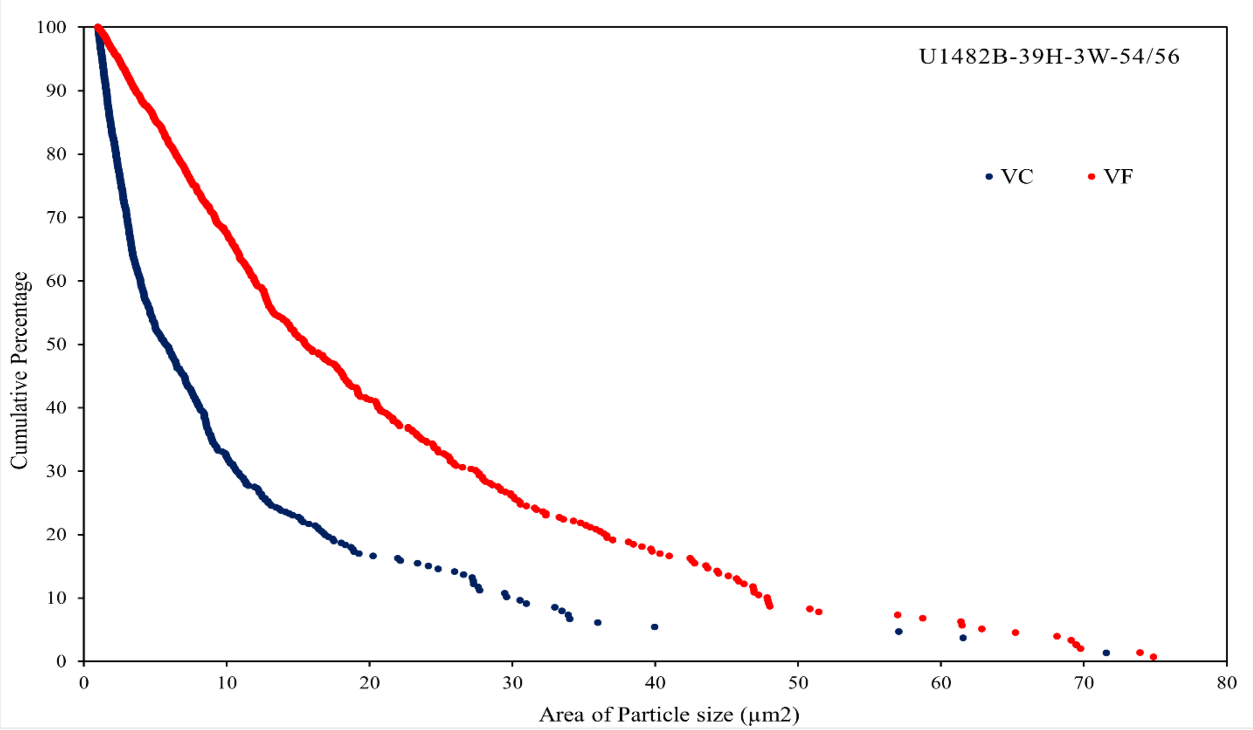
U1482B-39H-3W-54/56
● VC
● VF
Cumulative Percentage
0
10
20
30
40
50
60
70
80
90
100
0
10
20
30
40
50
60
70
80
Area of Particle size (µm2)

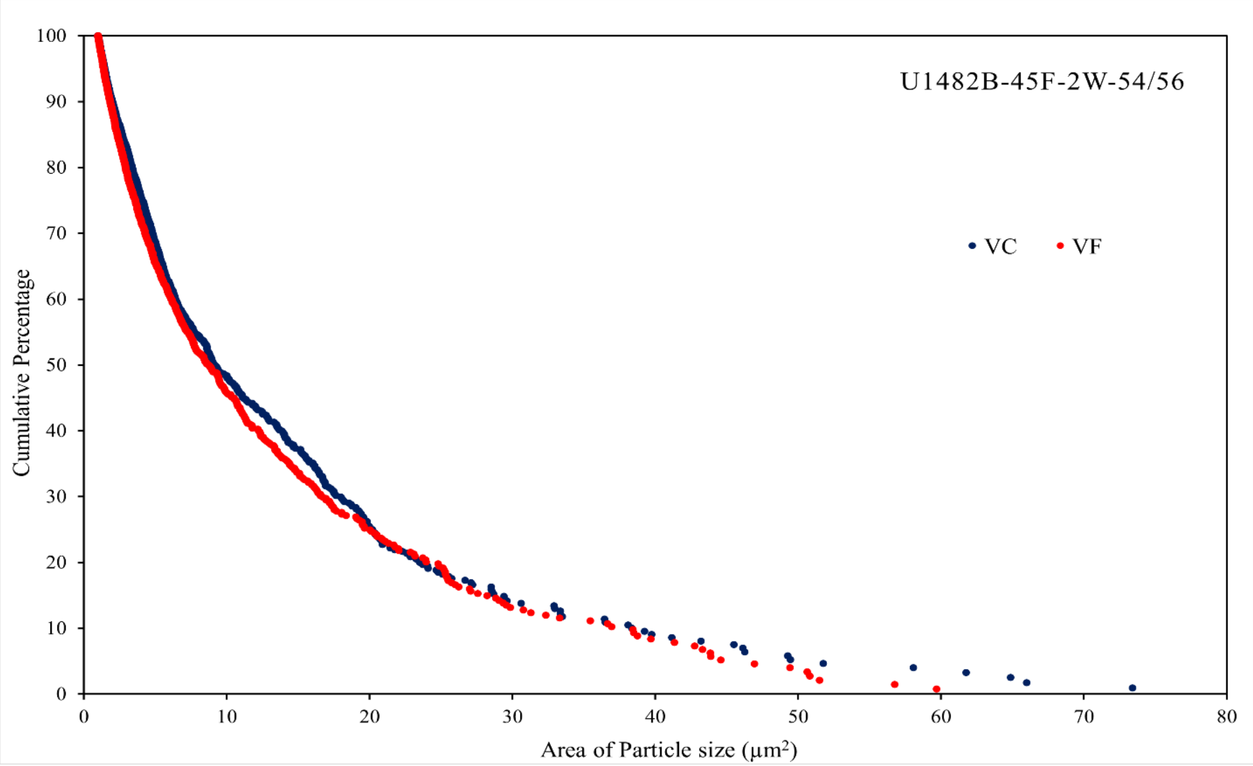
U1482B-45F-2W-54/56
● VC
● VF
Cumulative Percentage
0
10
20
30
40
50
60
70
80
90
100
0
10
20
30
40
50
60
70
80
Area of Particle size (µm²)

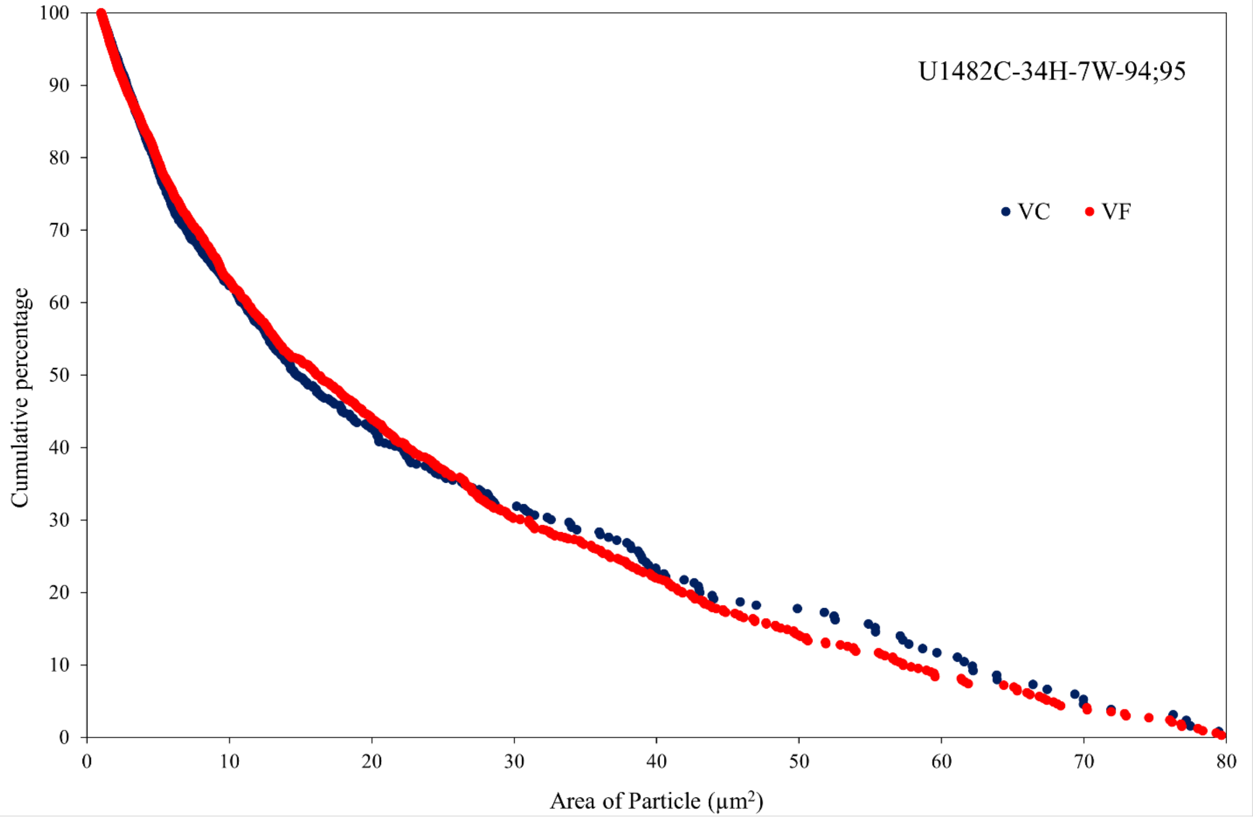
U1482C-34H-7W-94;95
● VC
● VF
Cumulative percentage
Area of Particle (μm²)
0
10
20
30
40
50
60
70
80
90
100
0
10
20
30
40
50
60
70
80

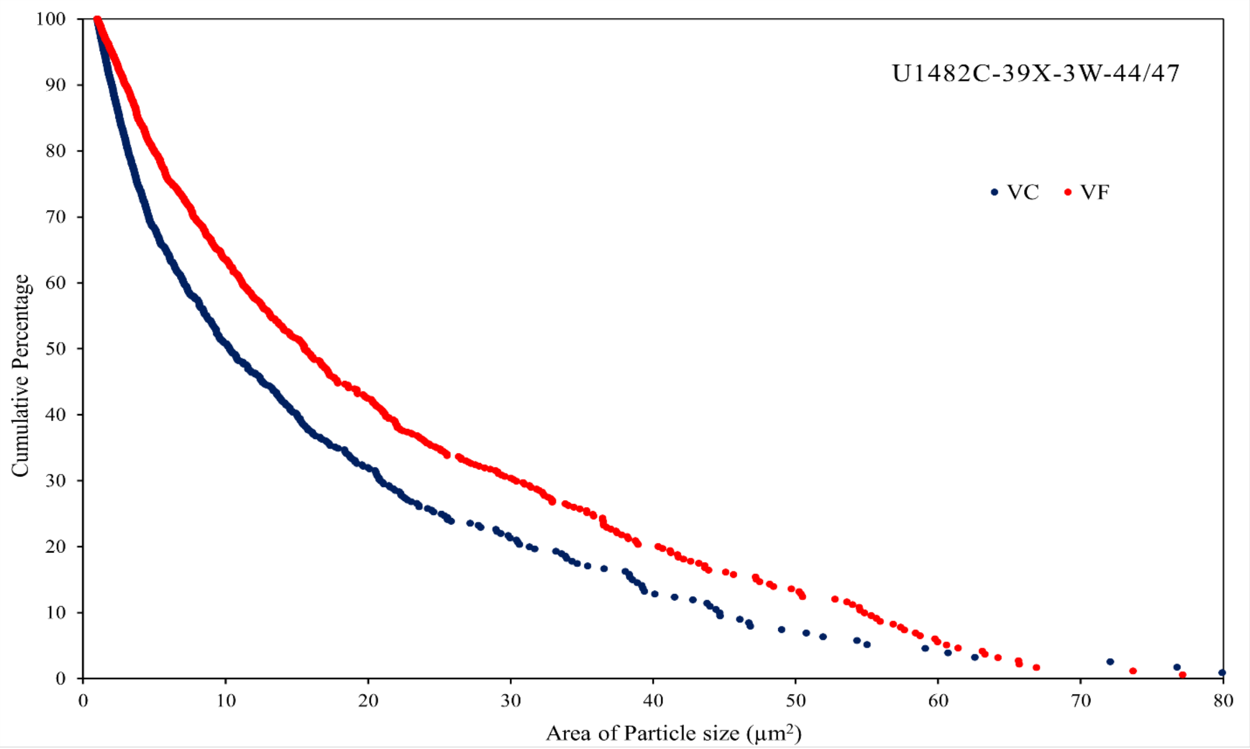
U1482C-39X-3W-44/47
● VC ● VF
Cumulative Percentage
100
90
80
70
60
50
40
30
20
10
0
0
10
20
30
40
50
60
70
80
Area of Particle size (μm²)

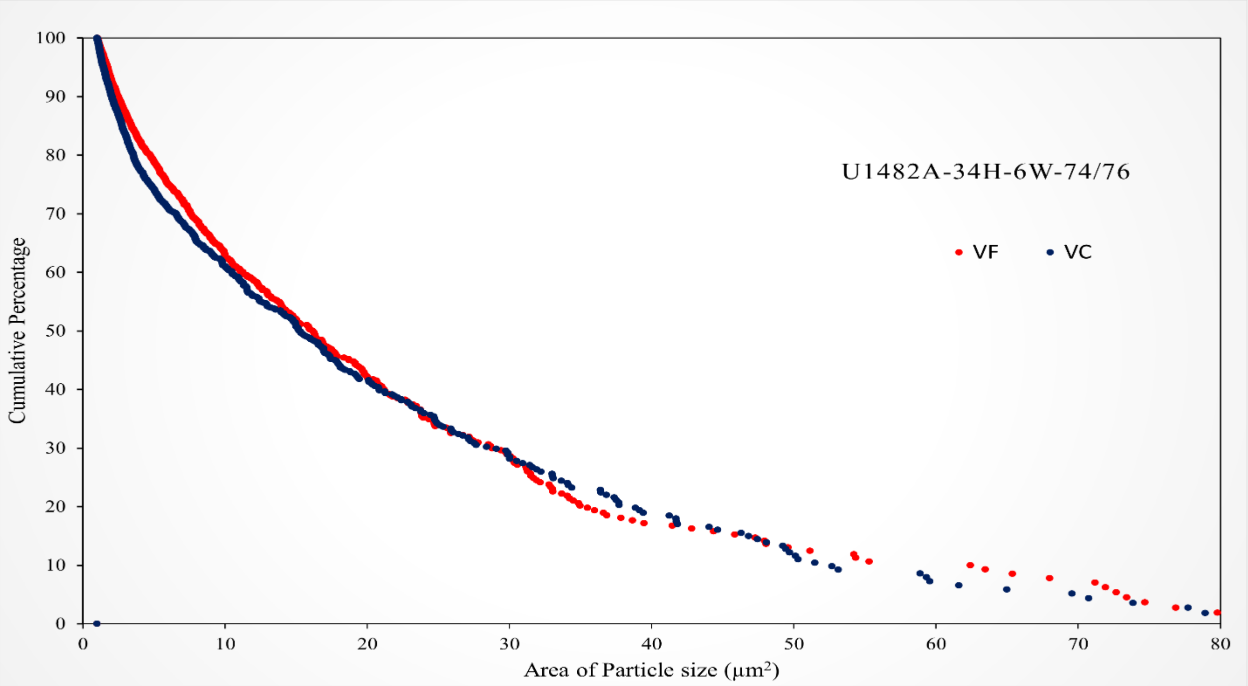
U1482A-34H-6W-74/76
● VF ● VC
Cumulative Percentage
100
90
80
70
60
50
40
30
20
10
0
0
10
20
30
40
50
60
70
80
Area of Particle size (μm²)